High Pressure High Temperature Reservoir Fluids with Focus on Scaling and Thermodynamic Modeling

Figueroa Murcia, Diana Carolina

Publication date:
2018

Document Version
Peer reviewed version

High Pressure High Temperature Reservoir Fluids with Focus on Scaling and Thermodynamic Modeling

Ph.D. Thesis
by
Diana Carolina Figueroa Murcia
2018

Center for Energy Resources Engineering
Department of Chemical and Biochemical Engineering
Technical University of Denmark
Kongens Lyngby, Denmark

DTU Chemical Engineering
Department of Chemical and Biochemical Engineering

Acknowledgements

This thesis is submitted as partial fulfilment of the requirement for the Ph.D. degree at Technical University of Denmark (DTU). The work has been carried out at Center for Energy Resources Engineering (CERE), Department of Chemical and Biochemical Engineering from December 2013 to May 2018. This work has been under the supervision of Associate Professor Kaj Thomsen and Associate Professor Philip Loldrup Fosbøl. This project was part of the Next Oil Project (New Extreme Oil and Gas in Denmark) funded by Mærsk Oil, DONG Energy and Innovation Fund Denmark.

I am deeply grateful to my supervisors for their mentorship, guidance and support through the development of this project. I appreciate every single discussion session we had to make this project a reality. Your encouragement empowered me to continue during this journey.

I am greatly indebted to the technicians at CERE, Zacarias, Povl and Dang. Thanks for your help during the design, construction and experimental stage of the solubility laboratory set-ups. The solubility measurements would not have been possible without their expertise. I would particularly like to thank Zacarias for his support, for the hours that we worked in the lab, for our discussion about politics and how to make this world a better one. Zacarias I will always cherish those moments in the lab.

I would like to express my gratitude to Teresa Regueira Muñiz for her valuable help, for her insightful comments and suggestions for the laboratory experiments.

I owe a very important debt to Sinh Hy Nguyen at the DTU Environment. His expertise with the ICP-OES made possible the obtention of the solubility results. I appreciate the time he invested in analyzing the samples, his willingness to help and his commitment to deliver results on time. Thanks are also due to Søren Vestergaard Madsen, with his commitment, expertise and professionalism the HT Titanium Cell became a reality.

Some special words of gratitude go to my friends who have always supported me and kept my spirit up: Luisa, Carolina, Natalia, Angelica, Lili Me, Lili Di and Lili Ma. *Gracias chicas!*

Mi inmensa gratitud es para mis padres y hermano, quienes siempre con su amor y palabras de aliento me han apoyado en todos los proyectos de mi vida. Y aunque perseguir mis sueños nos ha mantenido alejados físicamente su presencia siempre está conmigo. A mis tías Amparo y Consuelo por siempre tener un espacio en su corazón para mí.

Last but not least, infinite gratitude to my love and my everything, my beloved husband József, for his immense support and guidance. You always keep me going despite adverse times and encourage me to be a better person every day. *Én nagyon szeretlek!*

I am beyond grateful to my son David. He has enlightend my life during the last fourteen months of this project. He inspires me every day with his smiles and unconditional love. This thesis is dedicated to my son David.

Summary

Extensive research to increase the world's oil reserves is focused on the High-Pressure High-Temperature (HPHT) reservoirs. These reservoirs represent a great opportunity but also a challenge in terms of drilling, extraction operations and safety protocols. The extreme operating conditions and harsh environments of the HPHT reservoirs push the limits of engineering. Developing new materials that can withstand elevated temperatures, highly corrosive atmosphere (e.g. the presence of H_2S) and building machinery capable of working at pressures above 690 bars are at the order of the day. Among the cumbersome conditions mentioned, consequences inherent to the exploration activities, such as the rapid pressure drop will cause for example the deposition of minerals. The deposition of materials is referred to as scaling. The occurrence of scaling in oil reservoirs bring adverse consequences such as clogged pipes, malfunction of safety equipment (*e.g.* the safety valve) and reduction of the production of the well. Nowadays, the sulfide scaling materials are gaining more attention as they require a different treatment for their removal compared to the common scaling minerals found in oil reservoirs. These materials are formed as the product from the reaction between metallic ions (present either in the formation waters or injected brines) and H_2S present in the reservoir.

The aim of this thesis is to study the solubility of scaling materials, specifically Zinc Sulfide (ZnS), Iron Sulfide (FeS) and Lead Sulfide (PbS) at conditions that resemble HPHT reservoirs. Firstly, the Joule Thomson Effect (JTE) was evaluated to determine the impact of the decompression process on the final temperature of a confined fluid at HPHT conditions. Three different fluids (water, oil and brine) were included in this study. It was concluded that the increase of temperature for oil at non-isenthalpic conditions is 7.4 °C This represents a reduction of 16.8 °C compared to the final temperature estimated at isenthalpic conditions. Thus, these results show that if the JTE is estimated at isenthalpic conditions the final temperature is overestimated.

This study presents the design of an experimental apparatus at laboratory scale as well as the development of a reliable experimental methodology for measuring the solubility of minerals at HPHT conditions and especially at very low concentrations (trace elements).The designed experimental apparatus is a borosilicate glass set-up for measuring the solubility at temperatures up to 80 °C. Additionally, a High-Temperature Cell made of Titanium was built to perform the solubility experiment at temperatures up to 200 °C and 60 bars. Several drawbacks from published solubility methods were addressed in this study:(1) Anoxic conditions were guaranteed throughout the process, (2) sufficiently long contact time was assured between the solvent and the solute to assure steady state

conditions and (3) an adequate analytical technique for measuring trace elements: Inductively Coupled Plasma Optical Emission Spectrometry (ICP-OES) was chosen. Saturated solutions of the minerals were prepared and then the aqueous solution was analyzed using ICP-OES. Afterwards, the experimental data were used for adjusting the Extended UNIQUAC model to predict the solubility of sulfides by means of thermodynamic calculations.

The prediction of the occurrence of the scaling materials in an oil reservoir is a foremost tool for the operator of a well. The results showed that the Extended UNIQUAC model can represent the solid-liquid equilibrium of Zinc Sulfide and Iron Sulfide up to 100 °C. Difficulties were encountered for representing the solid-liquid equilibrium of the PbS aqueous system. The inclusion of complexes into the speciation equilibrium model is required to achieve good results. This study is a step towards understanding the behavior of sulfide scaling materials at high-temperatures and high-pressures.

Dansk Resumé

Omfattende forskning i at øge verdens oliereserver er fokuseret på højtryks-høj temperatur (HPHT) reservoirer. Disse reservoirer udgør en stor mulighed men samtidig også en udfordring for boringer, indvindingsoperationer og sikkerhedsprocedurer. De ekstreme arbejdsbetingelser og barske miljøer i et HPHT-reservoir skubber til grænserne for ingeniørkunst. På dagsordenen er derfor at udvikle nye materialer der kan tåle høje temperaturer og en stærkt korroderende atmosfære (fx. tilstedeværelse af H_2S) og nyt udstyr der kan arbejde ved tryk over 690 bar. På grund af de svære betingelser vil der være konsekvenser for olieudvindingsaktiviteter, blandt andet udfældning af mineraler grundet det hurtige trykfald. Denne udfældning af mineralsk materiale kaldes "scaling". Tilstedeværelsen af "Scaling" i oliereservoirer har alvorlige konsekvenser såsom stoppede rør, svigtende sikkerhedsudstyr (fx. sikkerhedsventiler) og en reduktion af produktionen i brønden. På nuværende tidspunkt får sulfidholdige scaling materialer mere opmærksomhed da de kræver en anden behandling for at blive fjernet end de almindeligt forekommende scaling mineraler i oliereservoirer. Disse materialer dannes ved reaktionen mellem metalioner [tilstede i formationsvandet eller injiceret (brines)] og H_2S som er tilstede i reservoiret.

Formålet med denne afhandling er at studere opløseligheden af "scaling" materialer, især Zinksulfid (ZnS), Jernsulfid (FeS) og Blysulfid (PbS) ved HPHT reservoir-lignende betingelser. Som det første blev Joule Thomson effekten (JTE) undersøgt for at bestemme indflydelsen af dekomprimeringsprocessen på den endelige temperatur af en indesluttet væske ved HPHT betingelser. Tre forskellige væsker (vand, olie og saltopløsninger) blev inkluderet i dette studie. De blev konkluderet at temperaturøgningen for olie ved ikke-isenthalpiske forhold er 7.4 °C. Dette svarer til en sænkning på 16.8 °C sammenlignet med den endelige temperatur anslået ved isenthalpiske forhold. Disse resultater viser altså at hvis JTE anslås ved isenthalpiske forhold bliver den endelige temperatur overvurderet.

Dette studie præsenterer frembringelsen af et eksperimentelt udstyr i laboratorieskala og udviklingen af en driftsikker metodologi til at måle opløseligheden af mineraler ved HPHT-betingelser og især ved meget lave koncentrationer (sporelementer). Det frembragte eksperimentaludstyr består af et borosilikat-glas set-up til at måle opløselighed ved temperaturer op til 80 °C. Yderligere blev en Højtemperatur-celle lavet i titanium for at udføre opløselighedseksperimenter op til 200 °C og 60 bar. Adskillige ulemper ved publicerede opløselighedsmetoder blev adresseret i dette studie: (1) Iltfrie betingelser blev sikret under hele processen, (2) tilstrækkelig lang kontakttid mellem

opløsningsmiddel og opløst stof blev sikret for at opnå *steady-state* betingelser og (3) en passende analytisk metode til at bestemme sporstoffer: Inductively Coupled Plasma Optical Emission Spectrometry (ICP-OES) blev anvendt.

Mættede opløsninger af mineralerne blev forberedt og den vandige opløsning analyseret med ICP-OES. Efterfølgende blev de eksperimentelle data brugt til at justere den udvidede (Extended) UNIQUAC model for at forudsige opløseligheden af sulfider ved hjælp af termodynamiske beregninger.

Forudsigelse af dannelse af "scaling" materialer i et oliereservoir er et af de vigtigste redskaber for operatøren af brønden. Resultaterne viste at Extended UNIQUAC modellen kan repræsentere fast stof-væske ligevægten af Zinksulfid og Jernsulfid op til 100 °C. Der opstod problemer med at repræsentere fast stof-væske ligevægten for det vandige PbS system. Inkluderingen af komplekser i "speciation model" kræves for at opnå gode resultater. Dette studie er et skridt hen imod at forstå opførslen af sulfid "scaling" materialer ved høje temperaturer og høje tryk.

List of Symbols

A	Debye-hückel parameter [$(kg \cdot mol^{-1})^{1/2}$]
B	molality [mol·kg of $water^{-1}$]
C	velocity [$m \cdot s^{-1}$]
C_P	heat capacity [$J\ K^{-1}\ mol^{-1}$]
E	total energy
G	gravitational acceleration [$m \cdot s^{-2}$]
G	Gibbs free energy
H	enthalpy
K_e	solubility product
M^{2+}	metallic ion (Zn^{2+}, Fe^{2+}, Pb^{2+})
N	number of moles
P	pressure
Q	heat
R	gas constant [$J\ K^{-1}\ mol^{-1}$]
S	entropy
S_{Total}	concentration of total sulfur
T	temperature
U	internal energy
U	interaction energy parameter
V	Volume
W_s	shaft work
X	mole fraction
Z	Elevation
Z	co-ordination number
R	UNIQUAC volume parameter
Q	UNIQUAC surface parameter
M	molar mass
I	ionic strength
μ	Joule Thomson coefficient
α	isobaric expansivity
θ	diffraction angle
γ	activity coefficient
μ_i	chemical potential
Δ	change of a quantity
ν	stoichiometric coefficient
Φ_i	volume fraction
θ_i	surface area fraction
ψ	parameter

Subscripts

f	formation
r	reaction

i	component
j	equilibrium phase
s	solid
aq	aqueous
w	water

Superscripts

Ex	Excess
0	standard state

Contents

INTRODUCTION

1.1 Introduction

The demand of fossil fuels has turned the attention to exploration of new reservoirs at extreme temperatures and pressures. The high pressures, temperatures and the depth of these reservoirs represent a challenge in terms of exploration, drilling and operating conditions. One of the challenges is to overcome sudden changes of temperature as a consequence of the change in pressure when the oil is pumped out to the surface. An unexpected increase of temperature (known as inverse Joule Thomson Effect) can lead to precipitation of salts present, causing scale formation.

The changes in pressure and temperature in HPHT alter the equilibria of the formation water in the reservoir making the chances of precipitation of scaling materials very high. Recently the deposition of materials such as Zinc Sulfide (ZnS), Lead Sulfide (PbS) and Iron Sulfide (FeS) is gaining more attention. The conventional inhibitors developed to tackle the formation of the most common deposition minerals do not have the same effectiveness for this type of minerals.

As these materials pose a risk to safe drilling activities, the development of more advanced tools to predict their behavior at extreme conditions bring new light into addressing the scaling problem. The aim of this work is to develop a method for measuring the solubility of ZnS, FeS and PbS and determine the solubility at high temperatures. The experimental data are intended to be used for parameter estimation in the Extended UNIQUAC model.

1.2 High Pressure High Temperature Reservoirs

These reservoirs at extreme conditions have been classified based on pressure and temperature in three categories: high pressure and high temperature (HPHT), ultra-high pressure and high temperature (Ultra-HPHT) and HPHT-hc. The high-pressure high-temperature reservoirs (HPHT) are defined as those reservoirs at pressures above 689.5 bar (10.000 psi) and 148.8 °C (300˚F). At more extreme conditions are the Ultra-HPHT reservoirs at temperatures and pressures greater than 205°C

and 1380 bar respectively. The HPHT-hc reservoirs are at conditions that exceed 260°C and 2410 bar. The characteristics of the HPHT-hc are more commonly found in geothermal reservoirs than in oil reservoirs [1,2]. The limits that define the type of reservoir are shown in Figure 1.1. Examples of reservoirs that are considered as HPHT are presented in Table 1.1.

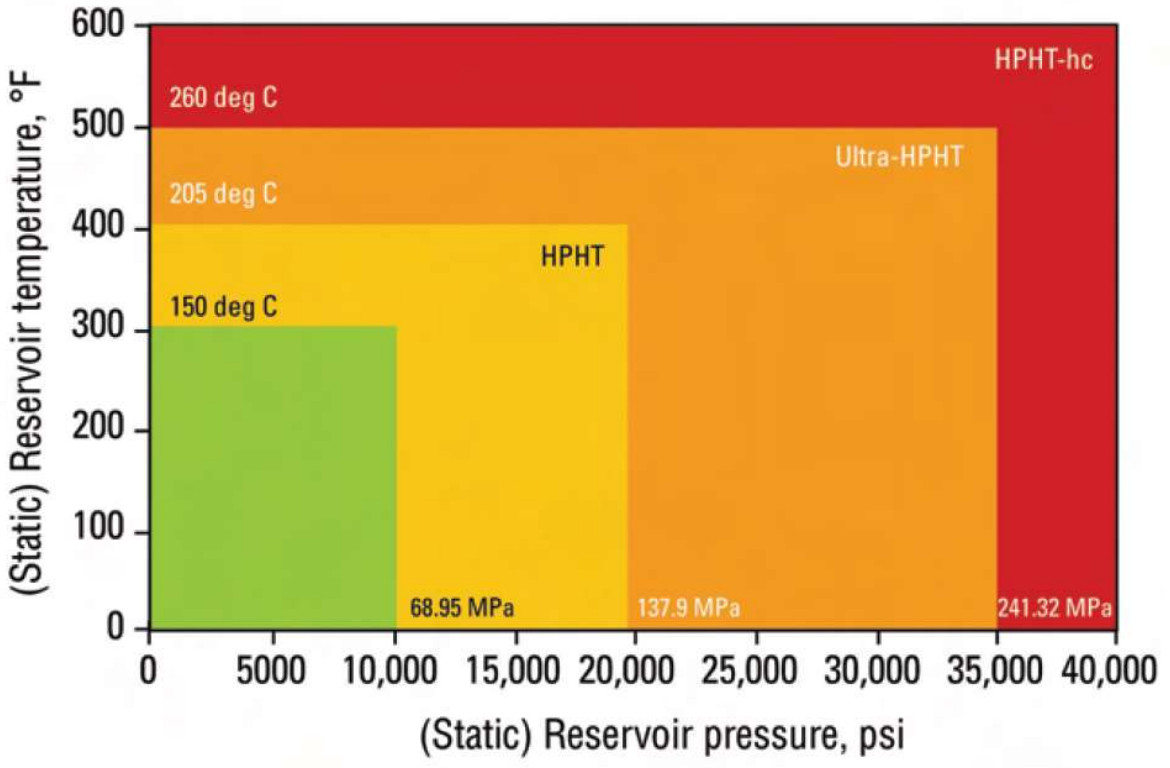

Figure 1.1 Characteristics of HPHT reservoirs. (Image taken from [3])

Ions such as Ca^{2+}, Mg^{2+}, and SO_4^- among others are present either in oil, the formation waters or in the water that is injected to the reservoir to recover the oil. The changes in pressure and temperature during the extraction process of oil alter the equilibrium of the aqueous system. Consequently, a precipitate known as scale is formed.

Scale is the deposition of a compound when the solubility of the compound has exceeded its solubility limit (auto-scaling). The deposition of these materials occurs when the equilibrium of the saturated solution is disturbed. Other events that disturb the equilibrium are the evaporation of the aqueous phase due to sudden changes in temperature (evaporation-induced scale), release of H_2S and or CO_2 present in the aqueous phase. Another cause of scale formation is the chemical incompatibility between formation waters and/or injection waters. The chemical incompatibility is referred as the reaction between ions present in the waters, forming new compounds of lower solubility with

subsequent precipitation. The produced water becomes supersaturated and scale is formed when the "incompatible" waters meet downhole (incompatible-mixing scale). The secondary recovery by injecting or flooding of a well with CO_2 triggers the formation of carbonate scale (gas flooding scale) [4–7].

Scale formation is one of the main problems to address during the extraction of oil from HPHT reservoirs. The presence of scaling at the oil reservoir will cause flow restriction, decreasing the production of the well and therefore the operational costs (OPEX) of the well will rise. Additionally, more frequent maintenance is needed and in some cases emergency shutdowns are required to keep the integrity of the well [7–9].

Table 1.1 HPHT Reservoirs and their characteristics

Field Name	Pressure (bar)	Temperature (°C)	Depth (km)	Type	Formation Waters	Reference
Elgin and Franklin [a]	1100	190	5	Gas condensate	Zn 300 ppm Fe 528 ppm Pb 300 ppm	[10,11]
Puffin [a]	1240	179	4.5	Gas condensate	N.A.	[12,13]
Culzean [b]	938	173	4.5	Gas condensate	Zn 572 ppm Pb 218 ppm	[12,14]
Gulf of Mexico	1240	177 – 204	5	Oil and gas condensates	Zn 245 ppm Pb 70 ppm	[15,16]
Svane [b]	1300	179	6	Gas condensate	N.A.	[12]
Morvin [b]	800	150	4.5	Gas condensate	N.A.	[12,17]
Erskine [a]	965	176	4.5	Gas Condensate	N.A.	[18,19]
Glenerlg [a]	1000	200	5.8	Gas condensate	N.A.	[9]

[a] United Kingdom Sector

[b] North Sea

The most common scaling minerals are $BaSO_4$ (barite), $CaCO_3$ (calcite) and $SrSO_4$ (celestite) among other minerals. Lately a new type of scaling materials has been found in oil reservoirs: sulfides.

Sulfide scaling minerals are formed as a result of the reaction of hydrogen sulfide and metallic ions present in the well. The origin of the metallic ions is diverse, for example zinc and lead are commonly present in the formation waters of the reservoir while the presence of iron is directly correlated to corrosion of pipe lines, accessories or instruments in the well. A well-known sulfide scaling case in HPHT reservoirs is the Elgin and Franklin field. Initially, the formation of $CaCO_3$ was expected and later identified in the well. However, this was not the only type of mineral found after the Elgin and Franklin field started production. The presence of ZnS and FeS was then identified and it was located at the surface choke (at approximately 90 °C). The sulfide minerals were not contemplated during the scaling risk assessment of the field. As a consequence, the well was shut in and the squeeze treatments intended to tackle $CaCO_3$ did not perform well for ZnS and FeS [10].

The risk of sulfide scaling increases as H_2S is present at high concentrations. For example, the analysis run for the Glenelg field shows elevated levels of H_2S (300 ppm) and the presence of Zn and Pb in the formation waters. Furthermore, the petrographic analysis has shown the presence of sphalerite, pyrite and iron minerals. Therefore, sulfide scaling at the Glenelg field is imminent [9,19].

In HPHT reservoirs, the evaporation of water is the main reason for super-saturation of scale minerals. The capacity of evaporation of a reservoir can be increased by the inverse Joule Thomson Effect [20]. The inverse Joule Thomson Effect (JTE) is stated as an increase in temperature at adiabatic conditions during the expansion of a fluid. The JTE is referred as a change in temperature associated to a change of pressure in the absence of heat transfer and shaft work. Generally, the JTE has been studied for fluids in gas phase and it has been concluded that a decrease in temperature is expected. However, the JTE is not only limited to fluids in gas phase and the final temperature after a change in pressure can either increase or decrease.

The increase of temperature due to the inverse Joule Thomson Effect (JTE) can cause serious operational problems in different processes. For instance, in a geothermal reservoir, i.e. a brine system at high pressure, the decompression process may lead to sudden evaporation of the aqueous phase. and consequently, the minerals will precipitate. The resulting scaling can plug the pipes and block fittings among other problems.

As mentioned above the Joule Thomson Effect plays a considerable role when extracting oil at high pressure and high temperatures. The increase of temperature when the oil is extracted will alter the equilibrium of the minerals that are dissolved in the aqueous phase. These minerals will deposit in the form of scale in the equipment and pipes in the reservoir.

Scale remediation is a very expensive practice that can be prevented. It is more important to think that the control of scale adds value to the well since the production of oil can be increased and therefore revenue obtained from the well will raise [21]. As the first step in the prevention of scaling it is important to identify and characterize the minerals present in the well. The latest constitutes one of the main reasons why this project is conducted. Solubility data of scaling minerals at high pressure and high temperatures is scarce. The saturation index determination of scale minerals as a function of temperature and pressure will provide valuable information regarding to the solubility of minerals at high pressures and temperatures.

Limited exploration has been done on solubility of sulfides. The solubility data around sulfides differ in several ways, from differences on the starting material to addition of other compounds e.g. to control pH or modify salinity that ultimate will hinder the effect of a single variable. Therefore, comparison between published data results cumbersome and in some cases ill-suited.

Thus, this research work was intended to design an experimental set-up and develop a method to determine the solubility of Zinc, Iron and Lead Sulfides at conditions similar to HPHT reservoirs.

1.3 Experimental Determination of Solubilities

The solubility experiments require a series of considerations to obtain accurate experimental data. A list of the most important and relevant aspects taken into account in this study are listed as follows [22,23].

1. Purity of the materials: The presence of impurities in the starting solid can interfere during the solubility measurements. Undesirable interactions between ion in the aqueous phase can take place and therefore erroneous interpretations of the solubility values obtained are made. The impurities not only interfere during the experiments, they also affect the determination of the concentration in the aqueous phase. For example, conductivity measurements are particularly sensitive to impurities, since this method is not specific for a targeted element. CO_2 present in the atmosphere can interfere the conductivity measurements.
2. Nature of the starting solid: Minerals exhibit different crystalline forms that exhibit different magnitudes of solubility. Thus, it is important to identify the crystal form previous carrying the laboratory work. On the other side mineral and precipitated forms differ in solubility

values as well. One of the main reasons it is the “aging” that the material has undergone for million years, making it hard to solubilize.

3. Particle size: The particle size of the solid plays a vital role during the experiments. Firstly, the size of the particles will dictate the dissolution rate, as fine particles will dissolve faster than coarse ones due to higher surface area. On the other side, during the phases separation it is important that very fine particles are collected and separated from the aqueous phase. Failure to do so will interfere in the reading of the results.
4. Regulation and measurement of temperatures and pressure.
5. Establishment of adequate solubility equilibrium: This is a crucial step during the determination of solubility. The experimenter has to keep track on a variable (i.e. pH, concentration, etc.) to decide when the solid and the liquid phase are in equilibrium. The equilibration time depends on several variables. Among those are:
    a. Agitation: active agitation is required in order to guarantee the saturation of the solvent.
    b. Duration: Allowing the solid and the liquid phases to stay in contact for sufficient time is critical when determining steady conditions.
6. Inertness of the solubility vessel: It is important to verify that the construction materials of the experimental set-up do not react with the compounds intended to study. It is important to avoid corrosion of the equipment as this will contribute to contamination of the aqueous phase.
7. Sampling and filtering: These are key steps during solubility measurements. In this step a representative sample of the solution at equilibrium conditions is withdrawn. The separation of phases is commonly achieved by direct filtration. However, disadvantages of this method arise as precipitation may occur during the filtration process. Precipitation can be avoided by keeping temperature and pressure constant during and immediately after filtration. The inertness of the membrane is also important to avoid contamination of the sample.
8. Method of analysis: The analysis method is chosen based on the order of magnitude of the solubility. Chemical analysis of the aqueous phase is the most widely used technique. The most common chemical analysis methods for solubility determination of sparingly soluble salts are:
    a. Atomic Absorption Spectroscopy (AAS)
    b. Mass Spectrometry (MS)
    c. Inductively Coupled Plasma Mass Spectrometry (ICP-MS)

d. Inductively Coupled Plasma Optical Emission Spectrometry (ICP-OES)

1.4 Thermodynamic modeling

Evaluating and predicting scaling conditions is highly valuable for the operator of a well. The potential conditions for scale formation can be detected by constant monitoring of the well. Temperature sensors, pH probes along with flow meters bring beneficial information regarding changes in chemistry in the well. However, constant monitoring does not guarantee that the occurrence of scaling can be anticipated [5].

The prediction of the occurrence of scaling materials is nowadays in high-demand. The conventional inhibitors developed to tackle the formation of the most common deposition minerals do not have the same effectiveness for this type of sulfide minerals. Instead of using a reactive approach to remove scaling in the reservoirs, a proactive approach should be implemented. Prediction of the occurrence of these scales in HPHT is a way to proactively address the scaling issue. Scaling prediction requires a highly accurate thermodynamic model capable of representing the solid-liquid equilibrium of the minerals. Scaling prediction will impact directly on the flow assurance of the reservoir, anticipating the precipitation of metallic sulfites at a determined pressure and temperature of the reservoir. Minimizing the deposition of these minerals will guarantee a continuous flow from the reservoir to the top site facility.

Among the most common models is the molality-based model of Pitzer. The Pitzer model is limited to concentrations up to 6 molal. This model has been criticized due to the unlimited number of parameters than can be fitted as increases the error propagation in the thermodynamic properties calculated by the model [24,25]. The ScaleSoftPitzer^{TM} software is one of the software based on the Pitzer's theory about electrolytes. This software is built in Excel and it is owned by the Brine Chemistry Consortium at Rice University.

The speciation-based model developed by Anderko et al. [26] is currently in use by renowned oil companies and it is commercialized by OLI Systems Inc. The model reproduces vapor-liquid, solid-liquid and liquid-liquid equilibria. The limits of the model are from infinite dilution to the fused salt limit. The model is mainly developed to represent the properties of multi-component aqueous solutions [26]. The model has been evaluated for extreme HPHT conditions at temperatures up to 300 °C and pressures up to 3500 bar in H_2S and CO_2 rich environments [27].

The experimental data obtained for ZnS, FeS and PbS in this study were used for parameter determination on the solid-liquid equilibrium calculations using the Extended UNIQUAC as thermodynamic model. The Extended UNIQUAC model is a local composition model that features several advantages compared to other models when describing the behavior of aqueous electrolytes systems. The model was presented by Thomsen and Rasmussen in 1999 [28]. The Extended UNIQUAC is combined with the Soave-Redlich-Kwong (SRK) equation of state to calculate the fugacities corresponding to the vapor phase. This model requires fewer parameters to be estimated compared to other models (i.e. Pitzer's model) therefore the propagation of error is minimized. Only a set of parameters: two parameters per species plus two parameters per species pair, is required. The parameters are adjusted against experimental data. The model accounts for the dependency of the solubility on pressure and temperature. The Extended UNIQUAC model has been previously studied by García et al. [29,30] for describing the solid-liquid equilibria of scaling minerals (carbonates and sulfates).

1.5 Objectives

This study was intended to provide data of the solubility of sulfides, in particular Zinc Sulfide (ZnS), Iron Sulfide (FeS) and Lead Sulfide (PbS) at elevated temperatures and pressures. The aim was to study the behavior of the sulfides at the conditions of High Pressure and High Temperature (HPHT) Reservoirs. The following objectives were set:

1. To estimate the Joule-Thomson Inversion Effect on final temperature in relevant brines.
2. To investigate the solid-liquid equilibrium of sulfides at HPHT conditions.
    a. To design and build an experimental set-up for measuring the solubility of sulfides.
    b. To develop a methodology for measuring the solubility of sulfides.
3. To determine the effect of pressure on solubility of sulfides.
    a. To design and build an experimental set-up for measuring the solubility of sulfides at pressures above atmospheric pressure.
    b. To develop a methodology for measuring the solubility of sulfides at pressures above atmospheric pressure.
4. To model the vapor-liquid-solid equilibrium of sulfides at HPHT conditions.

1.6 Scope of this work

The findings obtained in this research work are presented in this thesis that consists of six chapters. A brief outline of the chapters is as follows.

Chapter 2 is intended to provide an overall description of the Joule Thomson Effect (JTE). The Joule Thomson Effect is explored from its thermodynamic foundation until its application to cases such as decompression of pure water, brine and oil-brine mixtures. The cases are studied at pressure and temperatures relevant to HPHT reservoirs. This work was presented at the Society of Petroleum Engineers One Day Seminar in Bergen (Norway).

Chapter 3 presents the experimental work carried out to measure the solubility of Zinc Sulfide (ZnS). A borosilicate glass set-up was designed to determine the solubility and it is presented in this chapter. The set-up is intended to perform experiments at atmospheric pressure and temperatures up to 80 °C. The methodology developed is explained in detail from the challenges encountered during the experiments such as fine particles in the aqueous phase until the step by step on how the experiments were conducted. A brief description of the analytical technique chosen (Inductively Coupled Plasma Optical Emission Spectrometry) is included in this chapter. Key aspects for solubility measurements such as determination of the time required to reach steady conditions and effect of temperature were explored. This work was presented at the Society of Petroleum Engineers Oil Field Scale in Aberdeen (United Kingdom). An adaptation of this chapter was published in the Journal of Solution Chemistry with the tittle "Determination of Zinc Sulfide Solubility to High Temperatures"

The experimental set-up and methodology presented in Chapter 3 were used for solubility determination of Iron and Lead Sulfide as well. The results obtained are presented in **Chapter 4**. The findings were presented at the International Symposium on Solubility Phenomena and Related Equilibrium Processes (ISSP17) in Geneva (Switzerland) with the tittle "Solubility Measurements and Modeling of Zinc, Lead and Iron Sulfides at High Temperatures and High Pressures". An adaptation of this chapter was published in the Journal of Fluid Phase Equilibria with the tittle "Measurement of Iron and Lead Sulfide Solubility below 100 °C"

Experiments at higher temperature were required to get more insights regarding the solubility of sulfides at HPHT reservoirs conditions. A High Temperature Titanium Cell was designed and built to carry on solubility experiments at temperatures up to 200 °C and pressures up to 60 bar. The description of the cell is presented in **Chapter 5**. The solubility of the ZnS aqueous system was explored using the HT Titanium Cell. The results obtained at temperatures between 95 °C and 175 °C are presented in this chapter. The effect of pressure was explored as well, but unfortunately no influence of the pressure on the solubility was evidenced in the range explored (from saturation pressure to 60 bars). This work was presented at the International Symposium on Solubility Phenomena and Related Equilibrium Processes (ISSP18) in Tours (France) with the tittle "Solubility Measurements of Zinc Sulfide Using A Novel High Temperature Titanium Cell"

Chapter 6 is an additional chapter in which the solubility of Iron Carbonate ($FeCO_3$) is presented. Iron Carbonate is a corrosion product that protects the pipeline infrastructure. The experience gained during the solubility measurements of sulfides allowed to participate in a Sprint Project for the Danish Hydrocarbon Research and Technology Centre (DHRTC). The aim of this project was to study the solubility of the corrosion products for understanding at which conditions create a protective layer that could prevent the corrosion of the pipelines. The results in Chapter 6 are presented in two sections (1) the synthesis of high purity $FeCO_3$ and (2) the solubility determination of $FeCO_3$ at temperatures between 25 °C and 80 °C in aqueous solutions.

Chapter 7 deals with the modelling of the solubility of ZnS, FeS and PbS. The experimental data obtained in this study presented in Chapter 3 and Chapter 4 were the input for the Extended UNIQUAC model. The experimental data were used for estimation of the single interaction parameters.

1.7 List of Published Manuscripts and Conference Contributions

A list of the scientific manuscripts published during the PhD program and the contributions to international conferences is presented as follows:

Peer-reviewed articles

Figueroa, D. C., Fosbøl, P. L., & Thomsen, K. (2015, April 22). Risk Associated with The Decompression of High Pressure High Temperature Fluids - Study on Black Oil. Society of Petroleum Engineers. doi:10.2118/173846-MS

Figueroa, D. C., Fosbøl, P. L., & Thomsen, K. (2016, May 11). Prediction and Experimental Determination of the Solubility of Exotic Scales at High Temperatures - Zinc Sulfide. Society of Petroleum Engineers. doi:10.2118/179877-MS

Murcia, D. C. F., Fosbøl, P. L., Thomsen, K., and Stenby, E. H. (2017). Determination of Zinc Sulfide Solubility to High Temperatures. Journal of Solution Chemistry, 46(9-10), 1805-1817.

Figueroa, D. C. Fosbøl, P. L., & Stenby, E. H. And Thomsen, K., Measurement of Iron and Lead Sulfide Solubility below 100 °C. Fluid Phase Equilibria (*accepted, July 2018*)

Conferences

Figueroa, D. C., Fosbøl, P. L., & Thomsen, K. (2015, April 22). Risk Associated with The Decompression of High Pressure High Temperature Fluids - Study on Black Oil. Society of Petroleum Engineers (SPE) One Day Seminar. 22 April 2015. Bergen, Norway (Oral Presentation).

Figueroa, D. C., Fosbøl, P. L., & Thomsen, K. Prediction and Experimental Determination of the Solubility of Exotic Scales at High Temperatures - Zinc Sulfide. Society of Petroleum Engineers (SPE) Oilfield Scale Conference and Exhibition. 11-12 May 2016. Aberdeen, United Kingdom (Oral Presentation).

Figueroa, D. C., Fosbøl, P. L., & Thomsen, K. Solubility Measurements and Modeling of Zinc, Lead and Iron Sulfides at High Temperatures and High Pressures. Geneva, Switzerland (Oral Presentation).

Figueroa, D. C., Fosbøl, P. L., & Thomsen, K. Solubility Measurements and Modeling of Zinc, Lead and Iron Sulfides at High Temperatures and High Pressures. International Symposium on Solubility Phenomena and Related Equilibrium Processes (ISSP17). 24-29 July 2016. Geneva, Switzerland (Oral Presentation).

Figueroa, D. C., Fosbøl, P. L., & Thomsen, K. Solubility Measurements of Zinc Sulfide Using A Novel High Temperature Titanium Cell. International Symposium on Solubility Phenomena and Related Equilibrium Processes (ISSP18). 15-20 July 2018. Tours, France (Oral Presentation and Poster)

References

[1] C. Avant, S. Daungkaew, B.K. Behera, S. Danpanich, W. Laprabang, I. De Santo, G. Heath, K. Osman, Z.A. Khan, J. Russell, P. Sims, M. Slapal, C. Tevis, Testing the limits in extreme well conditions, Oilf. Rev. Oilf. Rev. 24 (2012) 4–19.

[2] G. DeBruijn, C. Skeates, R. Greenaway, D. Harrison, M. Parris, S. James, F. Mueller, S. Ray, M. Riding, L. Temple, High-pressure, high-temperature technologies, Oilf. Rev. 20 (2008).

[3] A. Belani, S. Orr, A Systematic Approach to Hostile Environments, (2008). doi:10.2118/0708-0034-JPT.

[4] A. Eseosa, A. Atubokiki, Prediction and Monitoring of Oilfield Carbonate Scales Using Scale Check, SPE Annu. Int. Conf. Exhib. (2011) 1–10. doi:10.2118/150797-MS.

[5] M. Crabtree, D. Eslinger, P. Fletcher, M. Miller, A. Johnson, G. King, Fighting scale—removal and prevention, Oilf. Rev. 11 (1999) 30–45.

[6] G. Atkinson, M. Mecik, The chemistry of scale prediction, J. Pet. Sci. Eng. 17 (1997) 113–121. http://www.sciencedirect.com/science/article/pii/S0920410596000605.

[7] R. Gomes, E.J. Mackay, R.H. Deucher, M.C.M. Bezerra, F.F. Rosario, M.M. Jordan, Impact of Reservoir Reactions on Thermodynamic Scale Predictions, (2012). doi:10.2118/155255-MS.

[8] A. Eseosa, A. Atubokiki, Prediction and Monitoring of Oilfield Carbonate Scales Using Scale Check, SPE Annu. Int. Conf. Exhib. (2011) 1–10. doi:10.2118/150797-MS.

[9] C. Okocha, K.S. Sorbie, C. Hurtevent, S. Baraka-Lokmane, M. Rossiter, Sulphide Scale (PbS/ZnS) Formation and Inhibition Tests for a Gas Condensate Field with Severe Scaling Conditions, SPE Int. Oilf. Scale Conf. Exhib. (2014). doi:10.2118/169798-MS.

[10] G.M. Graham, C.S.A. MacPherson, C. Simpson, K. Orski, S.M. Heath, Development of Appropriate Test Methodologies for the Selection and Application of Lead and Zinc Sulphide Inhibitors for the Elgin/Franklin Fields, Soc. Pet. Eng. (2006).

[11] S. Baraka-lokmane, C. Hurtevent, H. Zhou, P. Saha, N. Tots, F. Rieu, TOTAL ' s Experience on the Development and Implementation of a Scale Management Strategy in Central Graben Fields, (2014) 1–17.

[12] V.M. Limited, Offshore Technology, (n.d.). https://www.offshore-technology.com/.

[13] R.A. McCartney, P. Winefield, P. Webb, O. Kuhn, Spatial variations in the composition of formation waters from the central North Sea: implications for fluid flow in the deep high-pressure high-temperature hydrocarbon play, Geol. Soc. London, Spec. Publ. 237 (2004) 283 LP-303. http://sp.lyellcollection.org/content/237/1/283.abstract.

[14] R.A. McCartney, S. Brice, A. Chalmers, High Pb and Zn Concentrations in Formation Water from the Culzean Field: Real or Artefact?, in: SPE Int. Oilf. Scale Conf. Exhib., Society of Petroleum Engineers, 2016.

[15] J.K. Daniels, I.J. Littlehales, L. Lau, S. Linares-Samaniego, Laboratory Methods for Scale Inhibitor Selection for HP/HT Fields, Soc. Pet. Eng. (2014).

[16] M.M. Jordan, K. Sjursaether, M.C. Edgerton, R. Bruce, Inhibition of Lead and Zinc Sulphide Scale Deposits Formed during Production from High Temperature Oil and Condensate Reservoirs., in: SPE Asia Pacific Oil Gas Conf. Exhib., Society of Petroleum Engineers, 2000.

[17] Norwegian Petroleum Directorate, Norwegian Petroleum Directorate, (n.d.). http://www.npd.no/.

[18] R.F. Allen, M. Walters, Erskine Field: Early Operating Experience, Offshore Eur. Oil Gas Exhib. Conf. (1999). doi:10.2118/56899-MS.

[19] G.S. Elliott, R.A. Brockman, R.M. Shivers III, HPHT Drilling and Completion Design for the Erskine Field, Offshore Eur. (1995). doi:10.2118/30364-MS.

[20] S. Baraka-Lokmane, C. Hurtevent, H. Zhou, P. Saha, N. Tots, F. Rieu, TOTAL ' s Experience on the Development and Implementation of a Scale Management Strategy in Central Graben Fields, Soc. Pet. Eng. (2014) 1–17. doi:10.2118/169757-MS.

[21] J. Vetter, Oil field Scale - Can we handle it?, J. Pet. Technol. 28 (1976) 1402–1408.

[22] R.P.. Hefter, G.T; Tomkins, ed., The Experimental Determination of Solubilities, John Wiley & Sons, 2003.

[23] J. Zimmerman Howard K, The Experimental Determination of Solubilities., Chem. Rev. 51 (1952) 25–65.

[24] D. Rowland, E. Königsberger, G. Hefter, P.M. May, Aqueous electrolyte solution modelling: Some limitations of the Pitzer equations, Appl. Geochemistry. 55 (2015) 170–183.

[25] K. Thomsen, Electrolyte solutions: thermodynamics, crystallization, separation methods,

DTU Chem. Eng. Tech. Univ. Denmark. (2009). http://orbit.dtu.dk/files/131770579/ElectrolyteCompendium.pdf .

[26] A. Anderko, P. Wang, M. Rafal, Electrolyte solutions: from thermodynamic and transport property models to the simulation of industrial processes, Fluid Phase Equilib. 194 (2002) 123–142.

[27] R.D. Springer, P. Wang, A. Anderko, Modeling the Properties of H2S/CO2 /Salt/ Water Systems in Wide Ranges of Temperature and Pressure, SPE J. (2015). doi:10.2118/173902-PA.

[28] K. Thomsen, P. Rasmussen, Modeling of vapor-liquid-solid equilibrium in gas-aqueous electrolyte systems, Chem. Eng. Sci. 54 (1999) 1787–1802. http://www.sciencedirect.com/science/article/pii/S0009250999000196.

[29] A. Villafáfila Garcia, K. Thomsen, E.H. Stenby, Prediction of mineral scale formation in geothermal and oilfield operations using the extended UNIQUAC model: part I. Sulfate scaling minerals, Geothermics. 34 (2005) 61–97.

[30] A.V. García, K. Thomsen, E.H. Stenby, Prediction of mineral scale formation in geothermal and oilfield operations using the Extended UNIQUAC model: part II. Carbonate-scaling minerals, Geothermics. 35 (2006) 239–284.

CHAPTER 2

Joule Thomson Effect

2.1 Introduction

The increase of temperature while decompressing a fluid as a result of the inverse Joule Thomson Effect can cause serious operational problems in different processes. For instance, in a geothermal reservoir, i.e. an aqueous electrolyte system at high pressure, the decompression process might lead to sudden evaporation of the aqueous phase and consequently precipitation of the salts present. The precipitation of salts can generate scaling, causing problems of clogging pipes among other problems. This anomalous behavior that pure liquid water exhibits, is somehow surprising since based on the classic definition of the Joule Thomson Effect a decrease in temperature is expected.

The change in temperature associated with a change in pressure was first studied by Joule and Thomson through an experiment in which a gas was expanded to a lower pressure through a porous barrier [1]. The apparatus was insulated to guarantee an adiabatic process. They observed a temperature decrease upon expansion of the gas. This phenomenon is called the Joule-Thomson Effect. The expansion of a real gas at isenthalpic conditions leads to a decrease in temperature [2]. The Joule-Thomson effect is related to the non-ideal behavior of the fluid.

Based on the classic definition explained above, the inverse JTE stands for an increase of temperature during the expansion of a fluid. A decrease (JTE) or an increase in temperature (inverse JTE), is directly correlated to the inversion temperature of the fluid, which depends on the physico-chemical and thermodynamic properties of the fluid and the initial temperature and pressure of the process. For example, in the case of Argon (Ar) and carbon dioxide (CO_2) the inversion temperatures are 450 °C and 1227 °C respectively at 1 atm. If a decompression process takes place at a temperature of 527 °C, a cooling effect will occur in the case of CO_2 (JTE) but in the case of Ar, heating will take place due to the initial temperature being higher than the inversion temperature for Ar [2,3]. Many compounds

like Argon and CO_2 behave as expected and cool down during expansion below the Joule-Thomson inversion temperature. Liquid water on the other hand heats at expansion at temperatures below 250 °C.

The JTE plays a role in large scale processes such as fluid processing, flow rate measurement, cryogenics, oil production, injection of CO_2 into depleted gas reservoirs [4], seismic slip [5] or at small scale like high pressure liquid chromatography (HPLC).

The Joule-Thomson effect has mostly been studied for the expansion of gases and implemented for the liquefaction of gases and refrigeration cycles (e.g. Linde refrigerator), but this effect is also observed for expansion of liquid and solid phases. The gaseous condition under which the Joule-Thomson experiment originally was carried out is not a requirement, as mentioned by Adkins [6] and by Atkins and Paula [2].

In the context of gases, a cooling effect is expected in the decompression during an adiabatic throttling process [7]. For example, during the injection of CO_2 into depleted gas reservoirs, the expansion of the gas will lead to a cooling effect. If the Joule-Thomson effect is not taken into account, the decrease in temperature may cause problems such as CO_2 and/or CH_4 hydrate formation, or freezing of the residual water limiting the injectivity of the CO_2 into the reservoir [4].

The behavior of liquid methanol in liquid chromatography is studied by Martin and Guiochon [8]. The Joule Thomson coefficient was determined for methanol in an adiabatic column at a pressure of 1000 bar and temperatures ranging from 25 – 100˚C. The Joule Thomson coefficient in this case is negative meaning that methanol temperature increased after decompression [8]. Consequently, it can be said that liquid methanol exhibits the inverse Joule Thomson effect

In the case of solids and more specifically in the case of magmas and silicate minerals that experience an expansion from the mantle of the earth from 1 GPa to 0.1 GPa and temperatures above 450 °C the Joule-Thomson coefficient is negative. As a result, an increase in temperature is observed during the decompression process and cooling upon a compression process [5,9–11].

2.2 High Pressure High Temperature (HPHT) Reservoirs

The extreme conditions found in HPHT reservoirs in terms of pressure and temperature, push the development of new technologies. These reservoirs represent a challenge in terms of safety, drilling equipment, durability of materials and operating conditions, among others [12,13]

The increase of temperature during decompression as a result of the inverse Joule-Thomson Effect (JTE) might cause operational problems in HPHT reservoirs. The decompression might lead to sudden changes in temperature that could trigger the precipitation of salts as a result of evaporation of the aqueous phase, causing scale formation. The resulting scaling can cause problems such as clogging of pipes and fittings. Predicting the temperature profile upon decompression is a crucial task on operating HPHT reservoirs, to guarantee a safe procedure and to meet regulations criteria.

Lately, JTE has gained attention in reservoir engineering, which deals with planning and operation of the reservoir [14]. New oil and gas reservoirs at high pressure and high temperature are being developed, which require special attention. Challenges arise for drilling and operating conditions since the change in temperature that the fluids experience might compromise the process itself in terms of a safe operation. For hydrocarbon and gas production, a decrease in temperature during expansion is expected (related to the gas phase) but an increase of the temperature is actually observed in the case of production in High Pressure and High Temperature reservoirs (HPHT) with temperatures up to 250 °C and pressures up to 120 MPa [15,16]. The JTE phenomenon was studied experimentally by Jones [17] and Kortekaas et al. [18] and Baker & Price [9] who pointed out the increase of temperature from the bottom hole of the well during production. The production test showed an increase between 2 – 9 °C [9,17,18].

The results obtained by Kortekaas et al. [18] for gas condensates at HPHT conditions are presented in Figure 2.1. The calculations are done assuming an isenthalpic process. It is highlighted by the authors that the increase in temperature is larger as the molecular weight of the hydrocarbon increases. The largest increase (approximately 40 °C) is obtained for a North Sea Black Oil identified in Figure 2.1 as OIL2MW.

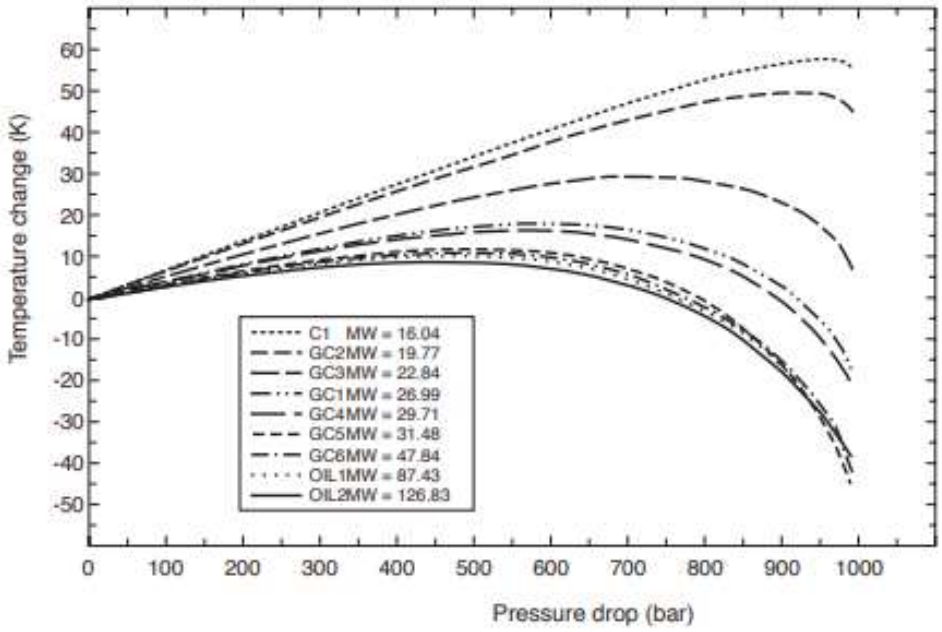

Figure 2.1 Temperature change vs pressure drop as function of composition. From the legend the molecular weight of the hydrocarbons increases from top to bottom. Image taken from Kortekaas et al. [18]

Studying the JTE and its inversion is of utmost importance since these effects may drive adverse consequences in different processes if they are not considered. Instead, the JTE and the inverse JTE can be anticipated if a rigorous study is done based on the fluid characteristics and the thermodynamic analysis of the process.

There is a limited amount of knowledge regarding the JTE in HPHT reservoirs. Baker and Price [9], Jones [17] and Kortekaas et al. [18] have published studies regarding the JTE in oil reservoirs. Lang [19], Ramberg [11] and Waldbaum [20] explored the fundamentals of the JTE. This shows that there is clear need for further development on the topic. A lack of understanding and misconceptions about the adiabatic decompression process has led to wrong conclusions about the JTE in the past. This study addresses the issue using fundamental understanding of the phenomenon and reliable resources for thermodynamic property calculations.

The aim is to explore the JTE from its thermodynamic foundation until the ultimate scenario for application in the field of HPHT oil production. First, the JTE effect is studied in pure liquid water, then in aqueous solutions and lastly in heavy oil at HPHT reservoir conditions.

2.3 Methodology

The Joule Thomson effect is quantified by the Joule Thomson Coefficient (JTC), which is positive in the case of the classic definition of the JTE and negative in the case if the inverse JTE. The conventional thermodynamic definition of the Joule Thomson coefficient (μ) is [21]:

$$\mu = \left(\frac{\partial T}{\partial P} \right)_H \tag{1}$$

For an accurate description of the Joule Thomson coefficient, a thermodynamic and mathematical development of the coefficient is required. Thus, starting out from the conventional definition of the Joule Thomson coefficient shown in Eq. (1) and taking into consideration some fundamental thermodynamic relationship such as the total differential equation for the enthalpy for a homogenous fluid at a constant composition,

$$dH = \left(\frac{\partial H}{\partial P} \right)_T dP + \left(\frac{\partial H}{\partial T} \right)_P dT \tag{2}$$

where H is enthalpy, P is pressure and T is temperature

Conventionally, the adiabatic decompression is assumed to take place at constant enthalpy. Thus, Eq. (2) can be substituted in Eq. (1) obtaining an expression as follows:

$$\mu = \frac{\partial T}{\partial P} = -\frac{\left(\frac{\partial H}{\partial P} \right)_T}{\left(\frac{\partial H}{\partial T} \right)_P} \tag{3}$$

where μ is the Joule Thomson coefficient.

The term $\left(\frac{\partial H}{\partial T} \right)_P$ is the definition of the heat capacity at constant pressure C_P, thus Eq. (3) can be written as follows:

$$\mu = \frac{\partial T}{\partial P} = -\frac{1}{C_P} \left(\frac{\partial H}{\partial P} \right)_T \tag{4}$$

The partial derivate of the enthalpy with respect to pressure P is:

$$\left(\frac{\partial H}{\partial P}\right)_T = T\left(\frac{\partial S}{\partial P}\right)_T + V \tag{5}$$

where S is entropy and V is volume

Using the Maxwell relation $\left(\frac{\partial S}{\partial P}\right)_T = -\left(\frac{\partial V}{\partial T}\right)_P$, Eq. (5) can be expressed as [22]

$$\mu = \frac{\partial T}{\partial P} = \frac{1}{C_P}\left[T\left(\frac{\partial V}{\partial T}\right)_P - V\right] \tag{6}$$

The definition of the isobaric expansivity α is [16]:

$$\alpha = \frac{1}{V}\left(\frac{\partial V}{\partial T}\right)_P \tag{7}$$

Including the isobaric expansivity α definition in Eq. (7), Eq. (6) can be also written as:

$$\mu = \frac{\partial T}{\partial P} = \frac{V}{C_P}\left[T\alpha - 1\right] \tag{8}$$

where μ is the Joule Thomson Coefficient, C_p is the isobaric heat capacity and α is the isobaric expansivity. As can be observed in Eq. (8), the Joule Thomson coefficient is a state quantity which depends on the actual pressure and temperature.

2.4 The non-isenthalpic case

The decompression process is assumed to occur at conditions with no change of phase, thus it is completed before reaching the bubble point of the mixture. Phase change is not desired during production from a reservoir. If water evaporates, it will cause scaling. The idea is to keep the fluid in a liquid state for safe handling at the top-site. This study considers the fluid transport from down hole to the conditions before the separator. It does not consider any post processing downstream.

The model is derived by energy balances. The most general expression for the conservation of energy in a system per unit of mass is shown in Eq. (9) [19,22]

$$E = U + PV + \frac{1}{2}c^2 + gz + Q + W_s \tag{9}$$

Here E refers to the total energy of the system, U is the internal energy of the system, P is the pressure, V is the specific volume, c is the velocity, g is the gravitational acceleration, z is the elevation, Q is the heat, and W_s the shaft work transfer to the system.

Using the differential form of Eq. (9) and considering a decompression process in which no shaft work and no heat is transferred, Eq. (9) is reduced to,

$$dU + dPV + cdc + gdz = 0 \tag{10}$$

the term $dU + dPV$ equals the enthalpy dH; then Eq. (10) can be expressed as follows:

$$dH = -(cdc + gdz) \tag{11}$$

Here dH refers to the differential form of enthalpy. Eq. (11) is valid for a process which occurs at non-isenthalpic conditions with an enthalpy change that is associated to changes in potential and kinetic energy.

Starting from the energy balance in Eq. (11) a more complete expression for the Joule-Thomson coefficient can be obtained by expressing the total differential of the enthalpy [see Eq. (2)] as follows:

$$\left(\frac{\delta H}{\delta P}\right)_T dP + \left(\frac{\delta H}{\delta T}\right)_P dT = -(cdc + gdz) \tag{12}$$

The term $(cdc + gdz)$ is substituted by dE_{k+p} in Eq. (12) to obtain a more general expression of the Joule-Thomson coefficient, thus:

$$\left(\frac{\delta H}{\delta P}\right)_T dP + \left(\frac{\delta H}{\delta T}\right)_P dT = -dE_{k+p} \tag{13}$$

Using the definition for the isobaric heat capacity $C_P = \left(\frac{\partial H}{\partial T}\right)_P$ and substituting Eq. (5) and Eq. (7) into Eq. (13), after some algebraic calculations,

$$\mu = \frac{\partial T}{\partial P} = \frac{V}{C_P}\left[T\alpha - 1 - \frac{dE_{k+p}}{VdP} \right] \tag{14}$$

Here dE_{k+p} is the differential of the potential and kinetic energy, V is the specific volume and dP is the gradient in pressure.

Equation (14) shows that the contribution of the potential and kinetic energy (the term dE_{k+p}) affects the value of the Joule-Thomson coefficient, leading to different results than obtained with the expression for the conventional (isenthalpic) Joule-Thomson coefficient shown in Eq. (8). Eq. (14) is a general expression for the Joule-Thomson coefficient. When the contribution of the kinetic and potential energy is not significant, Eq. (14) is reduced to Eq. (8).

The JTC approaches discussed above, lead to different results in terms of the final temperature upon decompression, especially when the potential energy and/or kinetic energy play a considerable role. It is often implied that adiabatic decompression processes occur at constant enthalpy, but this may lead to erroneous results. Waldbaum [20] and Ramberg [11] studied the decompression process in two different scenarios. Waldbaum [20] studied the Joule-Thomson effect on minerals in geological processes. He mentioned that the decompression process takes place at isenthalpic conditions and emphasized that "the only condition to be met is conservation of enthalpy in the material undergoing decompression". Waldbaum concluded that the temperature may increase upon decompression [20]). On the other hand, Ramberg considered the significant change in potential energy involved and demonstrated that the change in temperature was less significant since the real Joule-Thomson coefficients are much smaller than those calculated by Waldbaum [11]. Lang [19] indicated that a decompression process occurring in the absence of external work and involving a significant change in potential energy cannot occur at isenthalpic conditions [19].

In this work, the final temperature is calculated using the energy balance presented in Eq. 2 at two different scenarios: 1. Isenthalpic and 2. Non-isenthalpic conditions. The properties of pure liquid water are obtained using the NIST/ASME database [23] and for the brine, the NaCl apparent molar properties are obtained using the model proposed by Archer [24].

The properties of the black oil are calculated in Aspen Plus® using the Peng-Robinson EOS [25]. The composition of the black oil is chosen from Danesh et al. [26] as a heavy oil that can be found in HPHT reservoirs. In both scenarios, the process considers the extraction of black oil confined in a

well at 150 °C and 1000 bar. In the non-isenthalpic scenario, variations of the well depth are evaluated, assuming a vertical drilling at 3 different well depths (1, 3 and 5 km).

2.5 Results

The results of the final temperature after decompression of pure liquid water, aqueous solutions and heavy oil are presented in this section.

2.5.1 Pure liquid water

The results of the JTE and inverse JTE for pure liquid water that are presented in this section and are shown as the difference in temperature ΔT (T_{final}- $T_{initial}$) versus pressure. The final temperature calculations are performed using the database based upon the International Association for the Properties of Water and Steam (IAPWS 95) formulation [23]; based on the thermodynamic conditions of the decompression process and on the physicochemical properties of liquid water. All the calculations are made on a molar basis.

For the calculation of the Joule Thomson coefficient the initial pressure and temperature of the process are set. The Joule Thomson coefficient at initial temperatures of the process between 100 and 350 ˚C against pressure is presented in Figure 2.2. There are two types of lines shown, solid lines represent the Joule Thomson coefficient at non-isenthalpic conditions meanwhile the dashed lines represent the Joule Thomson coefficient at isenthalpic conditions.

It is noticed in Figure 2.2 that there is a difference in the values for the Joule Thomson coefficient at non-isenthalpic and isenthalpic conditions. The value of the Joule Thomson coefficient at isenthalpic condition is higher than the Joule Thomson coefficient at non-isenthalpic conditions of the process. This confirms what it was stated by Ramberg [11] that at non-isenthalpic conditions the Joule Thomson coefficient should be smaller than those calculated at isenthalpic conditions. The difference is more noticeable at a higher initial temperature. At isenthalpic and non-isenthalpic conditions, the Joule Thomson coefficient increments exponentially, the highest rate is observed at an initial temperature of 350 °C. As temperature decreases the rate of the Joule Thomson coefficient decreases (see Figure 2.2).

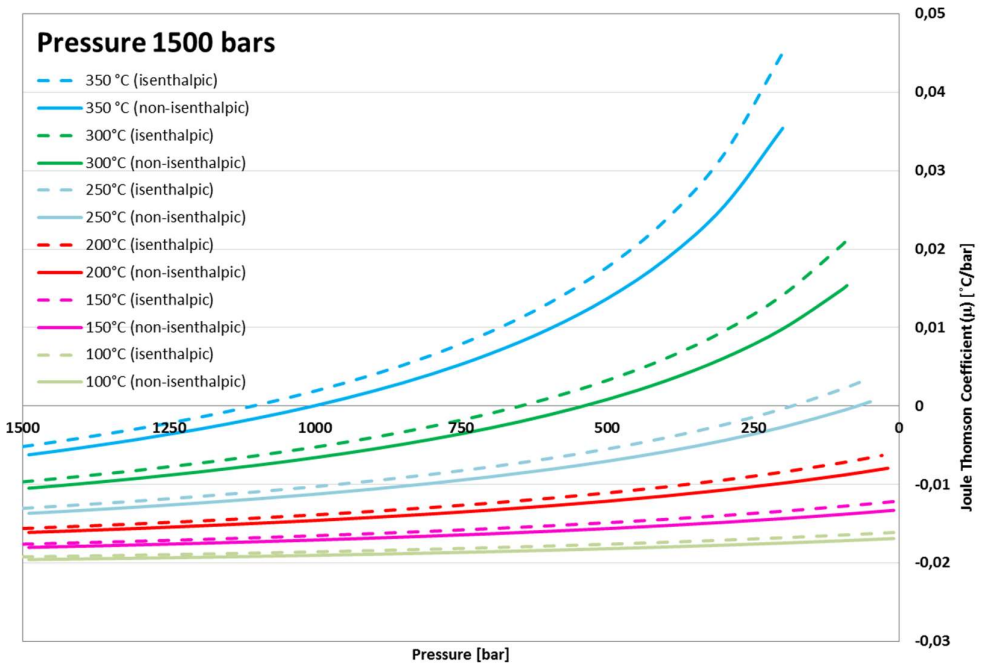

Figure 2.2 Joule Thomson coefficient for liquid water at initial pressure of 1500 bars [23].

The Joule Thomson coefficient exhibits positive and negative values (see Figure 2.2), this can be interpreted taking into account the thermodynamic definition of the Joule Thomson coefficient shown in Eq. (15).

$$\mu = \left(\frac{\partial T}{\partial P}\right) \approx \frac{\Delta T}{\Delta P} \tag{15}$$

For this specific case, decompression $\Delta P < 0$, meaning that if $\mu > 0$ Eq. (14) the final temperature of the liquid water will decrease with respect to the initial temperature at which the process started. For temperatures below 250 °C, the Joule Thomson coefficient remains negative $\mu < 0$ in which an increase in temperature is expected upon decompression. The latter confirms that under these conditions, pure liquid water increase its temperature as a consequence of the inverse JTE.

Furthermore, the effect of the initial temperature and initial pressure of the process should be explored. Hence the effect of the initial temperature and initial pressure is shown in Figure 2.3**,** Figure 3 and Figure 4 at 1500 bar, 1000 bar and 500 bar respectively. The results are presented as the change in temperature ΔT (T_{final}- $T_{initial}$) versus pressure.

Two different types of lines are shown in Figure 2.3**,** Figure 2.3, Figure 2.4; the solid lines represent the process at isenthalpic conditions, while the dash lines show the process at non-isenthalpic conditions. None of the lines end up at the same final pressure, since the calculations are done just for the conditions at which the pure water remains in liquid phase.

The process at non-isenthalpic conditions is calculated assuming that water is contained in a reservoir at 1, 3 and 5km of depth (potential energy) and that water is pumped out to surface at a velocity of 5 m/s (kinetic energy). The contribution of the kinetic energy compared to the potential energy accounts for less than 1%, thus the potential energy has the strongest influence on the non-isenthalpic process. The results at 5 km reservoir depth and 5 m/s as the velocity of pumping the fluid to the surface are plotted in Figure 2.3, Figure 2.4 and Figure 2.5. The influence of the reservoir depth on the final temperature is shown in Figure 2.6.

The change in temperature ΔT at 1500 bars (see Figure 2.3), increases as the initial temperature of the process decreases. For temperatures above 250 °C it is observed that the curves reach a maximum at which the direction of the slope changes (Joule Thomson inversion point). The difference between the non-isenthalpic and the isenthalpic process lays on the fact that the lines for the non-isenthalpic process are shifted down compared to those at isenthalpic conditions; this is due to a change in enthalpy as a result of the contribution of the potential and kinetic energy to the process. As stated by Ramberg [11] the change in potential energy "compensates for major part of the decompression" and as a consequence the final temperatures are less than those obtained at isenthalpic conditions.

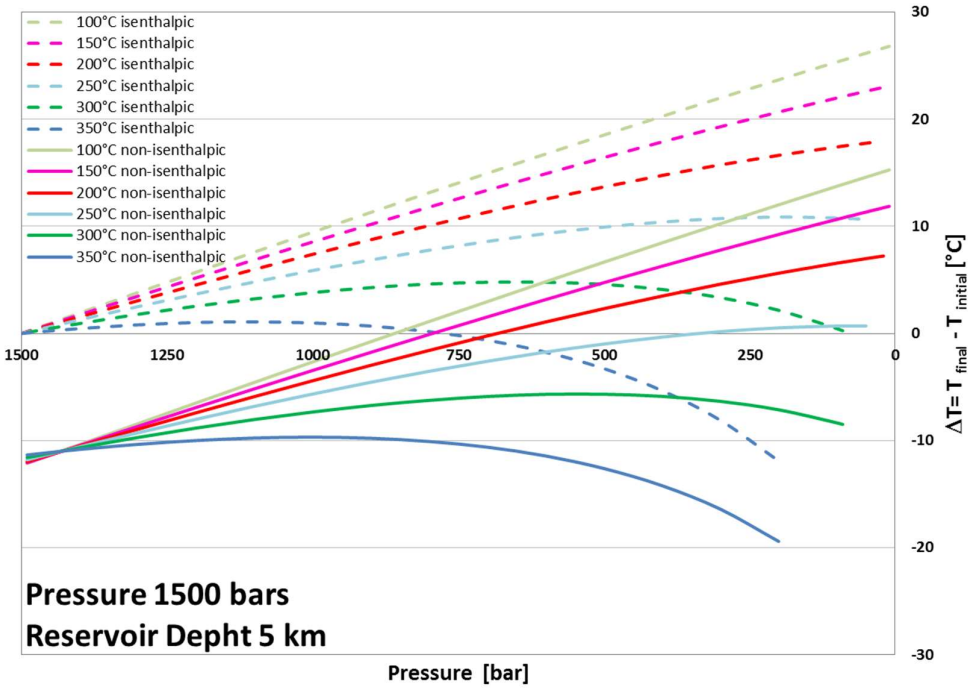

Figure 2.3 Decompression of liquid water at 1500 bar ΔT vs P at 5 km reservoir depth

It can be observed in Figure 2.3 that the final temperature (isenthalpic conditions) decreases when the initial temperature is between 300 °C and 350 °C. This trend continues at higher initial temperatures (for an isenthalpic process). On the other hand, for the decompression at initial temperatures between 100 and 300 °C ΔT is always positive at isenthalpic conditions, meaning that the final temperature increases with respect to the initial temperature, but at non-isenthalpic conditions the scenario is different. For instance, the case of initial temperature of 200 ˚C shows that the final temperature at non-isenthalpic conditions is lower than the final temperature obtained at isenthalpic conditions. If the contribution of potential and kinetic energy is neglected, e.g. initial pressure of 1500 bar and 200 ˚C as initial temperature, the final temperature of the process is over-estimated. Another interesting event is the case at an initial temperature of 300 ˚C, in which at isenthalpic conditions the increase in temperature leads to a heating effect while at non-isenthalpic conditions a cooling effect takes place. In the former case, the overall conclusion of the decompression process changes, from a heating effect (isenthalpic) to an actual cooling effect (non-isenthalpic).

Figure 2.4 presents the results for an initial pressure of 1000 bars for an isenthalpic and a non-isenthalpic process. In Figure 2.4 it can be noted that an increase in the final temperature with respect to the initial temperature is also obtained for low initial temperatures (100 – 200 °C).

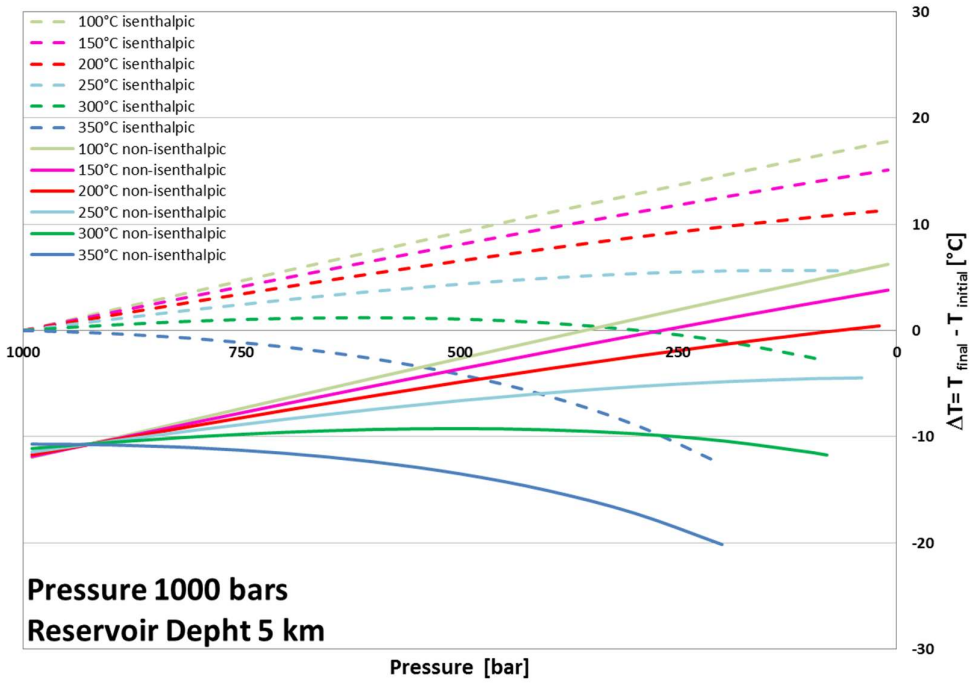

Figure 2.4 Decompression of liquid water at 1000 bar ΔT vs P at 5 km reservoir depth

Comparing the results of Figure 2.4 at 1000 bars to the results plotted in Figure 2 at 1500 bars, it can be observed that at lower initial pressure of the process, the final temperature of the process is lower. At an initial temperature of 250 °C the overall effect for a non-isenthalpic decompression process at an initial pressure of 1000 bar is a cooling effect, while in the case of 1500 bar as shown in the result Figure 2.3 is heating effect.

The analysis at 500 bars is presented in Figure 2.5 for initial temperatures between 100 °C and 350 °C. As well as presented in Figure 2.3 and Figure 2.4**,** the results for an isenthalpic and a non-isenthalpic process are compared in Figure 2.5.

For a decompression process at an initial pressure of 500 bars, it can be read from Figure 2.5 that for temperatures between 100 and 250°C an increase in temperature is obtained at isenthalpic conditions (inverse JTE). At initial temperatures between 300 °C and 350 °C a decrease in temperature is observed, meaning that the overall effect after decompression is a cooling effect. For low temperatures (100-250 °C) the heating effect dominates while the cooling effect dominates the process at high initial temperatures (300-350 °C) for an isenthalpic process. The cooling effect dominates the non-isenthalpic process at 500 bars at all the temperatures studied in this case (JTE).

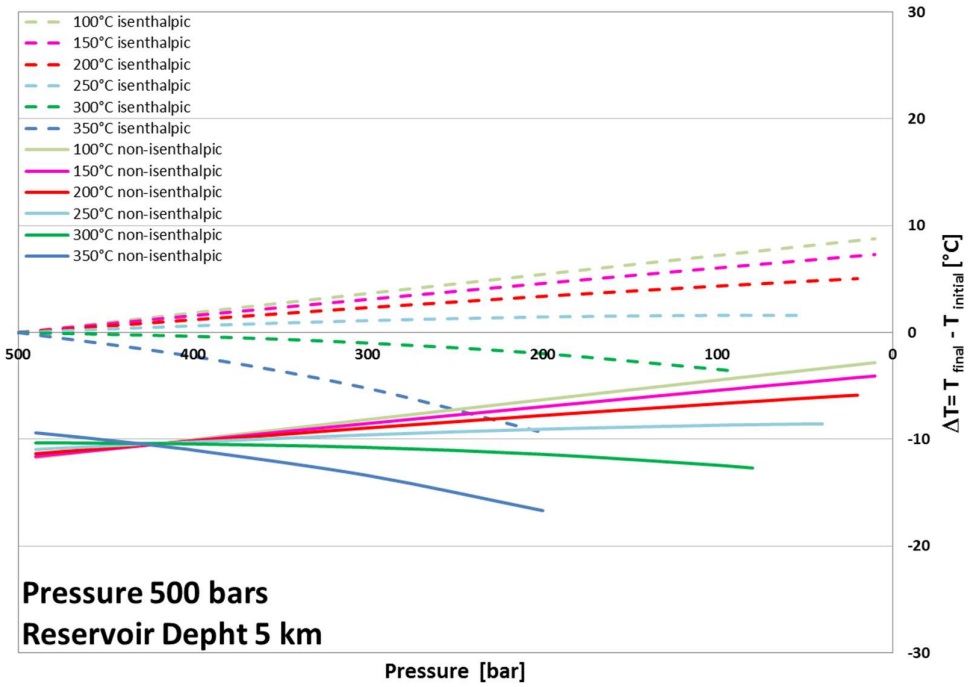

Figure 2.5 Decompression of liquid water at 500 bar ΔT vs P at 5 km reservoir depth

It is understood from the three examples shown above in Figure 2.3, Figure 2.4 and Figure 2.5 that the initial pressure plays a key role during the process. The effect of the initial pressure is proportional to the temperature increase, meaning that at high pressures higher is the increase in temperature compared to processes that occur at lower pressures. On the other hand, the effect of temperature has been found to be inverse at the lowest initial temperatures a highest increase in temperature is obtained.

The results above have shown the importance of including the contribution of the potential and kinetic energy during the decompression process. Significant differences are obtained in terms of the final temperature when the process occurs at isenthalpic or at non-isenthalpic conditions. The overall inverse Joule Thomson effect is diminished when the potential and kinetic energy terms are taken into account. In some cases, the effect is shifted, from concluding at isenthalpic conditions that a heating effect takes place to conclude that a cooling effect is in fact observed at non-isenthalpic conditions.

The effect of the reservoir depth is shown in Figure 2.6 at 1000 bars and 250 °C. The dash line represents the process at isenthalpic conditions, in that case the contribution of potential and kinetic energy is neglected. The solid lines represent the process at non-isenthalpic conditions, the potential

energy is calculated at different reservoir depths (1, 3 and 5 km) and the value for the kinetic energy is set at 5 m/s.

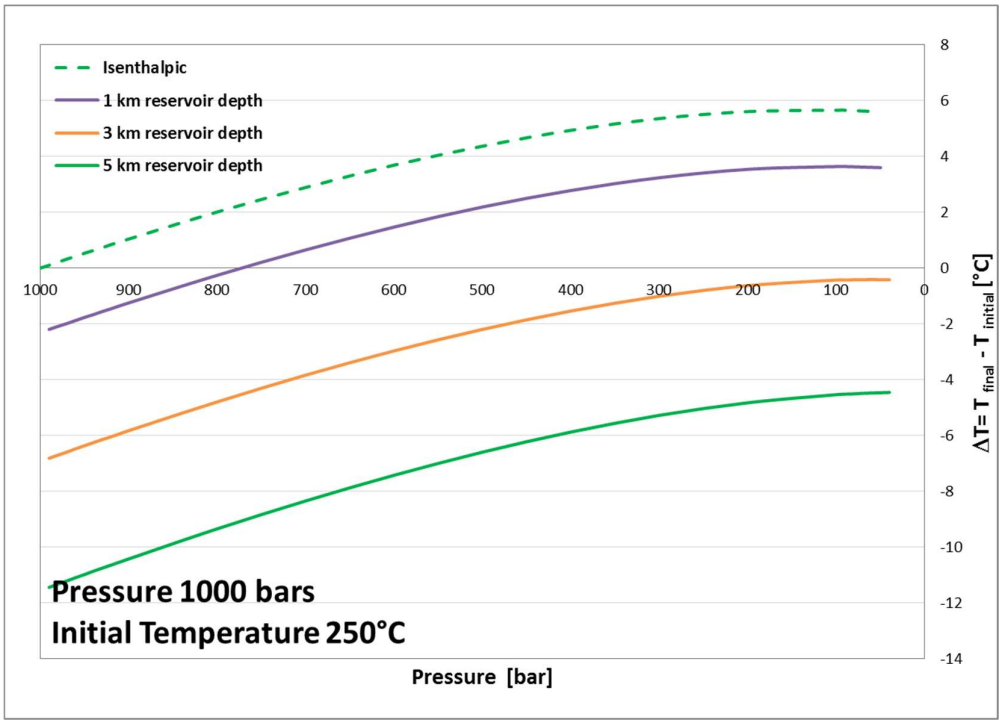

Figure 2.6 Decompression of liquid water at 1000 bar ΔT vs P at 1 km 3 km and 5 km reservoir depth

Figure 2.6 shows that as the reservoir depth increase the increase in temperature is less. Also, it is observed in that the conclusion of the overall effect can be different depending on the reservoir depth, for instance the final temperature at a reservoir depth of 1 km is higher than at 5 km; at 1 km the overall effect is a heating effect however the overall effect at 5 km is cooling when the liquid water is decompressed until 40 bars. As Figure 2.6 illustrates when the reservoir depth decreases the final temperature approaches the values of the final temperature obtained at isenthalpic conditions.

2.5.2 Aqueous solutions

The Joule-Thomson Coefficient (JTC) of aqueous solutions of NaCl at 1000 bars and 600 bars is presented in Figure 2.7. The results in Figure 2.7 are compared to the results obtained by Wood and Spera [27] at 1000 bar and 600 bar respectively. The JTC provides an approximation of the behavior of the aqueous solution of NaCl. Nonetheless the complete energy balance as mentioned before is needed to describe the process in a more accurate way.

The Joule-Thomson Coefficient (JTC) is calculated using Eq. (8). For Eq. (8) ρ, C_P and α are properties of the solution obtained from the model of Archer at different NaCl molalities [24] (valid at temperatures from -23 °C to 326 °C and pressures up to 1000 bar) .

The JTC calculated for this study are in accordance with the results presented by Wood and Spera [27] except for discrepancies observed only at 300 °C. The JTC are calculated at molalities up to 6 molal. Wood and Spera [27] predicted that the JTC should be even more negative at higher concentrations than 3 molal. This fact is corroborated as the Joule-Thomson coefficient in Figure 2.7 decreases as the NaCl concentration increases [27].

(a)

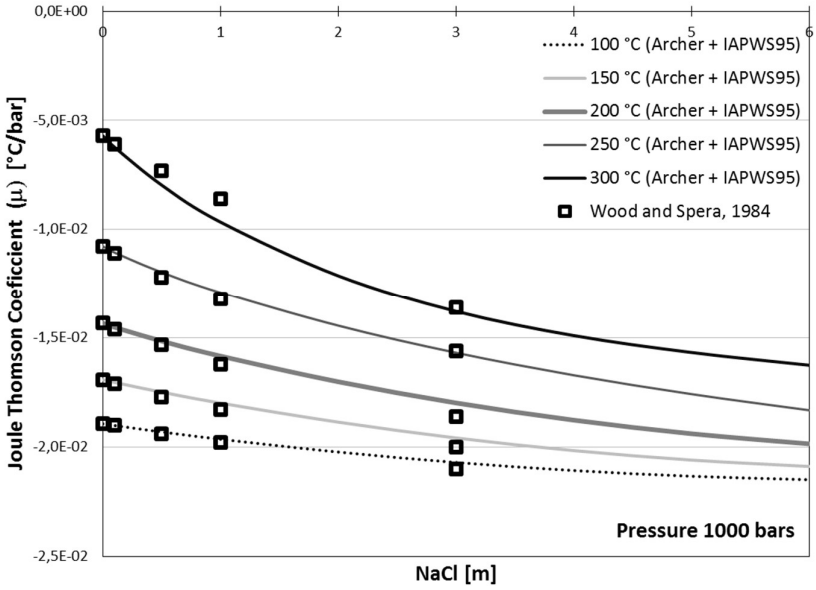

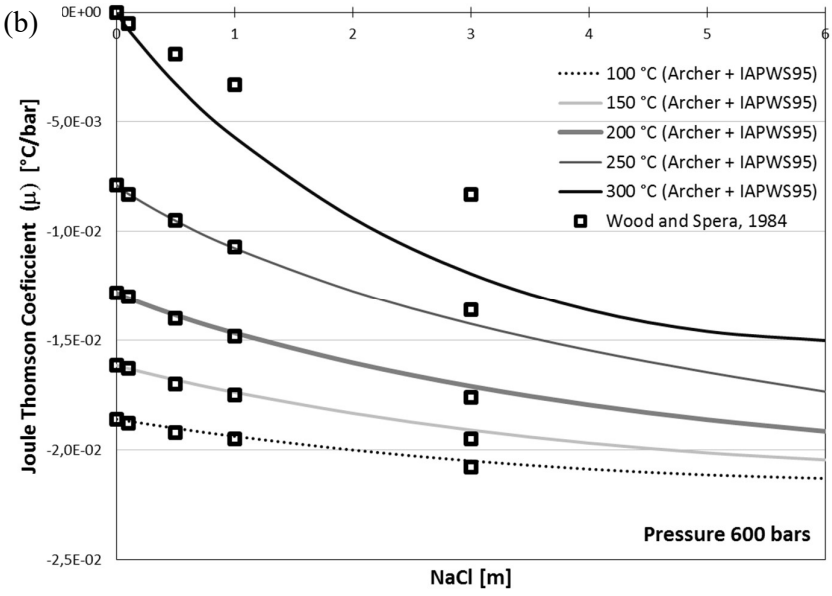

Figure 2.7 Joule-Thomson Coefficient for a NaCl solution at: (a) 1000 bar and (b) 600 bar and molalities up to 6 molal. Data shown in square dots are taken from Wood and Spera [27]. The Joule-Thomson Coefficient is calculated at initial temperatures between 100 °C and 300 °C.

Wood and Spera [27] calculated the JTC using Eq. (8) based on properties of aqueous electrolyte solutions obtained from three different sources. The specific volumes and isobaric expansivities were obtained from (valid at temperatures from 0 °C to 300 °C and pressures from 1 bar to 1000 bar). Furthermore, the isobaric expansivity values by Rogers and Pitzer [28] differ from the values obtained using Archer's model up to 26% compared to the values obtained from Archer's model [24]. The heat capacities for water were taken from Helgeson and Kirkham [29](valid at temperatures between 0 and 600 and pressures from 1 bar to 5 kbar). Wood and Spera [27] obtained the specific heat capacity from Smith-Magowan and Wood [30]. Smith-Magowan and Wood [30] measured the ratio of the heat capacity of water to the heat capacity of the aqueous solution in a differential flow heat-capacity calorimeter at NaCl molalities between 0.1m and 3.0m, temperatures between 47.40 °C and 298.99 °C and pressures between 10 bar and 177 bar. Thus, the heat capacities were not valid in the pressure range considered by Wood and Spera [27]. Differences between the values of the JTC obtained by Wood and Spera [27] and those calculated from the Archer model can be caused by differences in the properties values used for the aqueous electrolyte.

The JTC becomes more negative as NaCl molality increases as observed in Figure 2.7. This means that the final temperature after decompression is expected to be higher at high NaCl concentration than at low concentration.

The effect of pressure results in a slightly more negative JTC as illustrated in Figure 2.7. In this case, the brine solution at 1000 bars will experience a higher increase of temperature that the brine solution at 600 bars.

In order to describe the decompression path in terms of temperature change, the final temperature of the brine solution is calculated by means of an energy balance of the process. The process takes place at non-isenthalpic conditions since the potential and kinetic energy terms play a considerable role in the energy balance as demonstrated in the case of pure liquid water (see Section 2.5.1). The results are presented in Figure 2.8 as the difference between the final and initial temperatures (ΔT) versus pressure.

The JTC results in Figure 2.8 show an increase in the final temperature after decompression takes place. The effect of the initial temperature of the reservoir also is confirmed with the results in Figure 2.8. The highest temperature increase is obtained at the lowest initial temperature (100 °C). For initial temperatures above 200 °C ΔT is negative, meaning that a cooling effect takes places during the decompression of the fluid.

The temperature increase during the decompression becomes higher as the concentration of the brine increases. For example, at an initial temperature of 100˚C and a brine concentration of 0.1 molal the final temperature increases to 105.98˚C. Meanwhile, if the concentration of the brine is higher, i.e. 6.0 molal, the final temperature obtained is 106.92˚C.

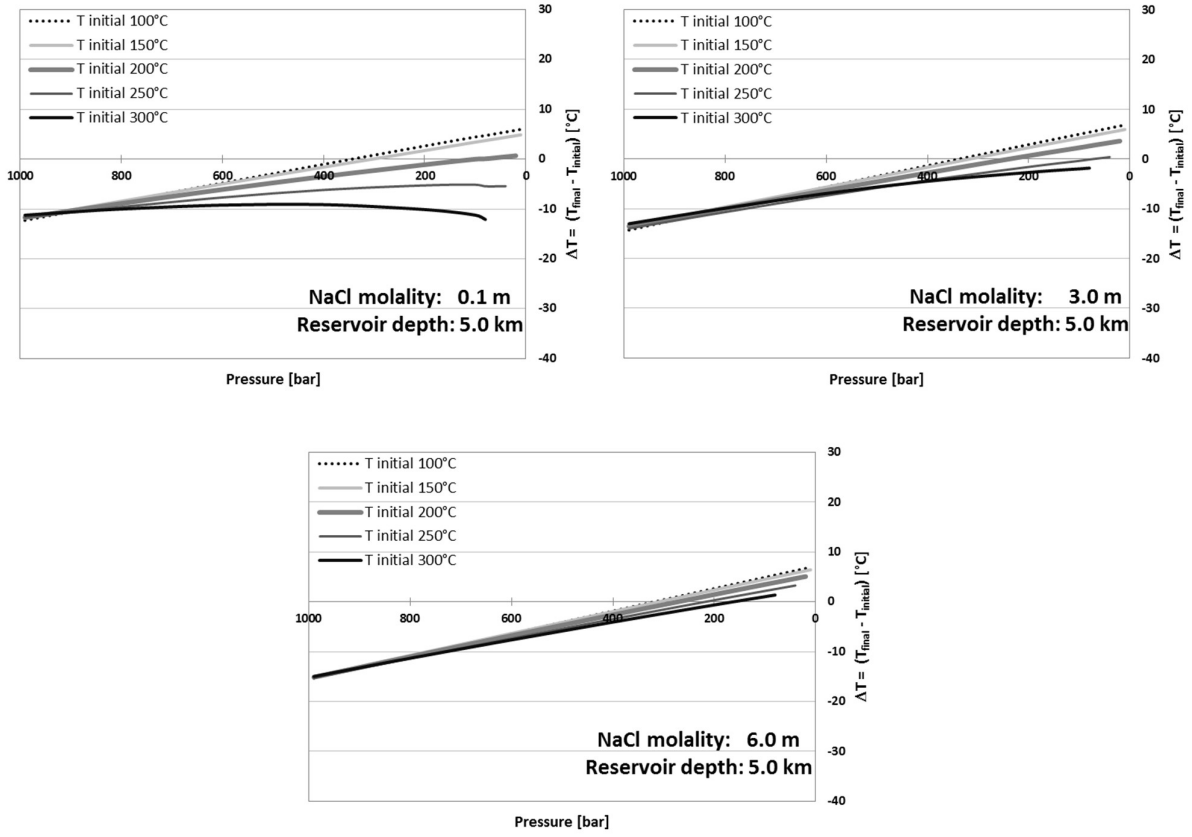

Figure 2.8 ΔT vs Pressure of NaCl at 1000 bars and initial temperatures between 100 °C and 300 °C

The effect of the addition of NaCl to pure liquid water is illustrated in Figure 2.8 for 3 different brine concentrations, ranging from 0.1 molal to 6 molal. The presence of NaCl increases the JTE as observed in Figure 2.9. The temperature increase during adiabatic decompression of a NaCl solution is higher than for pure liquid water. These observations are in agreement with the observations made by Wood and Spera [27] who pointed out that the addition of a salt to a solution will result in the decreasing of the JTC [27]. This means that a higher increase in temperature is expected upon decompression as the concentration of the NaCl increases.

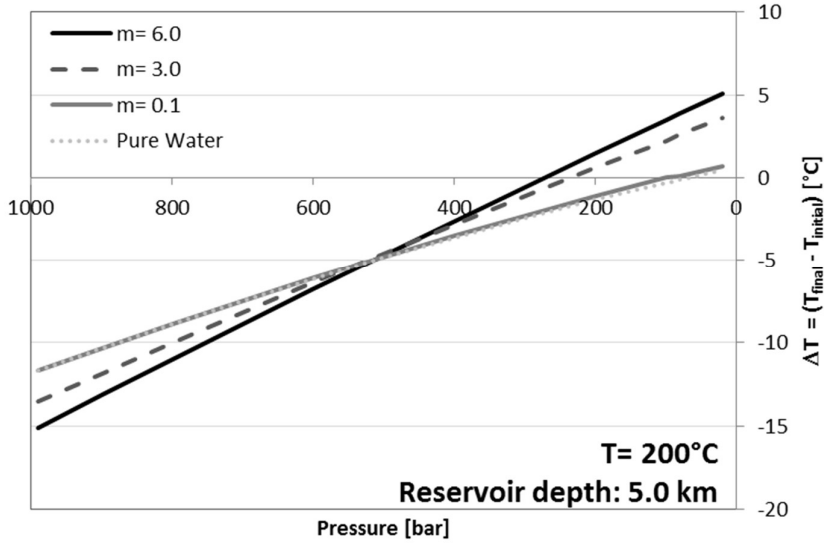

Figure 2.9 Effect of the presence of NaCl on pure liquid water during decompression.

Figure 2.10 shows the results for an initial pressure of 600 bar. The increase in the final temperature at 600 bar is lower than the increase observed at 1000 bar. For instance, at 100˚C and a concentration of brine of 6.0 molal the temperature increase at an initial pressure of 1000 bars is 5.07 °C. At 600 bar initial pressure there is no increase in temperature, rather a decrease with 3.54 °C is observed.

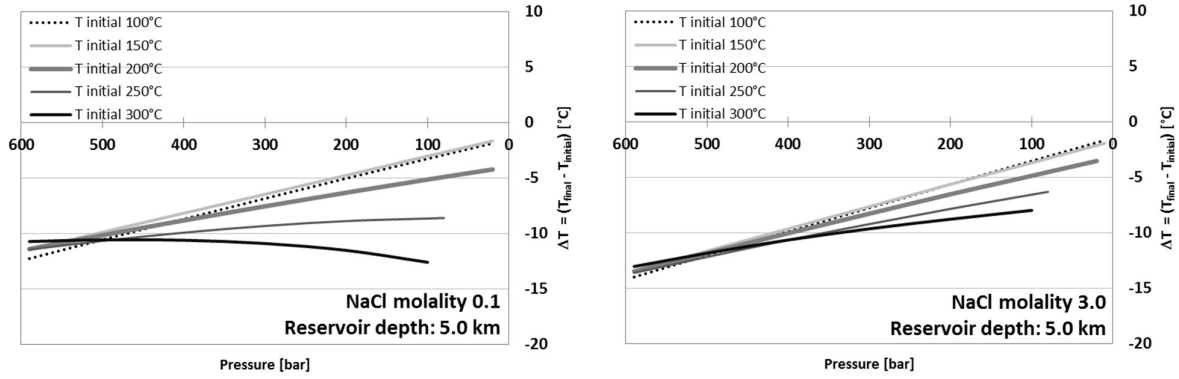

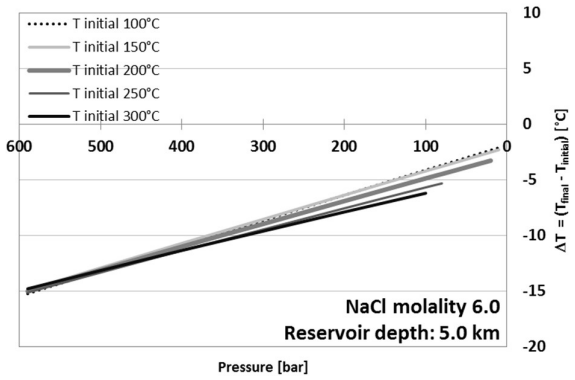

Figure 2.10 ΔT vs pressure of NaCl at 600 bars and initial temperatures between 100 and 300 °C. Dashed lines correspond to the decompression path of pure liquid water.

At 600 bar the behavior of ΔT scenario is similar as observed at an initial pressure of 1000 bar. As the initial temperature in the reservoir increases, a lower increase in the temperature is expected. Likewise, as observed at 1000 bar when the concentration of the brine increases a higher increase in the final temperature is predicted.

2.5.3 Heavy oil at HPHT reservoir conditions

The final temperature of the process after decompression is presented as follows: first the results for oil and water mixtures at isenthalpic conditions (ΔH=0) and secondly the non-isenthalpic conditions at well depths between 1 and 5 km. Finally, the impact of the presence of brine in the mixtures on the final temperature is presented. The results of the calculation are shown as temperature change from bottom hole to top-site conditions, ΔT (T_{final}- $T_{initial}$), versus pressure.

In Figure 2.11 the results for the decompression process of black oil-water mixtures are given. The final temperature is calculated assuming the decompression is taking place at isenthalpic conditions [Eq. (2) with ΔZ=0 and Δv=0]. As mentioned this is the most conservative temperature change which can be estimated.

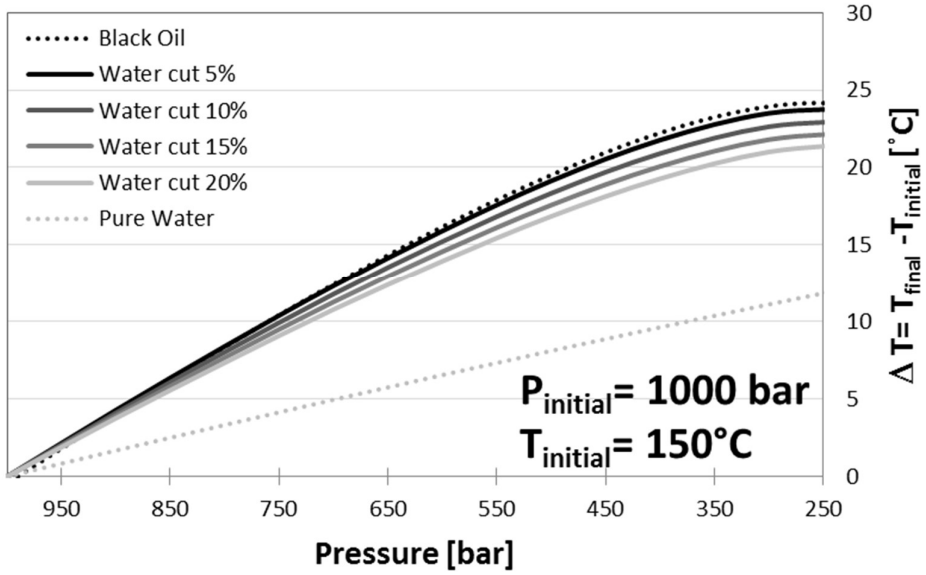

Figure 2.11 Decompression of black oil, pure liquid water and black oil-water mixtures at 1000 bar and 150 °C as initial conditions. Isenthalpic process.

The diagram outlines the positive ΔT along the decompression path. It indicates an increase in the final temperature compared to the bottom hole (BH) conditions. The highest increase in temperature is observed for black oil, up to 24.2 °C. For pure water the increase is up to 12 °C. The final temperatures of the mixtures are in-between the temperature of the black oil and pure water. It is observed that the presence of water in the black oil will diminish the heating effect, e.g. addition of an amount of water, corresponding to 5% of the oil-water mixture, will decrease the temperature 0.6˚C to 173.6˚C, at the top site. At a water cut of 20% the final temperature of the mixture is 171.3 °C starting at conditions from 150 °C.

Non-isenthalpic conditions

The impact of the well depth is illustrated in Figure 2.12, Figure 2.13 and Figure 2.14. These results are produced using a ΔZ and Δv different than 0 in Eq. (2). Figure 2.12 shows the results for the decompression of the black oil plus black oil/pure water mixture at 150 °C and 1000 bar. The well depth is set to 1 km and the velocity is 5 m/s. It is assumed the velocity in the reservoir approached 0 m/s compared to the velocity in the production pipe. The kinetic energy at the current conditions represents less than 1% of the potential energy; therefore, the change in temperature is basically related to the depth of the reservoir not so much the kinetic impact.

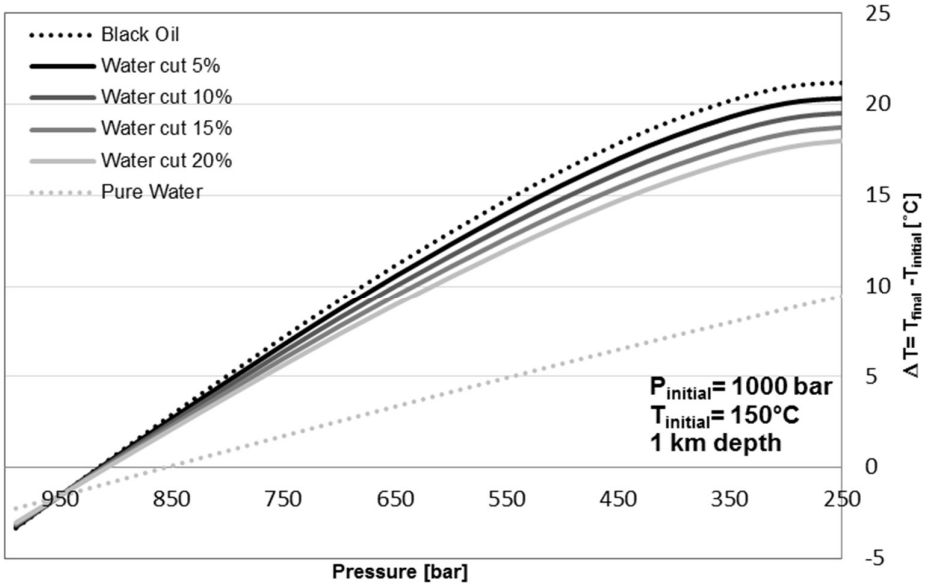

Figure 2.12 Decompression of black oil, pure liquid water and black oil-water mixtures at 1000 bar and 150 °C as initial conditions. Well depth 1 km. Non-isenthalpic process

The results show a slight reduction in the final temperature compared to the at isenthalpic conditions. For example, the final temperature obtained for black oil at 1 km well depth is 171.1 °C while the final temperature shown in Figure. 2.11 is 174.2 °C, a reduction of 3.1 °C. The same is observed for the black oil-water mixtures. The 5% water cut is 170.2 °C while at isenthalpic conditions (Figure 2.11) this was 173.6 °C, a 3.4 °C reduction.

Figure 2.13 represents the results for a 3 km well depth. Comparing the results to 0km (Figure 2.11) and 1 km depth (Figure 2.12), it is quite clear that as the depth of the well decreases the increase in the final temperature decreases as well. The ΔZ term in Eq. (2) has an impact similar to heat loss. The temperature rise in the well is less up to 10 °C when compared with the isenthalpic case.

The behaviour of the final temperature observed at 1 km and 3 km depth compared to the isenthalpic conditions is confirmed by Figure 2.14 at 5 km depth.

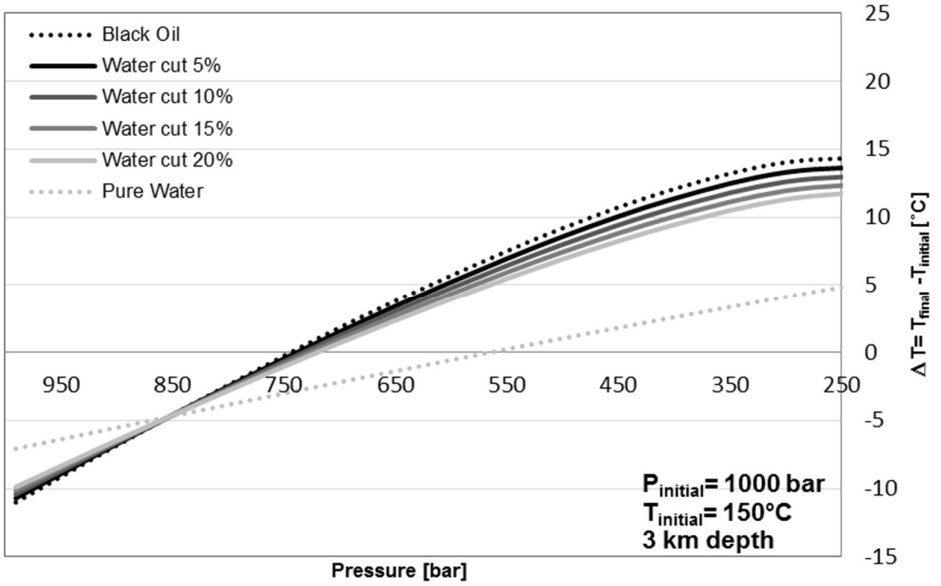

Figure 2.13 Decompression of black oil, pure liquid water and black oil-water mixtures at 1000 bar and 150 °C as initial conditions. Well depth 3 km. Non-isenthalpic process

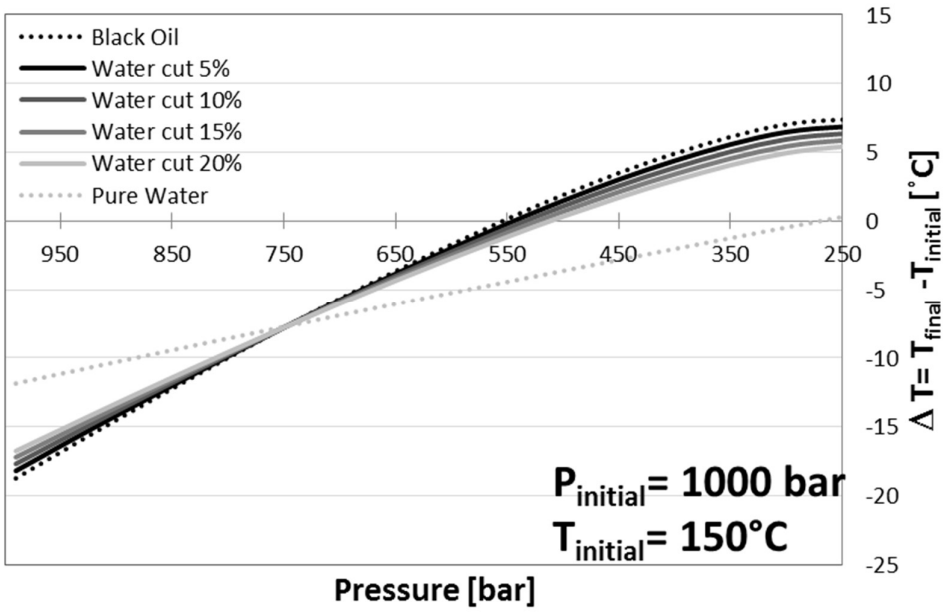

Figure 2.14 Decompression of black Oil, pure Liquid Water and black oil-water mixtures at 1000 bar and 150 °C as initial conditions. Well depth 5 km. Non-isenthalpic process

The lowest increase of the final temperature is observed in Figure 2.14 at a well depth up to 5 km. For instance, the increase for black oil at isenthalpic conditions (Figure 2.11) is 24.2 °C, equivalent condition in Figure 2.14 gives 7.4 °C. As stated by Ramberg [11] the change in potential energy "compensates for major part of the decompression" and as a consequence, the final temperatures are lower than those obtained at isenthalpic conditions. The findings in this study are in agreement with the observations made by Jones [17], Kortekaas et al., [18] and Baker and Price [9] who pointed out that increase in temperature is observed during decompression of oil from high pressure high temperatures as a consequence of the inverse JTE. The increase in temperature observed was 2 – 9 ˚C at a final pressure of 230 bar [17].

The results shown above reveal an evident dependence of the final temperature on the well depth. Even though the cases shown in Figure 2.12 and Figure 2.13 at 1 km and 3 km depth might be considered shallow reservoirs and might not exhibit HPHT conditions; the aim of showing these results is to highlight the importance of including the well depth into the energy balance. The case at 5 km well depth represents a more practical situation since typical depths of the HPHT reservoirs are in the order of this magnitude [31]. Therefore, the general approach used for estimation of the JTE in an oil reservoir is erroneous since the contribution of the potential energy is neglected. Here we have demonstrated the dependency of the final temperature on the well depth and further estimations of the JTE on HPHT should be based on this dependency.

The impact of brine

The results presented in the previous sections (see Section 2.5.1 and Section2.5.2) show an evident dependence of the final temperature on the well depth. Therefore, the results for heavy-oil brine are presented only for the non-isenthalpic scenario. Here the calculations are exemplified using the case of 6 molal brine with the heavy oil case. The findings are represented in Figure 2.15.

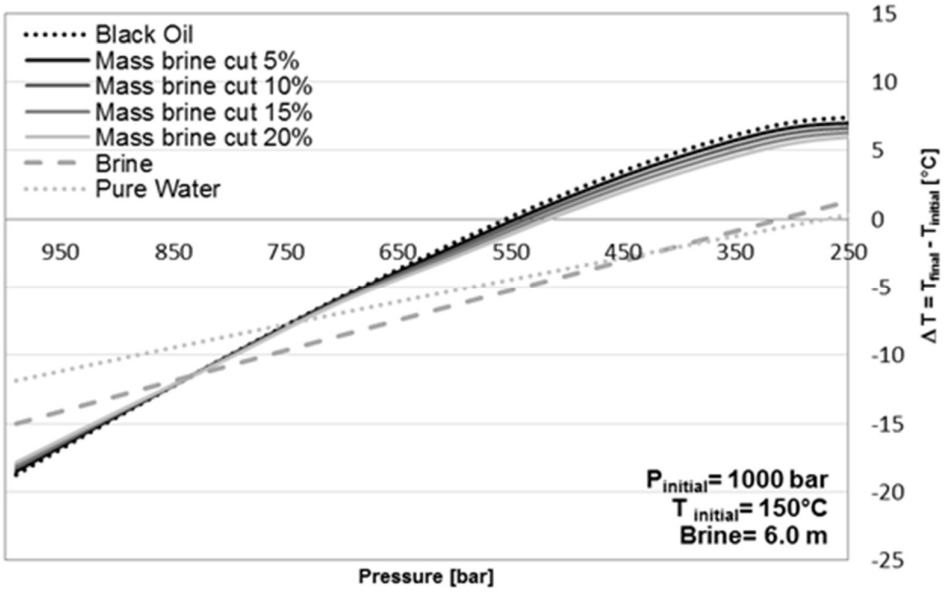

Figure 2.15 Decompression of black oil, pure liquid water, brine and black oil-brine mixtures at 1000 bar and 150 °C as initial conditions. Well depth 5km. Non-Isenthalpic process

Comparing the effect of pure water and brine, the brine causes a slight increase in the temperature. The final temperature of brine is 1.3 °C while pure water is 0.4 °C. It is therefore expected that brine will retain a higher temperature of the black-oil production compared to pure water. This is also visible by comparing Figure 2.14 and Figure 2.15.

An addition of a 5% water or brine cut increases the final temperature by 6.8 °C or 7.3 °C respectively. Therefore, the presence of NaCl in the oil-brine mixture produces an increase of 0.5 °C higher compared to the presence of pure water. At 20% cut the final temperature of pure oil is 155.7 °C and 156.2 °C for water and brine respectively.

2.6 Conclusions

The adiabatic decompression of pure liquid water does not occur at constant temperature, changes at the final temperature compared to the initial temperature are observed. An increase in the final temperature after an adiabatic decompression of liquid water at low initial temperatures (100- 200 °C) is observed in the case of initial pressure between 1500 and 1000 bars, at isenthalpic and non-isenthalpic conditions as a consequence of the inverse Joule-Thomson Effect. The inclusion of the terms for kinetic and potential energy into the energy balance of the process lower the effect over the

final temperature and in some cases, the overall effect is changed. That is observed for initial temperatures above 250 °C and initial pressure of 1500 bar, for which an overall heating effect is observed during decompression when the potential and kinetic energy are neglected. On the other hand, when those terms are included into the energy balance the overall conclusion changed, from an overall heating to an overall cooling upon decompression. These differences in temperature are associated with changes in potential and kinetic energy.

The behavior of pure liquid water after decompression is unexpected, since a decrease in the final temperature is expected after decompression of fluids as stated in the definition of the Joule Thomson Effect. This unusual behavior of liquid water as a consequence of the inverse Joule Thomson Effect might set off alarm bells for decompression processes of aqueous solutions or fluids with significant water content, since an anomalous heat flow might occur during the decompression.

Aqueous solutions of NaCl heat up upon decompression at non-isenthalpic conditions at high pressures and temperatures below 200 °C. The largest increase is observed at the lowest initial temperature studied here (100 °C). The temperature increase for a decompression from the initial conditions 100 °C and 1000 bars is 106.9 °C for saturated brine (6 mol of NaCl/kg of water). The presence of NaCl increases the Joule-Thomson Effect for an aqueous solution up to 4.6 °C in the case of saturated brine. Therefore, it can be concluded that the presence of NaCl in an aqueous solution at high pressure and temperatures below 200 °C will result in a larger increase in temperature than observed for pure liquid water.

An increase in the top site production temperature up to 24.2°C upon adiabatic decompression at isenthalpic conditions of black oil at 150 °C BHT and 1000 bar is calculated. The increase is the result of the inverse Joule-Thomson Effect (JTE) taking place during the adiabatic decompression of the oil. The effect of the well depth on the final temperature is explored. It was found that the terms for potential and kinetic energy reduce the temperature increase, which is a more realistic scenario. An increase of temperature up to 7.4 °C for black oil at non-isenthalpic (5 km well depth) conditions is obtained; this represents a 16.8 °C reduction compared to 24.2 °C increase at isenthalpic conditions.

The presence of brine and water in the black oil-water and black oil-brine mixtures lowers the heating effect. An addition of a mass brine cut of 5 % at 150 °C BHT, 1000 bar BHP and 5 km well depth, results in an increase of temperature up to 7.3 °C; while at the same conditions the increase of just black oil is 7.4 °C. Addition of water has a similar effect but the reduction is even less. A final temperature up to 156.8 °C is obtained when adding 5 % water cut to a black oil-water mixture. In

this case the reduction is 0.6 °C. Thus, addition of water or brine to oil has little effect on the final temperature upon decompression.

The methodology provided through this investigation demonstrates that prediction of the final temperature of oil-water and oil-brine mixtures when decompressed from HPHT reservoirs can be achieved using the correct energy balance of the process. The prediction of the final temperature will determine the operation conditions of the extraction process, the type of materials required and the capacity of evaporation of a reservoir.

Additionally, an accurate prediction of the final temperature will guarantee a safe operation of the reservoir.

References

[1] J.P. Joule, W. Thomson, On the Thermal Effects of Fluids in Motion. Part II, Philos. Trans. R. Soc. London. 144 (1854) 321–364. http://www.jstor.org/stable/108506.

[2] P.W. Atkins, J. de Paula, Atkins' physical chemistry, Oxford University Press, 2006.

[3] E. Albarran-Zavala, B.A. Espinoza-Elizarraraz, F. Angulo-Brown, Joule Inversion Temperatures for Some Simple Real Gases, Open Thermodyn. J. 3 (2009) 17–22.

[4] C.M. Oldenburg, Joule-Thomson cooling due to CO2 injection into natural gas reservoirs, Geol. Carbon Sequestration Methane Hydrates Res. from TOUGH Symp. 2006. 48 (2007) 1808–1815. doi:http://dx.doi.org.globalproxy.cvt.dk/10.1016/j.enconman.2007.01.010.

[5] K. O'Hara, Evaluation of asperity-scale temperature effects during seismic slip, J. Struct. Geol. 27 (2005) 1892–1898. doi:10.1016/j.jsg.2005.04.013.

[6] C.J. Adkins, Equilibrium Thermodynamics, (1983).

[7] B.Z. Maytal, A. Shavit, On the integral Joule-Thomson effect, Cryogenics (Guildf). 34 (1994) 19–23. doi:http://dx.doi.org.globalproxy.cvt.dk/10.1016/0011-2275(94)90047-7.

[8] M. Martin, G. Guiochon, Effects of high pressure in liquid chromatography, J. Chromatogr. A. 1090 (2005) 16–38. doi:http://dx.doi.org.globalproxy.cvt.dk/10.1016/j.chroma.2005.06.005.

[9] A.C. Baker, M. Price, Modelling the performance of high-pressure high-temperature wells, Pap. SPE. 20903 (1990) 21–24.

[10] C.R.B. Lister, On the thermal balance of a subduction zone, Geotherm. Asp. Low. Crustal Struct. Heat Flow Hydrothermal Circ. 257 (1996) 25–38. doi:http://dx.doi.org.globalproxy.cvt.dk/10.1016/0040-1951(95)00118-2.

[11] H. Ramberg, Temperature Changes Associated with Adiabatic Decompression in Geological Processes, Nature. 234 (1971) 539-. doi:10.1038/234539a0.

[12] I. Ahmad, O. Akimov, P. Bond, P. Cairns, T. Gregg, T. Heimes, G. Russell, F. Wiese, Drilling Operations in HP/HT Environment, Offshore Technol. Conf. (2014).

[13] J.K. Daniels, I.J. Littlehales, L. Lau, S. Linares-Samaniego, Laboratory Methods for Scale Inhibitor Selection for HP/HT Fields, Soc. Pet. Eng. (2014).

[14] W.A. England, Reservoir geochemistry - A reservoir engineering perspective, J. Pet. Sci. Eng.

58 (2007) 344–354.

[15] D. Bessieres, S.L. Randzio, M.M. Pineiro, T. Lafitte, J.L. Daridon, A combined pressure-controlled scanning calorimetry and Monte Carlo determination of the Joule-Thomson inversion curve. Application to methane, J. Phys. Chem. B. 110 (2006) 5659–5664. doi:10.1021/jp057038o.

[16] D.V. Nichita, C.F. Leibovici, Calculation of Joule-Thomson inversion curves for two-phase mixtures, Fluid Phase Equilib. 246 (2006) 167–176. doi:10.1016/j.fluid.2006.05.025.

[17] C. Jones, The Use of Bottomhole Temperature Variations in Production Testings, (1988). doi:http://dx.doi.org/10.2118/18381-MS.

[18] W.G. Kortekaas, C.J. Peters, J. de Swaan-Arons, High Pressure Behavior of Hydrocarbons. Joule-Thomson Expansion of Gas Condensates, Oil Gas Sci. Technol. 53 (1998) 259–263.

[19] A.R. Lang, PRESSURE AND TEMPERATURE GRADIENTS IN ASCENDING FLUIDS AND MAGMAS, NATURE-PHYSICAL Sci. 238 (1972).

[20] D.R. Waldbaum, Temperature Changes Associated with Adiabatic Decompression in Geological Processes, Nature. 232 (1971) 545-. doi:10.1038/232545a0.

[21] J. Vrabec, A. Kumar, H. Hasse, Joule-Thomson inversion curves of mixtures by molecular simulation in comparison to advanced equations of state: Natural gas as an example., Fluid Phase Equilib. 258 (2007) 34–40. doi:10.1016/j.fluid.2007.05.024.

[22] J.M. Smith, H.C. Van Ness, Introduction to chemical engineering thermodynamics, (1987).

[23] NIST/ASME, NIST/ASME Steam Properties Database 10: Version 3.0 Based upon the International Association for the Properties of Water and Steam (IAPWS) 1995 formulation, Version 3. (2013).

[24] D.G. Archer, Thermodynamic Properties of the NaCl+H2O System. II. Thermodynamic Properties of NaCl(aq), NaCl·2H2(cr), and Phase Equilibria, J. Phys. Chem. Ref. Data. 21 (1992) 793–829.

[25] D.-Y. Peng, D.B. Robinson, A new two-constant equation of state, Ind. Eng. Chem. Fundam. 15 (1976) 59–64.

[26] A. Danesh, D.H. Xu, A.C. Todd, Comparative-Study of Cubic Equations of State for Predicting Phase-Behaviour and Volumetric Properties of Injection Gas-Reservoir Oil Systems, Fluid

Phase Equilib. 63 (1991) 259–278.

[27] S.A. Wood, F.J. Spera, Adiabatic Decompression of Aqueous-Solutions - Applications to Hydrothermal Fluid Migration in the Crust, Geology. 12 (1984) 707–710.

[28] P.S.Z. Rogers, K.S. Pitzer, Volumetric properties of aqueous sodium chloride solutions, J. Phys. Chem. Ref. Data. 11 (1982) 15–81.

[29] H.C. Helgeson, D.H. Kirkham, Theoretical prediction of the thermodynamic behavior of aqueous electrolytes at high pressures and temperatures; I, Summary of the thermodynamic/electrostatic properties of the solvent, Am. J. Sci. 274 (1974) 1089–1198. doi:10.2475/ajs.274.10.1089.

[30] D. Smith-Magowan, R.H. Wood, Heat capacity of aqueous sodium chloride from 320 to 600K measured with a new flow calorimeter, J. Chem. Thermodyn. 13 (1981) 1047–1073.

[31] R. Maroli, M. Tambini, G. Wilde, S. Craig, Development of HP-HT Coiled Tubing Unit, (1996). doi:http://dx.doi.org/10.2118/35561-MS.

CHAPTER 3

Zinc Sulfide Scaling

3.1 Introduction

Zinc present in aqueous solution exist as the hexa-aquo $Zn(H_2O)_6^{2+}$ ion in which the coordination of zinc is octahedral. For the formation of zinc sulfide (ZnS) a series of units of ZnS is repeated with Zn and S in tetrahedral coordination, as a result amorphous ZnS (also known as sphalerite) is formed. Usually trace amounts of the metastable dimorph wurtzite is also formed and found in the ZnS structure [1].

The zinc sulfide scaling material is formed at oil reservoirs by the reaction between metal formation waters with hydrogen sulfide (H_2S)[2]. The presence of the metal could be also present in the rock formation [3]. Heavy fluids such as zinc bromide are used as a control mechanism for HP reservoirs. Any loss of the heavy fluid to the formation of the well will promote the formation of zinc sulfide scaling [4,5] . A case of zinc bromide loss was reported in the North Sea UK sector with subsequent formation of zinc sulfide on downhole gauges and logging tools [6].

The origins of the H_2S present in the HPHT reservoirs is produced from different sources [6–9]

- Bacterial: Reduction of sulfates present in the reservoir by sulfate-reducing bacteria.
- Thermal cracking: cracking of sulfur organic compounds.
- Thermo-chemical: chemical sulfate reduction.
- Decomposition of working fluids such as: drilling compounds and corrosion inhibitors

Zinc sulfide scaling has been identified near the wellbore and production tubing during fluid extraction, at the downhole safety valves (low pressure and low temperature conditions) in the Central Graben fields [2], at the surface choke at the Elgin/Franklin field [10], near the wellbore and

perforation interval in a well at the Gulf of Mexico as sphalerite [4] and wurtzite form [5], at the production tubing and in the topside (e.g. hydrocyclones) process facilities at North Sea oil and gas fields [6]

Potential risk of formation of zinc sulfide has been identified in the Glenelg Field as identifying the presence of H_2S (~300 ppm) and zinc in the cements of the reservoir rock and produced brines [8]

Zinc sulfide scaling presence is not only limited to oil reservoirs. This type of scale is also found in geothermal reservoirs together with other rich sulfide scaling materials (e.g. PbS and CuS) [11]. This inclusions have been observed in reservoirs in Iceland at the Reykjanes geothermal system [12] and at the Kakkonda geothermal field in Japan [11].

In order to understand the occurrence of ZnS as scaling material in HP/HT reservoirs, studies on the behavior of the solubility of ZnS are required. The influence of variables such as temperature and pressure of the reservoir are key aspects to be explored.

3.2 Previous studies on ZnS solubility

Several authors have studied and measured the solubility of ZnS in aqueous solutions at temperatures ranging from 18 °C to 350 °C. Generally, these solubility experiments were performed using different sources of Zinc Sulfide (ZnS). It is important to remember that ZnS exists in two crystalline forms: Sphalerite and Wurtzite. Sphalerite is the cubic crystal form of ZnS and it is thermodynamically stable at standard conditions while wurtzite (hexagonal crystal form) is thermodynamically stable at temperatures above 1035 °C [13]. These crystalline forms, present different solubility values.

In the study by Barrett and Anderson [14] precipitated ZnS was used, obtained by bubbling H_2S through a solution of $ZnCl_2$. No further analysis to confirm the crystal structure of the solid was carried out. By this in-situ precipitation of ZnS, different types of solids with different properties can be produced. The solubility of ZnS precipitated from alkaline medium (identified by Barrett and Anderson [14] as β ZnS) is about 4.6 times higher than the solubility of ZnS precipitated from acidic medium (identified by Barrett and Anderson[14] as α ZnS).

Tagirov and Seward [15] indicated that their solubility measurements were slightly higher for the precipitated solid form than the solubility of the natural occurring sphalerite as a consequence of the presence of another crystalline form of ZnS: Wurtzite. They assumed that wurtzite was present in

such small quantities but the XRD analysis did not detect it. They compared their measured solubility values of natural and of precipitated sphalerite and concluded that the solubility of natural sphalerite is lower than that of the precipitated form. Their hypothesis was that the difference in solubility was due to the presence of fine particles or another form of ZnS.

The analytical techniques and the experimental procedures documented in literature for measuring the solubility of ZnS are widely diverse, which is a contributing factor for the observed scatter in the published data. The zinc content was analyzed using atomic absorption spectroscopy [14,16–19]

The solubility of mineral (from Santander mine) and in-situ precipitated ZnS was measured by [20]. The author did not use degassed water, which could lead to the formation of oxidized sulfate species. These oxidized species give a higher zinc concentration. Thus, the measured value is a combination of the ZnS solubility and the solubility of the oxidized sulfate species. Furthermore, the solubility was measured using conductivity as analytical technique. Conductivity is not a zinc selective technique as contaminants and other ions in the solution also contribute to the measured conductivity value. The measured conductivity values include the impurities present in either the aqueous solution or dissolved from the mineral/precipitated form of ZnS. Moreover, the use of both mineral and precipitated ZnS was employed by Weigel [20]. Differences were observed for the solubility measurements when using mineral ZnS and precipitated ZnS. The author noticed that the solubility of mineral ZnS is lower than that of precipitated ZnS [20].

The gravimetric technique was employed by Ellis, Laudise and Hemley [21–23]. The solubility of ZnS was determined in water at temperatures between 200 and 300 ˚C (no clear information about the experimental pressure is given) [21]. Oxygen was removed from the water by stripping with pure nitrogen. The solute was light brown colored mineral ZnS. The solubility was determined by a gravimetric method removing crystals from the vessel and then weighed in a micro-balance after each run. The solubility data presented by Ellis [21] show no significant temperature dependency between 194 ˚C and 300 ˚C. It is suggested that the value determined corresponds to the solubility of zinc oxide (ZnO) [21]. A possible explanation for this unexpected tendency may be the presence of impurities in the type of solute used by Ellis [21]. Thus, the value of solubility reported may correspond to the solubility of other species rather than ZnS, e.g. ZnO [21]. The gravimetric method applied by Ellis [21] is questionable as well, since it is not the most suitable for this type of experiments due to its low accuracy for sparingly soluble materials [21]. The precision of the method was questioned by Laudise [22] who also implemented this method for the determination of ZnS

solubility. It was claimed by Ellis [21] that 20 mg of the solid were dissolved in 20 cm^3 of water, in the vessel. There is no information about the accuracy of the measurements nor the sensitivity of the scale used.

A colorimetric measurement technique was implemented by Vukotic [24]. The solubility of ZnS was measured in water at temperatures from 110 ˚C up to 350 ˚C. The measurements were carried out at the corresponding water vapor pressure at each temperature. The ZnS was prepared in-situ using a solution of zinc acetate and H_2S (purity 99.2%). The solubility measurements were carried out in an autoclave using degassed water. The zinc present in the aqueous solution was analyzed by means of colorimetry using dithizone. The solubility data published by Vukotic [24] show a slight dependency on temperature. There is no information regarding the pore size of the filter plug installed in the experimental set-up. Potentially in this case, the data reported as ZnS solubility could contribute to the concentration of suspended fine particles in the apparently saturated solution.

The solubility of radioactive ZnS was measured in a bomb at 130±5 ˚C at pressures between 275-345 bar by Relly [25]. The solubility was determined using the Zn65 as a tracer and measuring the gamma-radiation intensity with a scintillation detector. It is mentioned that different zones at different temperatures were detected in the bomb. The sensitivity of the tracer method was questioned by the author, suggesting the radiation of the sample was weak and therefore the data point obtained is doubtful [25].

The solubility of ZnS in aqueous solution measured using the polarography technique was employed in [26]. He reported solubility values in pure water at 25 °C and 100 °C at 6.8 and 34 bar respectively. An increase of ZnS solubility is observed as temperature and pressure increase. However, in this case the individual influence of temperature or pressure cannot be discussed [26].

The majority of the analytical methods here mentioned do not have very low detection limits and therefore the accuracy of the solubility determination is questionable. Thus, both the purity of the sample and the experimental method needs to be carefully selected to assure reliability and precision of the experimental data.

3.3 Experimental set-up

The experimental set-up designed for measuring the solubility of sparingly soluble salts such as ZnS is shown in Figure 3.1. The system consists of 3 key parts: (1) an equilibrium cell (Figure 3.1b),

transport of sample at constant temperature (Figure 3.1d) and filtration at constant temperature (Figure 3.1e).

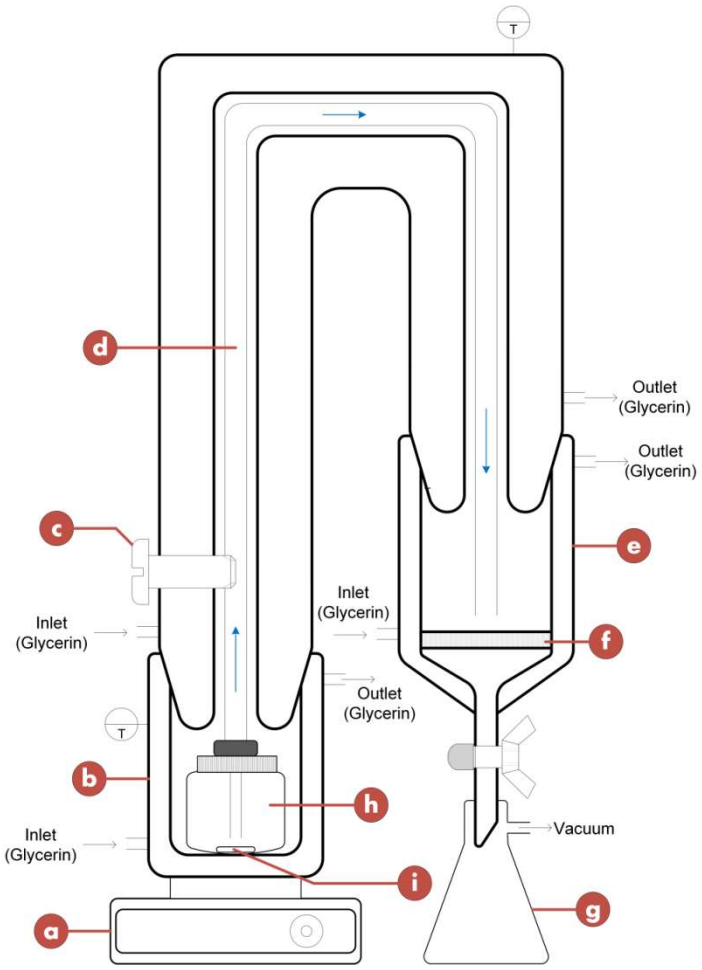

Figure 3.1 Experimental set-up for measurements of ZnS. (a) Stirring plate, (b) equilibration cell, (c) Teflon screw, (d) transport of sample at constant temperature, (e) filter chamber, (f) porous body, (g) side-arm flask, (h) vial and (i) stirring bar

The set-up runs at constant temperature by means of a thermostatic bath using glycerin as heat-transfer fluid. The filter chamber (Figure 3.1e) is a double walled chamber that contains a porous body (Figure 3.1f) made of fritted glass of porosity (10-16 μm).

3.3.1 Materials description

The experiments were performed using ZnS powder of 99.99% purity (from Sigma-Aldrich) and with a particle size of 10 μm. The characteristics of this solid were analyzed using state-of-the-art analytical techniques. The particle size distribution of the ZnS powder was verified by means of laser

diffraction analysis. The ZnS crystal structure was confirmed by means of X-Ray Diffraction (XRD) and its elemental composition was determined using a Scanning Electron Microscope (SEM).

3.3.2 Purity of the ZnS material used

A series of non-destructive analysis were performed to confirm the crystalline structure and stoichiometry of the ZnS. The X-ray analysis was carried out at DTU Chemistry and the SEM analysis at Center for Electron Nanoscopy. The results obtained for the X-ray analysis are presented in Figure 3.2.

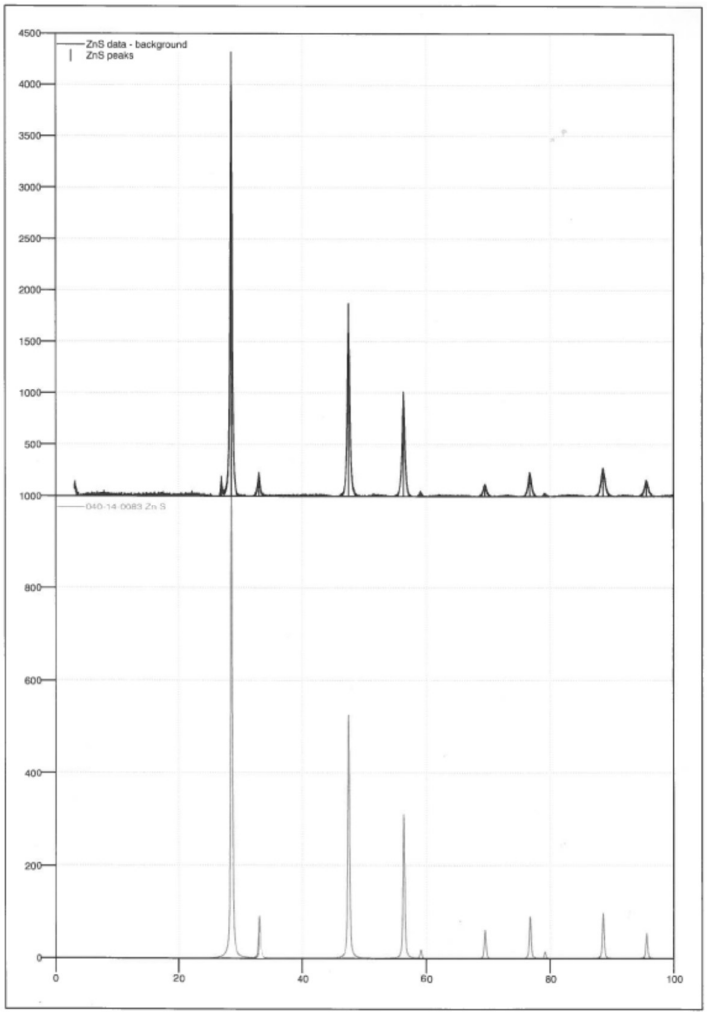

Figure 3.2 X-ray analysis for ZnS.

The peaks observed for the analyzed material (Figure 3.2 upper spectrum) are located at the same scattering angle 2θ (axis of abscissas) than the reference pattern (Figure 3.2 bottom spectrum). The solid is identified as pure ZnS in its cubic form.

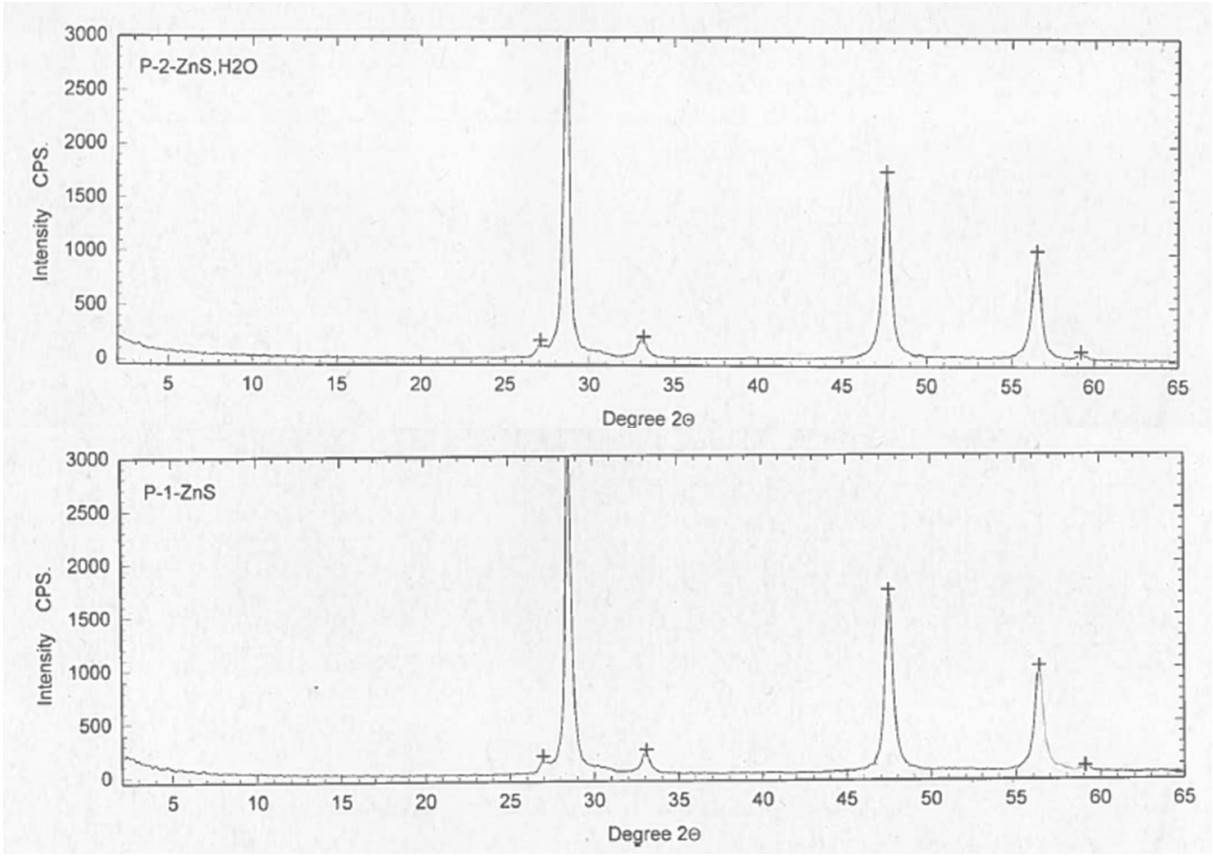

Figure 3.3 X-ray analysis. The upper graph represents the spectra for ZnS after processing. The graph at the bottom corresponds to the spectra of the starting material.

Figure 3.3 shows the X-ray analysis of the ZnS solid left after solubility measurements. The upper plot corresponds to the spectrum of ZnS solid in excess in the aqueous solution. The bottom part is the starting material ZnS (powder). The spectra do not show any significant difference between them. The X-ray analysis shows that the ZnS crystals do not undergo any changes after days of being under experimental conditions.

The elemental composition was carried out using SEM analysis and the results are shown in Figure 3.4 and Table 3.1. The results confirm the presence of zinc and sulfur as major components. The impurities present in the ZnS can be considered negligible. The presence of these impurities is also doubtful since the majority of peaks overlap Zn and S.

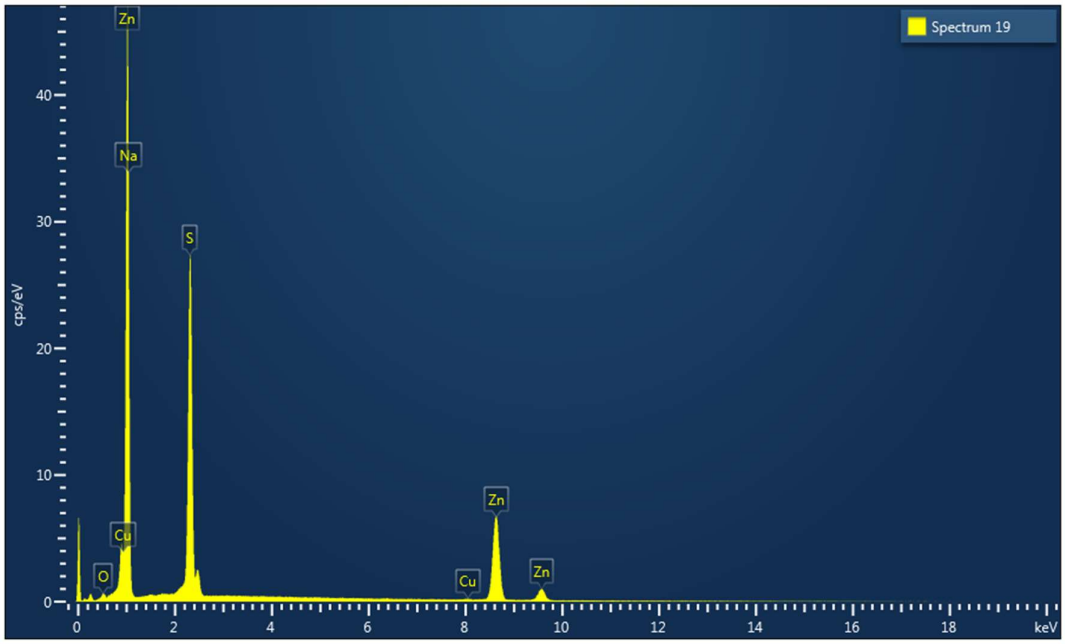

Figure 3.4 Scanning Electron Microscopy spectrum for ZnS.

The elemental analysis demonstrates that the composition corresponds to ZnS and the impurities do not have a significant effect on the solubility measurements of ZnS.

Table 3.1 Elemental analysis for ZnS material used using SEM

	Elements (Weight %)				
Statistics	**Zn**	**S**	**O**	**Na**	**Cu**
Max	62.57	30.95	2.03	9.47	1.90
Min	60.57	26.54	1.20	3.55	1.52
Average	61.58	28.42	1.54	6.74	1.72
Standard Deviation	0.99	1.98	0.40	2.67	0.15

The number of areas analyzed during the SEM analysis was 4. The standard deviation obtained for these measurements is considered low and acceptable with respect to the average value obtained. Thus, no extra measurements were carried out to determine the composition of ZnS. The intention using the SEM was to confirm the presence of Zn and S as major components, rather than providing the exact quantitative composition of ZnS.

There is evidence for the existence of non-stoichiometric ZnS [27] but based on the results shown above it can be said that the sample of ZnS corresponds to stoichiometric ZnS. Therefore, no

deficiencies of Zn or S can be attributed to the difference in concentration of the Zn and S observed during the solubility measurements (see Figure 3.10)

The aqueous samples were prepared using ultra-pure water (resistivity ~18.2 MΩ) degassed with nitrogen (purity 99.999%) [28]. The concentration of dissolved oxygen was monitored using an oxygen electrode. The oxygen removal process was stopped when the oxygen level was less than 0.01 mg/L (lowest detection level of the electrode). The ZnS in solid form was equilibrated with degassed ultra-pure water at reduced oxygen atmosphere in a glove box using nitrogen (purity 99.999%). This is an important step as ZnS is susceptible to oxidation in presence of oxygen [23,29]. Oxidation of the sample leads to formation of ZnO.

3.4 Methodology

This section describes the methodology developed for solubility measurements of salts with very low solubility in water, such as ZnS, PbS and FeS. This methodology is demonstrated for ZnS and it addresses many of the uncertainties of previous experiments: evaporation of unknown amounts of water at high temperatures, identity of the crystalline form of the investigated sample, the filter pore size and the particle size, the purity of the sample, impact of oxygen and other impurities.

In this study, the determination of ZnS solubility was carried out at temperatures up to 80°C and atmospheric pressure. In all the experiments, the surface of the sample was covered with a layer of insoluble silicon oil to minimize evaporation, similar to the work of [30]. Solubility measurements at 96 ˚C were performed but the evaporation of the aqueous phase was significant.

Afterwards, the sample was placed in a polypropylene vial (see Figure 3.1h) instead of a glass vial, to reduce the risk of contamination with interfering ions in the aqueous solution. Then, silicon oil was added to the aqueous solution to avoid vapor formation of the solution and evaporation of H_2S from the solution [30]. The vial was immersed in the equilibrium cell (Figure 3.1b) filled with glycerin and connected to a thermostatic bath until equilibrium is attained. The sample is stirred continuously using a stirring plate (Figure 3.1a). The vial (Figure 3.1h) is connected to the sampling hose (Figure 3.1d) and sealed using a Teflon screw (Figure 3.1c) to avoid the presence of oxygen in the sample. Stirring was stopped approximately 3 hours before sampling to allow ZnS particles to settle down.

After solid-liquid equilibrium was attained, the suspension was filtered at constant temperature in the filtration chamber (Figure 3.1e). The filter is custom made with a heating jacket using a temperature

equal to the equilibration temperature. This guarantees no alteration of the equilibration conditions of the solution. A filter paper with a pore size of 0.22 μm was used. This is a key feature of the developed experimental set-up which maintains success of the sampling.

After filtration, the solution is diluted immediately with ultra-pure water (Figure 3.1g). The dilution of the sample takes place in the side-arm flask with a previously weighed amount of ultra-pure water. This dilution is carried out to avoid precipitation of the solid phase from the saturated solution. The dilution takes place at room temperature.

Afterwards, a set of samples were withdrawn from the diluted solution and the concentration of zinc and total sulfur was determined by Inductively Coupled Plasma Optical Emission Spectroscopy (ICP-OES).

The excess solid was collected from the vial (see Figure 3.1h), dried in a vacuum oven (at 105°C) and the crystal structure was analyzed by XRD.

3.4.1 Inductively Coupled Plasma Optical Emission Spectroscopy (ICP-OES)

The ICP-OES is an analytic technique that is commonly used for trace elemental analysis. It is based on the formation of analyte ions formed in the inductively coupled plasma and then sent to an optical spectrometer where the identification of the analytes takes place. The ICP torch is an assembly of three fused-silica tubes. Argon flows throughout these silica tubes which then will constitute the plasma. In the ICP torch a spark from a Tesla coil is used to produce “seed” electrons and ions that are transported by the argon flow. The solution is then introduced by means of converting the solution in an aerosol. Then the sample is conducted by the inner argon (Ar) flow into the central channel of the plasma. The temperature in the plasma is around 9726°C (10000 K) in which the aerosol is rapidly vaporized. Afterwards the aerosol is desolvated and then the analytes are broken into free atoms (ionized) by the plasma. The collisions in the plasma promote the atoms to excited states. Now in the form of ions the analytes are detected in a photodetector. The characteristic wavelength of the photons produced in the plasma is converted to an electrical signal by the photodetector. Then the identification and concentration of the analytes can be determined based on the characteristic wavelength and the total number of photons [31,32]. A schematic diagram of an ICP-OES is illustrated in Figure 3.5.

Sampaio et al. (2009) measured the concentration of Zn in aqueous solutions to monitor the concentration of zinc in effluent. In their work ICP-OES analytical technique was implemented to

trace the remaining concentration of zinc of an effluent after reaction with NaS to precipitate ZnS and eliminate zinc from the effluent.

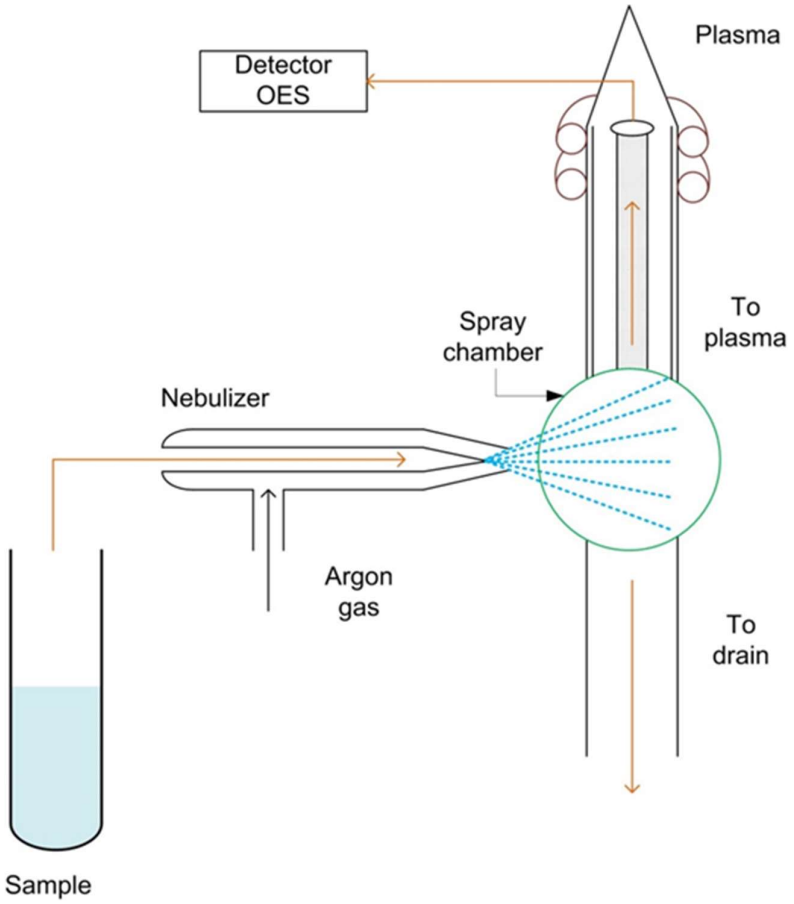

Figure 3.5 Schematic diagram of an ICP-OES assembly

The acidification of the samples for ICP-OES could be questioned if the HNO_3 is considered to interfere with sample. Tagirov et al. used a matrix of 0.5% HNO_3 and 1.5%HCl. They tested the impact of the matrix on the concentration of zinc for the measurements in the FAA (Flame Atomic absorption). The test performed consisted of a set of standard solution with a known concentration of zinc. The concentrations were measured using the matrix mentioned above. Tagirov et al. found out that there is no significant change in the zinc concentration. A set of samples were tested in this study and no impact of the addition of HNO_3 was observed on the ICP-OES results [19].

3.5 Results and discussion

The results of the experimental determination of ZnS solubility are presented in two sections: First the equilibration time results are presented as concentration of zinc and total sulfur versus time. Then, the solubility of ZnS at different temperatures ranging from 40°C up to 80°C is presented.

3.5.1 Dependency on initial mass

In order to study the presence of fine particles in an indirect way, the initial mass of ZnS powder added to the plastic vial was varied. Then the samples were analyzed as described in the methodology section. The concentration of zinc was measured using the ICP-OES analytical technique and the results are shown in Figure 3.6. If there are fine particles present in the saturated liquid, these fine particles will be accounted for zinc concentration, since ICP-OES is not specific for analyzing ions; instead the detection of the element is carried out.

The pore size of the filter membrane (0.45 µm) was initially chosen based on the particle size provided by Sigma-Aldrich (10 µm)

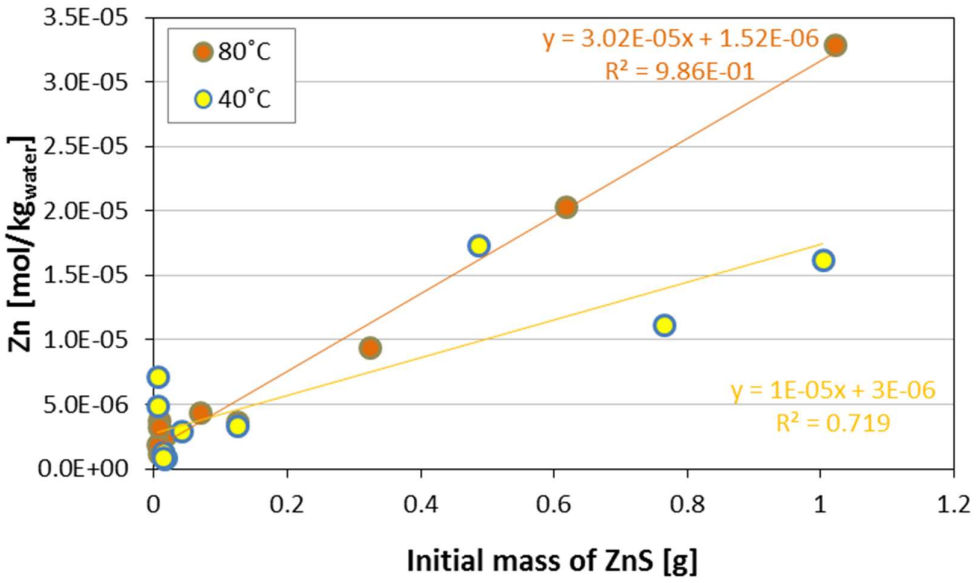

Figure 3.6 Dependency on the ZnS initial mass on the concentration

Figure 3.6 shows clearly a dependency of the solubility of zinc on the initial mass of ZnS. This indicates that there are fine particles that are not retained by the porous membrane and are present in the aqueous phase. The presence of fine particles does not allow to determine if the aqueous phase is

saturated and if it has reached equilibrium conditions. Instead a much higher solubility value will be reported.

The data obtained that include the concentration of the fine particles are shown in Figure 3.7. It can be observed that the data are in between the limits of the literature data published until now. The dependency of the solubility on temperature shows a very flat profile compared to the data obtained in Figure 3.11. Furthermore, the data obtained are comparable to those reported at high pressures. This suggests elevated values for the solubility values obtained. Additionally the information regarding the type and size of pore size used for filtration of samples (if carried out) is not clear as it is the case of the experiments performed by Vukotic [24]. Some of the published data mentioned in Section 3.2 are not included in Figure 3.7 as they were obtained at experimental conditions relatively different to the ones considered in this work.

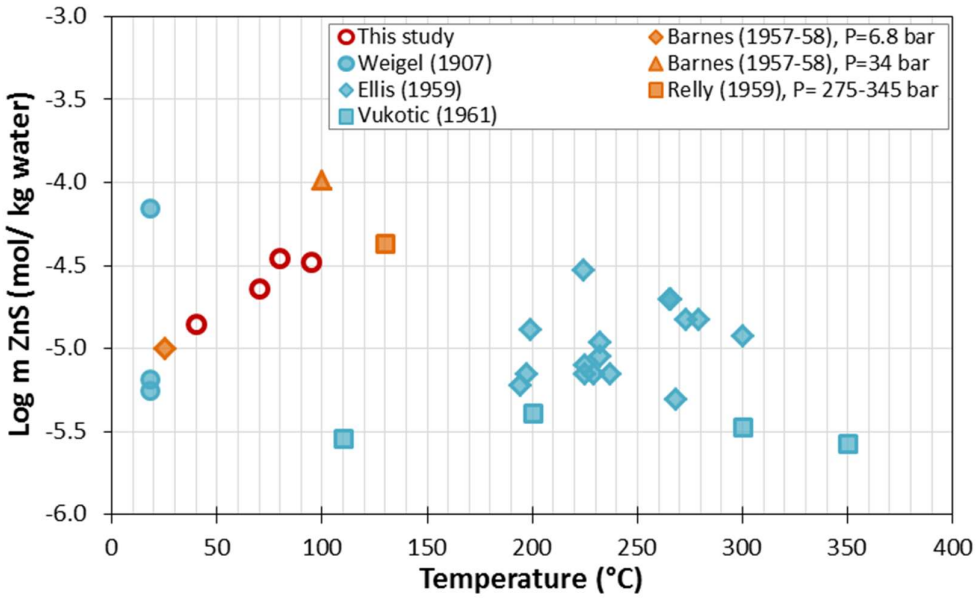

Figure 3.7 Preliminary data obtained for the solubility of ZnS. The high values reported here are due to presence of fine particles in the aqueous phase.

The problem of the fine particles was initially addressed by a new design of the jacketed filter. The first filter employed in the experiments was a single-body filter. It was observed that the liquid sample could by-pass the filter membrane between the walls of the glass body and the edges of the membrane.

Then the new design of the jacketed filter consisted of a two-bodies: 1. a glass funnel (Figure 3.8a) and a base with a porous body (Figure 3.8c). The membrane can be easily placed between the two parts and secured with an aluminum ring (Figure 3.8b).

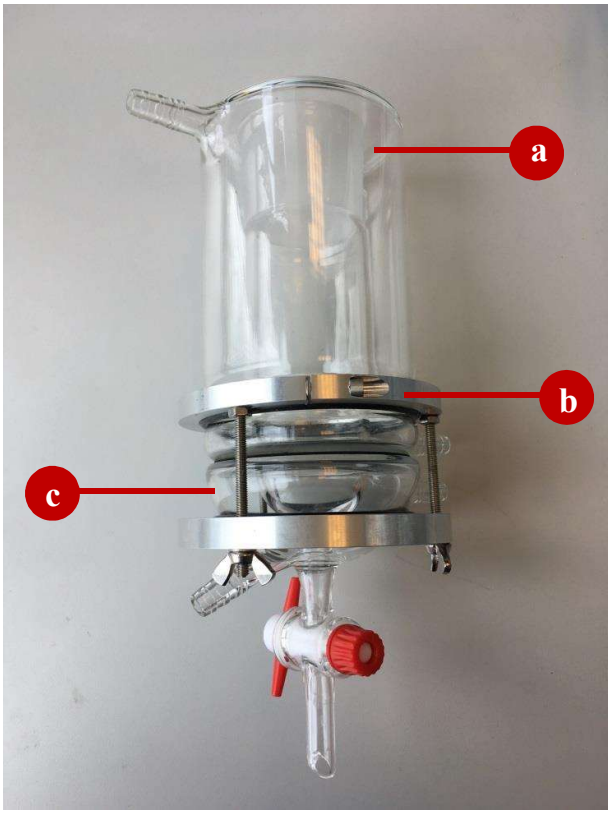

Figure 3.8 Jacketed filter

Additionally, the filter membrane pore size was chosen with respect to a particle size analysis distribution (see Section 3.5.2). A reduction of 93% in the concentration of zinc was observed when using the filter illustrated in Figure 3.8 and a membrane of 0.22 µm of pore size.

3.5.2 Particle size distribution of the ZnS source material

The distribution of the ZnS source material particle size used in this work was determined in two different ways: 1. in powder (dry) and 2. in an aqueous dispersed form (dispersion). This was carried out in order to determine the correct pore size for the filtration step. This particle size distribution analysis was performed using the laser diffraction method [34]. The results are presented in Figure 3.9 as the volume density (%) versus the particle size (logarithmic scale).

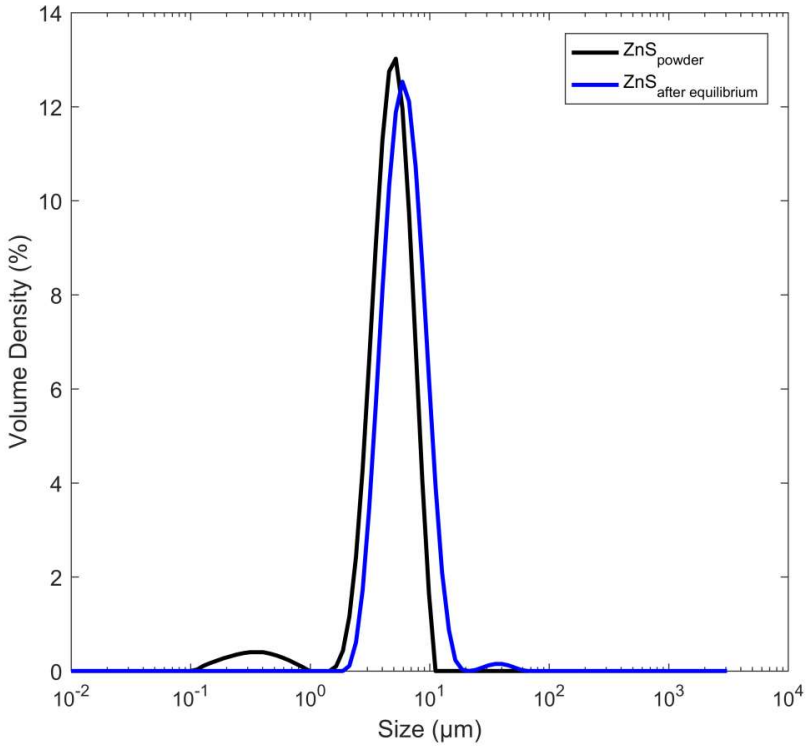

Figure 3.9 Particle size distribution for ZnS

Figure 3.9 shows that the ZnS powder used in the experiments has a particle size distribution between 0.11 to 9.86 μm. The majority of the particles (13.02%) have a particle size of 5.21 μm. The vast majority of the particles are smaller than 10 μm as specified by the supplier. For the powder, 98.87% of the particles have a particle size greater than the selected filter pore size (0.22μm). A more useful scenario is the measurement of the particle size of ZnS dispersed in the saturated solution. This analysis provides the particle size distribution of the sample before filtration. In this case the particle size is distributed between 2.13 μm (0.11%) and 58.9 μm (0.02%) with a maximum at 12.53% that corresponds to a particle size of 5.92 μm. These findings are in agreement with the result for the powder. Figure 3.9 shows that the majority of the particles are smaller than 10 μm and 99.99% of the particles have a particle size above 0.22 μm (filter paper pore size). Thus, the particle size analysis confirmed that the majority of the particles are larger than the pore size of the used filter paper.

The particle size distribution analysis provided valuable information for choosing the correct filter pore size for filtration. If the filter pore size is chosen arbitrarily, the chance of fine particles passing through the filter is very high. Then, the determination of the ZnS solubility would be erroneous as

the concentration of Zn and S would include the fine particles suspended in the “saturated solution” as mentioned by [15].

3.5.3 Equilibration time determination

This section discusses the importance of equilibration time when determining the solubility of ZnS at temperatures up to 80 ˚C. The equilibration time represents the time needed to reach equilibrium between the solid and the liquid phases and it varies with respect to temperature and the source of ZnS. Therefore, the experimental analysis of equilibration time is very important to assure experimental reproducibility and accuracy.

There is no agreement regarding the equilibration times for ZnS solubility suggested in the literature. It was indicated by [18] in their experiments that the solubilization period is greater than 48 hours. They did not provide any reason why they decided on using this equilibration time. The equilibration time was estimated based on the pH of the solutions by [14,16]. They estimated that equilibrium is attained in hours (in saline solutions), based on the time required for the solution to reach a constant value of pH. They mentioned that the equilibration time depends on the starting material. They found that the equilibration time is achieved faster when using precipitated material than when using the mineral forms [14,16].

The experiments performed by Ellis [21] were run up to 150 hours (roughly 6 days). Ellis did not explore the results at extended times. His results indicate that equilibrium was not reached and therefore no influence of temperature was observed [21]. Hemley [23]estimated that the equilibration time was between few days (at high temperatures) and up to 2 weeks (at low temperatures) for his experiments of ZnS and PbS at 300 to 500 ˚C and 1000 bars. Meanwhile, Relly observed that equilibrium was attained at at around 50 to 60 hours [25].

Figure 3.10 shows the concentration of zinc and the concentration of total sulfur as a function of time for temperatures between 40 ˚C and 80 ˚C. It is assumed that all zinc is present as zinc ion (Zn^{2+}). Figure 3.10c shows that the concentration of zinc increases during the first 3 days. Then it reaches a plateau corresponding to equilibrium. Figure 3.10a and Figure 3.10b show that the concentration of zinc slightly fluctuates with respect to time. However, the concentration of total sulfur remains constant along the time interval studied. The scattering observed in the data could be due to presence of colloidal particles present in the filtrate that passed through the filter paper. The presence of colloidal particles might contribute to the solubility values of ZnS

The equilibration time is observed to vary depending on temperature and it is apparently shorter at higher temperatures. It can be observed from Figure 3.10 and Table 3.2 that the equilibration time in this interval of temperature (40 ˚C to 80 ˚C) required is minimum 3 days.

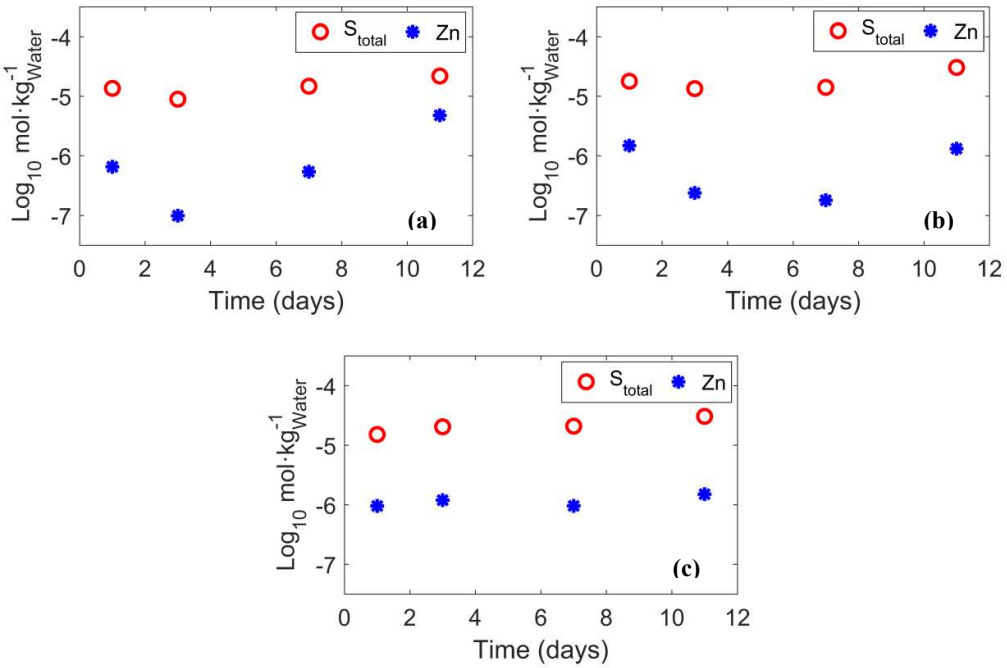

Figure 3.10 Determination of the equilibration time for ZnS solubility measurements at temperatures (a) 40 ˚C (atmospheric pressure), (b) 60 ˚C (atmospheric pressure) and (c) 80 ˚C (atmospheric pressure).

The results described above are based on the behavior of the zinc concentration. The concentration of total sulfur remains almost constant over the intervals of time analyzed; suggesting that the equilibration time is achieved in a matter of hours. Figure 3.10 shows that up to 10 days, the concentration of total sulfur is in some cases hundreds of times higher than the concentration of zinc. This difference between zinc and total sulfur concentration reduces over time at 40 ˚C and 11 days when the concentration or total sulfur is just five times higher than the concentration of zinc. This behavior is not observed at higher temperatures analyzed (60 ˚C – 80 ˚C).

Table 3.2 Solubility data for ZnS at temperatures between 40 ˚C and 80 ˚C at atmospheric pressure. Equilibration times between 1 and 11 days. The concentration corresponds to the average of the data points reported.

Eq. time (days)	Temp. (˚C)	Zn concentration [mol·kg^{-1} H_2O] x 10^8	Data points	S total concentration [mol·kg^{-1} H_2O] x 10^6	Data points
1	40	65.27 ± 18.8	4	13.54 ± 0.1	4
	60	148.03 ± 1.5	3	17.84 ± 0.2	3
	80	95.36 ± 48.1	3	15.09 ± 0.1	5
3	40	9.91 ± 0.6	4	8.91 ± 0.7	5
	60	23.91 ± 2.9	4	13.40 ± 0.1	4
	80	119.52 ± 16.3	3	20.30 ± 9.7	3
7	40	54.14 ± 17.3	6	14.71 ± 0.7	3
	60	18.00 ± 0.9	3	14.09 ± 0.7	4
	80	95.66 ± 4.2	4	20.81 ± 1.2	3
11	40	477.00 ± 147.4	4	21.82 ± 1.2	4
	60	131.26 ± 68.9	4	14.09 ± 0.7	4
	80	150.52 ± 0.8	3	30.40 ± 12.9	3

This difference between the concentration of zinc and total sulfur could be due to the presence of byproducts in the ZnS or formation of other products during the solubilization process. It was mentioned by [33] that a soluble species $Zn(HS)_n$ could be present in the aqueous solution. They also observed an excess of total sulfur even though sulfur was added in stoichiometric quantities [33]. The formation of complexes has been discussed by several authors; nonetheless the existence of those complexes cannot be easily proved [1,15,18,19]. It was found by Luther et al. [1] in their studies on the formation of sphalerite at low temperature (25°C) in saline solutions (0.545 mol·L^{-1} NaCl) and neutral pH (controlled by adding 5 mmol·L^{-1} of acetate) a complex with stoichiometry of 3 S and 2 Zn. They claimed the presence of molecular clusters of ZnS in solution [1].

It can be concluded that the time required to reach equilibrium conditions is minimum 3 days at temperatures above 40 ˚C. The exact time cannot be set as it is very hard to identify a clear trend of the Zinc concentration versus time as demonstrated in Figure 3.10.

3.5.4 Effect of temperature on ZnS solubility

Figure 3.11 shows the effect of temperature on the solubility of ZnS at temperatures between 40 ˚C - 400 ˚C and varying pressures. The ZnS solubility data of this work reported in Figure 3.11 corresponds to the concentration of zinc and 3 days of equilibration at atmospheric pressure. The solubility data are presented in Table 3.2.

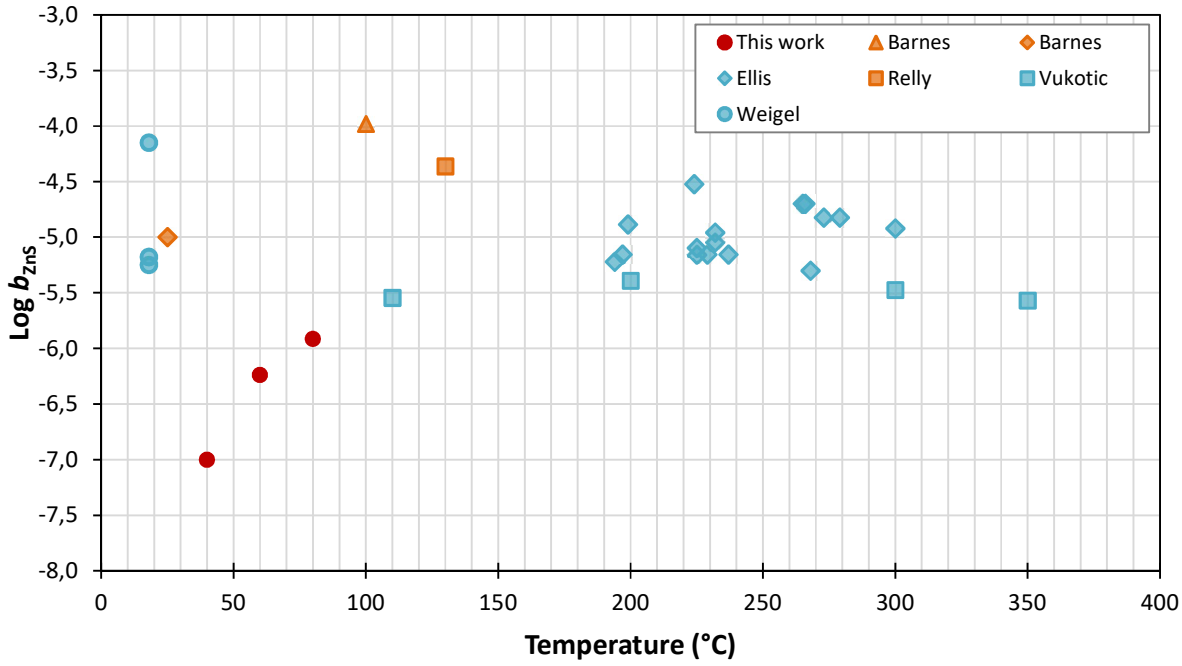

Figure 3.11 Solubility of ZnS vs temperature. Barnes [26] at 6.8 bar (diamond marker) and at 34 bar (triangle marker); Ellis [21]; Relly [25] at 275-345 bar (pressure range is presented since it is not certain the value at which the experiments were run); Vukotic [24] and Weigel [20]

Figure 3.11 indicates that the solubility of ZnS exponentially increases with temperature between 40 ˚C and 80 ˚C. An increase of 40 ˚C results in an increase of roughly 12 times for the solubility of ZnS.

Figure 3.11 also shows published ZnS solubility by Weigel, Ellis, Vukotic, Barnes and Relly [20,21,24–26]. The pressure conditions of the studies by Weigel and Ellis [20,21] at which the solubility data were obtained are not specified. The pressure conditions for Vukotic's experiments correspond to the water vapor pressure at each temperature [24]. This diagram shows that our measured ZnS solubility at 40 and 60 ˚C are 10 - 100 times lower than previously published data. The reason for this is discussed below.

The solubility data presented by Ellis [21] show no significant temperature dependency between 194 ˚C and 300 ˚C as observed in Figure 3.11. A possible explanation for this unexpected tendency may be the presence of impurities in the type of solute used by Ellis [21] or the presence of oxygen in the bomb that lead to formation of ZnO as suggested by Ellis [21].

The solubility data published by Vukotic [24] in Figure 3.11 show a slight dependency on temperature. An increase in solubility is observed from 110 ˚C until 200 ˚C, reaching at this point a maximum. Beyond 200 ˚C the solubility of ZnS tends to decrease.

An increase of ZnS solubility is observed (see Figure 3.11) as temperature and pressure increase for the solubility data published by Barnes [26]. However, in this case the individual influence of temperature or pressure cannot be discussed, since both parameters were modified during the experiments.

The ZnS solubility data presented by different authors in Figure 3.11 are highly scattered. The discrepancies and low reproducibility of the data observed between authors originate from various factors: (1) The starting material is different in all the cases. Some authors studied the solubility of ZnS using mineral ZnS from different origins [20]. Others performed the experiments with precipitated ZnS [14,15]. In some cases the precipitate was obtained in-situ using different purification methods [24]. (2) It is questionable if equilibrium was reached. (3) The presence of oxygen also plays an important role in the measured value. There was no attempt of removing oxygen in some of the experiments; therefore oxidized species could have been formed and partially affect the measured solubility [20]. (4) The withdrawal of saturated solution in some cases does not occur at constant conditions (e.g. constant temperature). A particle size analysis was not carried out and used for selecting the pore size of the filter [24]. (5) Finally, the analytical techniques may not have been the most accurate for the determination of sparingly soluble salts e.g. gravimetric determination of the solubility implemented by Ellis [21] and the sensitivity of the radioactive tracer used by Relly [25]. Some of the applied analytical techniques might also include the concentration of contaminants present in the solution [20].

3.5.5 Reliability of the analytical technique

The reliability of the developed methodology for measurement of ZnS is assured by addressing the pitfalls observed in previous experimental methodologies. In this work there was a detailed focus toward the accuracy of the analytical technique applied for the concentrations measurements in water. The background noise of contaminants such as Zinc present in the ultra-pure water was measured.

Blank samples (i.e. ultra-pure water) were analyzed by ICP-OES showing that the concentration of Zinc and total Sulfur was below the detection limit ($4x10^{-8}$ mol·kg^{-1} for Zinc and $2x10^{-7}$ mol·kg^{-1} for total Sulfur). Therefore, the content of total zinc and sulfur in the matrix of the samples does not constitute a source of noise in the measurements.

The error estimation of the measurements is determined using standard solutions of the elements studied here. The relative error estimated for zinc concentrations oscillates between 0.7 and 10.1%. For total sulfur the error estimation oscillates between 0.6% and 5.7%.

3.6 Conclusions

The solubility of ZnS in aqueous solution was determined at temperatures between 40 ˚C – 80 ˚C (atmospheric pressure). A dependency of the ZnS solubility on temperature was observed in the interval of temperature studied. An increase of 40 ˚C results in an increase of roughly 12 times for the solubility of ZnS.

An experimental set-up was developed to measure the solubility of Zinc Sulfide (ZnS). This setup can be used for determination of low soluble salts solubility up to approximately 100 ˚C at atmospheric conditions for systems which tend to react with oxygen. The set-up and the developed methodology presented in this work address several drawbacks and pitfalls to be aware of during the analysis. These play a vital role in the previously published ZnS solubility measurements reported in literature.

The developed methodology prevents oxidation of the starting material and assures equilibrium conditions even during filtration of the saturated solution.

The purity of the starting material was determined by SEM analysis, showing that the composition of the solid sample corresponds to high purity ZnS. A particle size analysis of the ZnS starting material was performed. This analysis is a key step during the determination of the ZnS solubility, allowing to choose the correct pore size for the filtration step. Equilibrium conditions were guaranteed by exploring a wide range of equilibration times (between 1 and 11 days). It is concluded that ZnS reaches equilibrium at around 3 days in contact by water. The scattering of the experimental data reported in this study could be due to presence of colloidal particles in the filtrate.

ICP-OES was applied as analytical technique. The relative error estimated for the measurements varies from 0.6% to 10.1%, showing that ICP-OES is an adequate analytical technique for

determination of ZnS solubility. The standard deviation calculated for each run demonstrates the very good precision of the implemented methodology.

References

[1] G.W. Luther, S.M. Theberge, D.T. Rickard, Evidence for aqueous clusters as intermediates during zinc sulfide formation, Geochim. Cosmochim. Acta. 63 (1999) 3159–3169. doi:10.1016/S0016-7037(99)00243-4.

[2] S. Baraka-lokmane, C. Hurtevent, H. Zhou, P. Saha, N. Tots, F. Rieu, TOTAL ' s Experience on the Development and Implementation of a Scale Management Strategy in Central Graben Fields, (2014) 1–17.

[3] C. Okocha, K.S. Sorbie, C. Hurtevent, S. Baraka-Lokmane, M. Rossiter, Sulphide Scale (PbS/ZnS) Formation and Inhibition Tests for a Gas Condensate Field with Severe Scaling Conditions, SPE Int. Oilf. Scale Conf. Exhib. (2014). doi:10.2118/169798-MS.

[4] J.G. Darby, D.A. Uhlig, J.R. Steckler, J. Martin, Scale Prevention Application of a Chemical Technology That Has Been Effectively and Economically Applied to a 420° F, 13,500-Ft-Deep, Gulf of Mexico (GOM) Well to Prevent Lead and Zinc Sulfide Deposition, in: SPE Annu. Tech. Conf. Exhib., Society of Petroleum Engineers, 2009.

[5] S.L. Berry, J.L. Boles, A.K. Singh, I. Hashim, Enhancing Production by Removing Zinc Sulfide Scale From an Offshore Well: A Case History, Soc. Pet. Eng. (2011).

[6] M.M. Jordan, K. Sjursaether, M.C. Edgerton, R. Bruce, Inhibition of Lead and Zinc Sulphide Scale Deposits Formed during Production from High Temperature Oil and Condensate Reservoirs., in: SPE Asia Pacific Oil Gas Conf. Exhib., Society of Petroleum Engineers, 2000.

[7] A.J. Savin, B. Adamson, J.J. Wylde, J.R. Kerr, C.W. Kayser, T. Trallenkamp, D. Fischer, C. Okocha, Sulfide Scale Control: A High Efficacy Breakthrough Using an Innovative Class of Polymeric Inhibitors, SPE Int. Oilf. Scale Conf. Exhib. (2014). doi:10.2118/169777-MS.

[8] C. Okocha, K. Sorbie, Scale Prediction for Iron, Zinc and Lead Sulphides and Its Relation to Scale Test Design, Corros. 2014. (2014) Paper No 3766. doi:10.2118/164111-MS.

[9] S. Baraka-Lokmane, C. Hurtevent, H. Zhou, P. Saha, N. Tots, F. Rieu, TOTAL ' s Experience on the Development and Implementation of a Scale Management Strategy in Central Graben Fields, Soc. Pet. Eng. (2014) 1–17. doi:10.2118/169757-MS.

[10] G.M. Graham, C.S.A. MacPherson, C. Simpson, K. Orski, S.M. Heath, Development of Appropriate Test Methodologies for the Selection and Application of Lead and Zinc Sulphide

Inhibitors for the Elgin/Franklin Fields, Soc. Pet. Eng. (2006).

[11] N. Yanagisawa, K. Fujimoto, Y. Hishi, Sulfide scaling of deep-geothermal well at Kakkonda geothermal field in Japan, in: Proc. World Geotherm. Congr., 2000: pp. 1969–1974.

[12] V. Hardardóttir, M. Hannington, J. Hedenquist, Metal concentrations and metal deposition in deep geothermal wells at the Reykjanes high-temperature Area, Iceland, Procedia Earth Planet. Sci. 7 (2013) 338–341.

[13] H.L. Clever, M.E. Derrick, S.A. Johnson, The solubility of some sparingly soluble salts of zinc and cadmium in water and in aqueous electrolyte solutions, J. Phys. Chem. Ref. Data. 21 (1992) 941–1004.

[14] T.J. Barrett, G.M. Anderson, The solubility of sphalerite and galena in 1–5 m NaCl solutions to 300 C, Geochim. Cosmochim. Acta. 52 (1988) 813–820.

[15] B.R. Tagirov, T.M. Seward, Hydrosul fi de / sul fi de complexes of zinc to 250 ° C and the thermodynamic properties of sphalerite, Chem. Geol. 269 (2010) 301–311. doi:10.1016/j.chemgeo.2009.10.005.

[16] T.J. Barrett, G.M. Anderson, The solubility of sphalerite and galena in NaCl brines, Econ. Geol. 77 (1982) 1923–1933.

[17] A.H. Ewald, G.. Hladky, Solubility Measurements on Sphalerite, North Ryde (NSW), Australia, 1980.

[18] K. Hayashi, A. Sugaki, Solubility of sphalerite in aqueous sulfide solutions at temperatures between 25 and 240 ° C, 54 (1990) 3–5.

[19] B.R. Tagirov, O.M. Suleimenov, T.M. Seward, Zinc complexation in aqueous sulfide solutions: Determination of the stoichiometry and stability of complexes via ZnS(cr) solubility measurements at 100 °C and 150 bars, Geochim. Cosmochim. Acta. 71 (2007) 4942–4953. doi:10.1016/j.gca.2007.08.012.

[20] O. Weigel, The solubility of the sulphides of the heavy metals in water, Z. Phys. Chem. 58 (1907) 293–300.

[21] A.J. Ellis, The solubility of zinc sulfide in water at high temperatures, Econ. Geol. 54 (1959) 1035–1039.

[22] R.A. Laudise, E.D. Kolb, D. JP, Hydrothermal solubility and growth of sphalerite, Am.

Mineral. 50 (1965) 382.

[23] J.J. Hemley, C. Meyer, C.J. Hodgson, A.B. Thatcher, Sulfide solubilities in alteration-controlled systems, Science (80-.). 158 (1967) 1580–1582.

[24] S. Vukotic, Contribution to the study of the solubility of galena, of sphalerite, and of chalcopyrite in water in the presence of hydrogen sulfide between 50 and 200 C, Bull. Bur. Rech. Geol. Min. (1961) 11–27.

[25] B.H. Relly, A method for determining solubility at high temperatures and pressures, Econ. Geol. 54 (1959) 1496–1505.

[26] H.. Barnes, Ore Solutions, 57th ed., Carnegie Institute of Washington, 1958.

[27] S.D.B.H.. Scott, Sphalerite-wurtzite equilibria and stoichiometry, Geochim. Cosmochim. Acta. 86 (1972) 1275–1295.

[28] C. Okocha, Effects of Sulphide Scales (PbS , ZnS & FeS) on BaSO4 Crystal Growth and Dissolution, Water. 96 (2010). doi:10.2118/130391-MS.

[29] I.M. Kolthoff, The Solubilities and Solubility Products of Metallic Sulphides in Water, J. Phys. Chem. 35 (1931) 2711–2721.

[30] R.W. Potter, M.A. Clynne, Solubility of highly soluble salts in aqueous media. Part 1. NaCl, KCl, CaCl2, Na2SO4, and K2SO4 solubilities to 100°C, J. Res. US Geol. Surv.;(United States). 6 (1978).

[31] X. Hou, B.T. Jones, Inductively Coupled Plasma / Optical Emission Spectrometry, (2000) 9468–9485.

[32] J.W. Olesik, ICP-OES and ICP / MS, 63 (2000) 12–21.

[33] R.M.M. Sampaio, K.J. Keesman, P.N.L. Lens, Monitoring ZnS Precipitation: Estimation, Error Analysis and Experiment Design, 2009. doi:10.1080/01496390902886013.

[34] R. Jones, Particle size analysis by laser diffraction: ISO 13320, Am. Lab. 35 (2003).

CHAPTER 4

Iron and Lead Sulfide Scaling

4.1 Introduction

Iron present in aqueous solution exist as the hexa-aquo $Fe(H_2O)_6^{2+}$ ion in which the coordination of iron is octahedral. Iron sulfide is present in several crystalline forms as mackinawite $FeS_{(1-x)}$, troilite FeS, pyrrhotite $Fe_{(1-x)}S$ (monosulfides: only stable in absence of oxygen) pyrite FeS_2 (cubic) and marcasite FeS_2 (orthorhombic) (iron disulfides) [11].

Iron sulfide scaling can be formed as a consequence of corrosion in the well as well as deposition as a result of the reaction of soluble Fe and H_2S present in the well. Iron sulfide scaling is usually present in H_2S rich oil wells (sour oil) and gas wells [1–4] . Iron sulfide is not only present in oil reservoirs, it is also found in water reservoirs [5–7].

Formation of FeS has been reported at the Khuff gas reservoir in Saudi Arabia. The gas produced by this reservoir is a sour gas rich in H_2S and CO_2 and a heavy condensate. The deposited material is porous, with a light brown to black color and it has been usually located at the bottom half of the tubing string. The composition of the material was identified as mainly iron, sulfur and chlorine. In the case of FeS the composition analysis shows that the material is iron deficient pyrrhotite [$Fe_{(1-x)}S$ where x varies from 0 to 0.14] but mackinawite (Fe_9S_8) and pyrite (FeS_2) were also found along together with other corrosion related compounds. It was found out that the scaling material near the pipe is mainly iron and chlorine while the outer layer (next to flow streams) is mainly composed by iron and sulfur [1].

Iron sulfide scale can cause problems during wire-line work, reduce well deliverability and loss of injectivity in power water injectors, water supply wells and gas wells [1,2]. Iron sulfide is not only present in the well, it is found upstream as well in heat exchangers and furnaces reducing their

efficiency [2]. Meanwhile, lead sulfide scaling has been located typically near the wellbore, production tubing, surface choke (90 °C)and at the downhole safety valves(at 125 °C) [8,9].

4.2 Previous studies on Iron Sulfide solubility

The solubility of mackinawite $FeS_{(1-x)}$, troilite FeS, pyrrhotite $Fe_{(1-x)}S$ (monoclinic and hexagonal), and pyrite FeS_2 was determined by Tewari *et al.* [10]. The solubility experiments were carried out in aqueous solutions at 0.1 MPa and 1.8 MPa H_2S pressures between 25 °C and 125 °C. The starting material was single crystals of FeS obtained from the Mines Branch Ottawa. Tewari et al. [10] decided to use single crystals in order to minimize the contribution of fine particles to solubility values and to avoid the presence of impurities present on the surface of powder materials. Mackinawite and hexagonal pyrrohotite were precipitated in situ since they were not available. The solid was equilibrated with triple distilled water (Fe concentration less than $5x10^{-8}$ m). Solubility data of troilite and pyrrhotite were not analyzed at temperatures above 125 °C to avoid conversion to higher sulfide phases. The solubility experiments were carried out in a titanium autoclave. The samples were withdrawn at constant temperature and pressure. The pore size of the filter installed in the sampling line was 0.02 μm. The iron concentration was determined by atomic absorption spectroscopy (AAS) and by colorimetry. The precision of the AAS method was determined as ±12% in the concentration range below 1 μg/g. The precision of the colorimetric method was determined as ±5% for concentrations above 1 μg/g. Equilibrium conditions in the case of troilite were achieved within hours while pyrrhotite (monoclinic) required at least seven days. For pyrrhotite (hexagonal) the equilibration time was determined as 100 hours. The fast dissolution of mackinawite and its transformation to other sulfides types made the determination of its solubility very difficult. It is believed that due to those reasons the equilibration time could not be determined accurately. Equilibration time for pyrite is not specified. It is concluded that mackinawite is the most soluble form while pyrite is the least soluble one. The solubility ratio at 25 °C and 1.8 MPa H_2S were determined as 6000:80:40:10:1 for mackinawite, troilite, monoclinic pyrrhotite, hexagonal pyrrhotite and pyrite respectively. It is observed that solubility of all iron sulfide forms decreases with temperature increase. The highest impact of temperature is observed for mackinawite which show the most drastic decrease in solubility in the temperature range between 25 °C and 125 °C. Tewari et al. [10] also observed changes in the structure of mackinawite after the dissolution experiments. They

observed the presence of other types of FeS such as marcasite, greigite (Fe_3S_4) and pyrite in runs at ambient temperature [10].

Rickard [11] describes the solubility measurements of in-situ precipitated FeS. The FeS was precipitated in situ using Mohr's salt ($Fe(NH_4)_2(SO_4)_2 \cdot 6H_2O$) as a source for Fe^{2+}. The Mohr's salt was chosen since previous experience of the author evidenced oxidation using other sources of Fe^{2+} (i.e. $Fe(ClO_4)_2$). The Mohr's salt was added to a solution of 0.1 M NaCl. The system was purged with oxygen-free nitrogen and HCl (10%) was added until the pH was below 3. Afterwards H_2S was bubbled through the solution for 45 minutes. Addition of 4 M NaOH was carried out to induce the precipitation of FeS. Measurements were performed at different pH by controlling the addition of NaOH. The equilibration time was determined as the time required to reach a constant pH. The equilibration time in these experiments varied from 2 to 6 hours and it depended on the concentration of the H_2S gas. The solution was sampled (temperature variation during extraction was not mentioned) and it was filtrated in a 0.45 μm filter (no particle size analysis was presented). Rickard [11] claims that the filtrated solution was crystal clear with no solid particles present. The solution was filtrated (using a 0.02 μm filter) finding no evidence of nanoparticles present. The stability of the aqueous solution at equilibrium was carried out by repeatedly freezing and thawing the solution. No changes in the solution were observed. Rickard [11] mentioned that the concentration of H_2S in the aqueous phase varied due to changes in the atmospheric pressure. This introduced a source of error to the measurements of solubility. Rickard [11] found that the solubility of FeS is independent of pH at neutral and alkaline pH, while at acidic pH there was a clear dependency. The FeS precipitated was analyzed and identified as a modified mackinawite structure. The author concludes that the solubility results obtained cannot be compared to other studies since the composition of the FeS precipitated is in doubt. Rickard [11] also pointed out that there is a lack of information regarding the structure of the FeS and the method how it was precipitated by different authors. FeS obtained from acid solutions tends to be more stable and therefore less soluble than FeS obtained at basic pH.

Berner [12] studied the solubility product of FeS at 25±0.1 °C. For his measurements Berner [12] used 4 crystalline forms of FeS (greigite, mackinawite, precipitated FeS and pyrrhotite). All the four crystal forms were synthesized in the laboratory. Precipitated FeS was obtained by bubbling H_2S into a $FeSO_4 \cdot 7H_2O$ aqueous solution. The dissolved of H_2S was eliminated by evaporation. Then the product was filtered using a 0.45 μm membrane and the solid obtained analyzed by X-Ray diffraction in order to observe changes in the crystal structure during solubility analysis. Evaporation of H_2S and

the pore size of the membrane can introduce error to the measurements. Evaporation of H_2S could lead to a change in the equilibrium conditions and consequently measuring the concentration of iron of a solution that was not at equilibrium. The large pore size employed in this study will increase the likelihood of fine particles to be present in the liquid phase (as discussed previously for other studies). Pyrrhotite of almost stoichiometric composition ($Fe_{0.8}S$) was obtained by the reaction between elemental iron and sulfur at high temperatures and vacuum conditions. The particles obtained were in the order of millimeters size. The particles were grinded (no particle size provided by the author) prior to solubility analysis and stabilized in aqueous solution previously saturated with H_2S. The dissolved iron was determined by using a DU spectrophotometer (measures the UV and visible spectra). The change in pH was explored to determine equilibrium conditions. Experiments typically lasted between 3 to 6 hours. The criterion employed was less than 0.01 pH units change in 3 hours [12].

Solubility data of FeS at high pressure and/or high temperatures are scares in open literature. Yan et al. [13] studied the solubility of troilite at HPHT reservoir conditions (100 °C – 250 °C and 336.6 bar – 1654.7 bar). The measurements were carried out in a flow-through apparatus in 1M and 3M NaCl solutions at anoxic conditions. The concentration of iron was measured by ICP-OES. A phase change was observed after the analysis of the solid, finding by XRD that the solid was a mixture of troilite and pyrrhotite. The author mentions that this is caused by the cooling and heating sequence of the experiments. It is observed that the solubility of iron increases as the pressure increases. Meanwhile the effect of temperature on the iron concentration is inverse. The presence of NaCl in the solution increases the solubility but the effect is not as large as observed for pressure.

4.3 Previous studies on Lead Sulfide solubility

Lead sulfide is formed after the reaction of lead present in the formation waters or from external sources such as decomposition of inhibitors. Lead sulfide scaling has been located typically near the wellbore, production tubing and at the downhole safety valves [8]. Lead sulfide scaling is not only limited to oil reservoirs, it is also present in geothermal fields. As an example, PbS was found as the predominant scale mineral in the Salton Sea California geothermal field. This well is characterized by the presence of heavy metals in its brine composition such as Zn, Cu, Pb and Fe [14].

Lead sulfide is also known as Galena and it is characterized by a cubic crystal structure. An orthorhombic form of lead sulfide has been identified but it only exists at high pressures (25000 bar) [15]

Weigel [16] measured the solubility of both precipitated and crystallized PbS mineral. The solubility of the former is higher than the one of the later. The analytical technique chosen by Weigel was conductivity. The conductivity technique is not adequate, as the conductivity levels of these solutions are very low. The solubility data reported by Weigel using conductivity are likely to be the conductivity of impurities present in the water or in the solid PbS itself. Another hypothesis is that the data may correspond to measurements of oxidized species, which may occur in the oxygen rich solution water (no attempt of oxygen removal was made by the author) [16].

Nims and Bonner [17]estimated the solubility of PbS by means of concentration cells in which the electromotive force (e.m.f) was measured. One of the cells contained galena obtained from a mine and it was washed with ammonium acetate to remove oxide products from the surface. The equilibration time was assumed to be attained when the e.m.f. between the cells was constant. There are not enough arguments regarding the experimental procedure to consider that the value reported is doubtful. On the other hand, the algebraic approximations made in order to calculate the e.m.f in presence of different anions can impact the final result [17].

Hamann and Anderson [18] experienced low reproducibility of the measurements of the solubility of galena. The measurements of PbS were conducted in sulfur-rich NaCl solutions. They explored the solubility at two temperatures: 25 °C and 90 °C. The large deviations observed in their data are due to several reasons: (1) Fine particles getting through their filter, was believed to be a large source of error. They used a series of filters, with a pore size of 4 μm as the smallest. The study did not provide a particle size distribution. This analysis would have provided valuable information on whether the filter pore size would retain fine particles or not; (2) They also experienced precipitation of colloidal sulfur, when acidifying samples. This could alter the equilibrium conditions and therefore influence the solubility data; (3) Moreover, the data are presented with a rather broad range in pH and equilibration time. The measurements were conducted at pH values between 3 – 12 and equilibration times between 20 and 204 hours. There are no samples tested at similar conditions, therefore comparison between experiments is almost impossible. The pH of the solutions in acidic ($pH<8$) and moderately alkaline ($8<pH<11$) solution was controlled by bubbling H_2S and/or adding NaOH and. The strongly alkaline solutions ($pH>11$) were prepared by adding of $Na_2 S{\cdot}9H_2O$. This naturally will

make the pH level fluctuate, and rather hard to reproduce accurately. They had no comments on whether equilibrium conditions were reached, other than assuming that the elapsed time was enough to have saturated solutions. These different conditions at which the experiments were conducted give ambiguous solubility data. Furthermore, the results show large standard deviations, confirming the poor experimental conditions mentioned above and the low sensitivity of the analytical method. A lead concentration of 25±130 ppb reported at 90 °C is a good example of the enormous standard deviation. Many of the solubility data are negative values; which indicate that the detection limits of the atomic absorption spectrophotometer (AAS) were not suitable for their experiments [18].

The experimental work of Barrett and Anderson [19] consists of a detailed description of the experimental procedure employed for solubility measurements of galena. They used a precipitated form of PbS obtained by bubbling of H_2S through a $PbCl_2$ solution. The solubility data reported were obtained at a salinity range from 3 m to 5 m of NaCl. This study shows larger solubility values in the same temperature and salinity range than the values reported by Hamann and Anderson [18]. The pH conditions are lower (0.5-2.97) than in the before mentioned study of Hamann and Anderson [18] (pH 3 - 12). They controlled the pH values by adding NaOH or HCl. The analytical method used for solubility determination in their study was AAS. Equilibration time was determined by the change in pH values of the solution. Equilibrium conditions were achieved in a matter of few hours. The variation of pH in this type of solutions is very low and could incur in an inaccurate determination of the equilibration time. The pore size of the filtration media employed in this study was between 0.2 and 0.45 μm. Comparing the results obtained in this study by Barrett and Anderson [19] against the results obtained by Hamann and Anderson [18] a large decrease is observed in the concentration values of PbS which could be attributed to the reduction in pore size by Barrett and Anderson [19] compared to a 4 μm pore size employed by Hamann and Anderson [18] (the comparison is valid since both studied used ASS as analytical technique). Another pitfall noted in Barrett and Anderson [19] experimental procedure is the change in temperature during the filtration step. This decrease in temperature can interfere the equilibrium conditions and might trigger precipitation.

The effect of temperature and pH on the solubility of PbS was studied by Gallup [14] in hypersaline brines (4.3 m NaCl). The experiments were carried out in an autoclave at temperatures up to 300 °C. Oxygen was removed from the autoclave using pre-purified nitrogen. pH was adjusted to desired values (4.0 to 5.5) with HCl. The pH was not monitored during the experiments neither measured after sampling. PbS was precipitated from the reaction between $PbCl_2$ and H_2S (0.0006m). The sampling process is not explained in detail, but it can be implied that the sample was withdrawn at

experimental conditions and then filtered using a 0.22 μm membrane. No information is provided regarding the time lapse between the precipitation of PbS and the moment the aliquot was taken. Lead concentration was measured by ICP technique but there is no information available about the detector (MS or EOS). Gallup adverts that the solubility data obtained in his study are elevated compared to PbS solubility in water due to chloride complexing [14].

4.4 Experimental set-up

The experimental set up used for FeS and PbS solubility determination was described in Chapter 3. No modifications were done for the set-up during the experiments using FeS and PbS.

4.4.1 Materials description

The starting material for measuring the solubility of FeS and PbS was a precipitated form of FeS and PbS provided by Sigma-Aldrich. The purity of the material is 99.9% trace metals basis. The sulfides provided by Sigma Aldrich are not packed in anoxic containers. Oxygen may cause oxidation on the surface of the particles. The FeS and PbS crystal structure and presence of oxidized species present in the initial solid were determined by X-Ray Diffraction (XRD). A particle size analysis of the starting material was run to determine accurately the required pore size of the filtration membrane.

4.4.2 Purity of the FeS and PbS used

X-Ray Diffraction (XRD) analysis was performed for FeS and PbS to identify their crystal structure. The XRD patterns are shown in Figure 4.1.

(a)

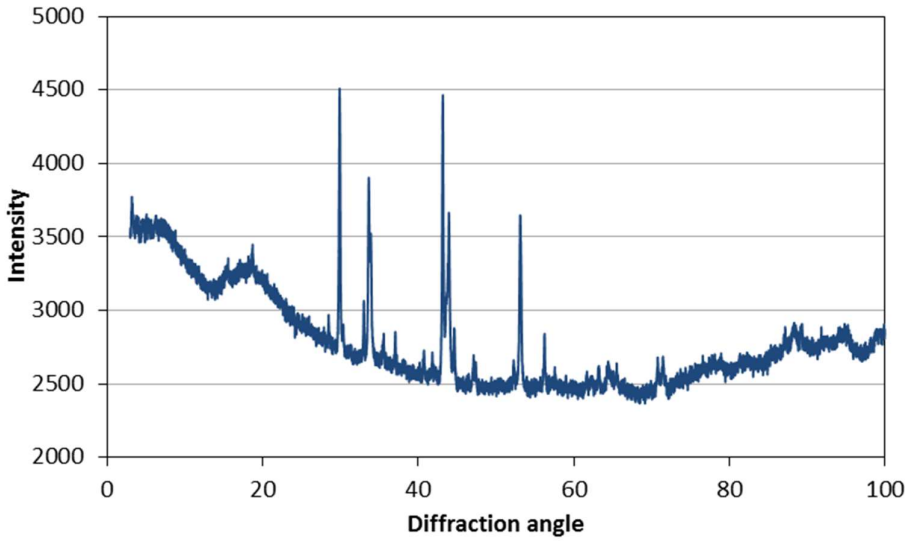

(b)

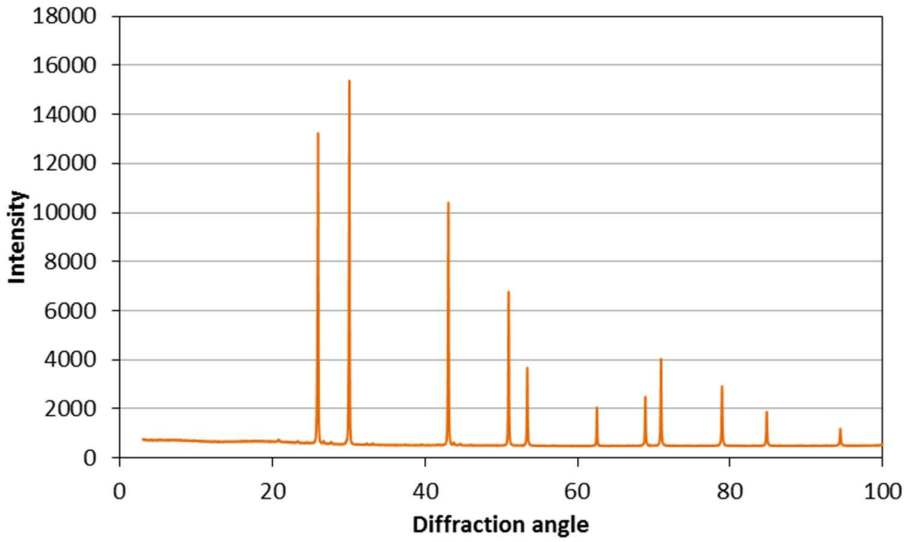

Figure 4.1 X-ray diffraction patterns of (a) Iron sulfide and (b) Lead Sulfide

The spectrum for FeS (Figure 4.1a) identifies the starting material solid as FeS with less than stoichiometric Fe. The compound is identified as synthetic pyrrhotite in its hexagonal form. The XRD analysis suggests a formula of $Fe_{0.98}S$ or $Fe_{0.879}S$. The XRD analysis is a qualitative analysis and therefore the pattern just proposes that the FeS starting material is pyrrhotite, containing slightly less iron than sulfide.

Figure 4.1b shows the XRD pattern obtained for PbS. The pattern is more clearly defined than the one obtained for FeS and the material was identified as synthetic Galena (PbS) in its cubic form. No other compounds were found in the solid analyzed.

No other compounds different than FeS and PbS were detected by XRD. Therefore, the solubility measurements are carried out with the intended initial solid. No peaks referring to oxidized species were found in the XRD. Although increasing the time analysis of the samples might show some oxidized species (due to XRD analysis carried out in oxygen rich atmosphere). A rigorous procedure is followed to avoid the oxidation of the FeS starting material. The procedure is explained in Section 4.5.

4.5 Methodology

The methodology developed to determine the solubility sulfides is described in detail in Figueroa et al. [20]. The solubility of FeS and PbS was measured at temperatures ranging from 25 to 80 °C and atmospheric conditions. The methodology employed guarantees anoxic conditions to avoid the presence of oxidized species. Anoxic conditions are provided by preparing the sample in a glove box flushed with pure nitrogen (99.999%) and stabilizing the solid using ultra-pure. The case of FeS is more critical in terms of having free oxygen conditions. In this case, the ultra-pure water was first distilled and then degassed. This precaution was made since iron (II) can easily be oxidized to iron (III).

4.6 Results

The results for the solubility measurements of FeS and PbS at temperatures from 25 °C to 80 °C are reported. The first part of this section shows a preliminary analysis of the presence of fine particles in the aqueous solution. Then the membrane pore size is assessed. The last sections describe the results obtained for the determination of the time required to reach steady state conditions and the dependency of the solubility on temperature.

4.6.1 Dependency on initial mass

Fine particles in the aqueous solution in the case of ZnS (see Chapter 3) were found to influence the results obtained by ICP-OES. The same analysis was done for FeS. The results are presented in Figure 4.2.

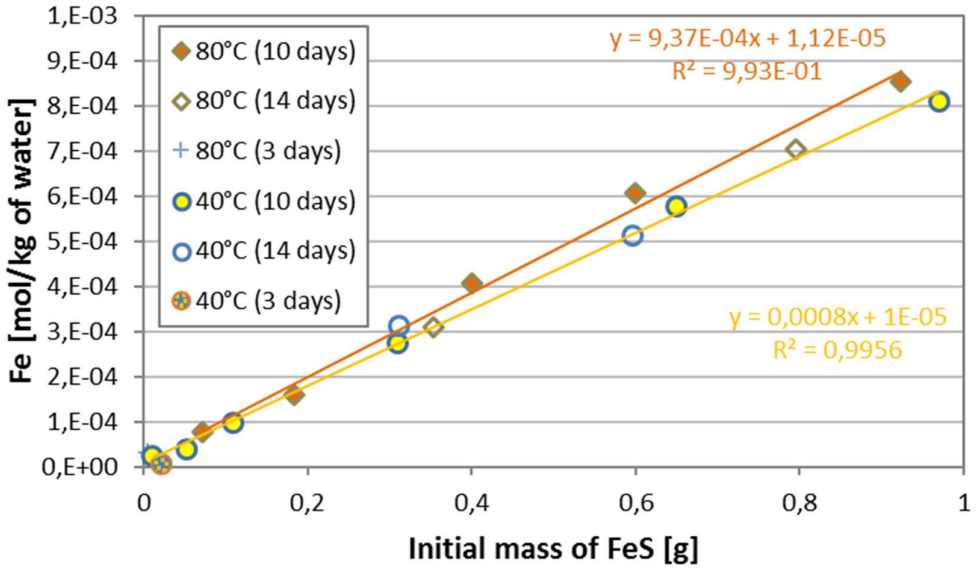

Figure 4.2 Dependency on the ZnS initial mass on the concentration

It is evident from the results shown in Figure 4.2 that the concentration of Fe depends on the initial mass of the FeS. This shows clearly that fine particles are present in the aqueous solution when using a membrane pore size of 0.45 µm. Therefore, a particle size analysis was carried out to determine the membrane pore size that will retain the FeS solid particles. The particle size analysis is presented as follows.

The analysis on the initial mass dependency for PbS was not performed as it was observed from the ZnS and FeS cases that the particle size distribution analysis will provide more information regarding the filtration conditions.

4.6.2 Particle size distribution

The particle size distribution of FeS and PbS was determined using a laser diffraction method [21]. The results are presented in Figure 4.3. Figure 4.3 shows the particle size distribution of (a) FeS and (b) PbS measured at two different conditions.

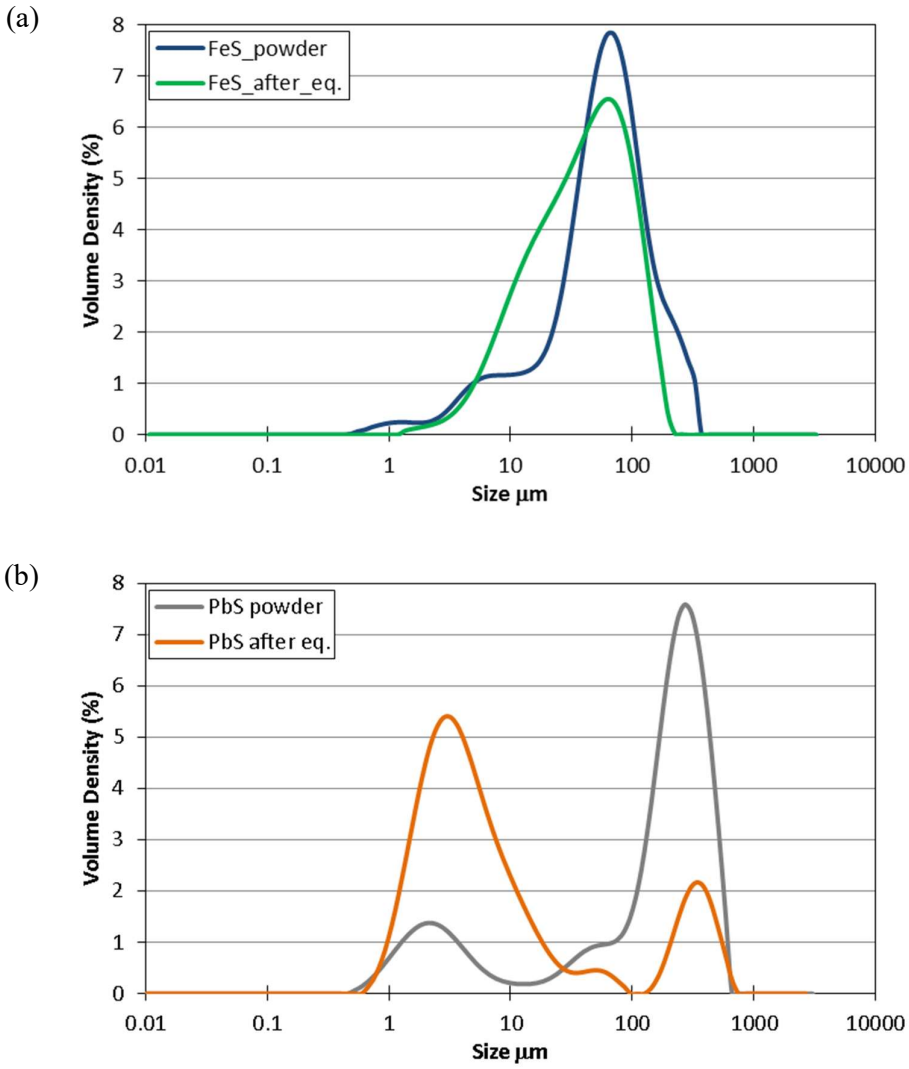

Figure 4.3: Particle size distribution of (a) FeS (b) PbS measured as initial solid (powder) and after equilibrium experiment

First, the solid was measured in powder form and secondly dispersed in ultra-pure water (after eq. conditions were achieved). The particle size of FeS in powder form is distributed between 0.38 – 330 µm. The 7.8 % of the particles have a particle size of 62.7 µm.

The FeS analyzed in dispersed form shows a similar distribution as the powder form. The particle size ranges from 1 µm to 255 µm with most of the particles having a particle size of 62.7 µm. Both analyses verify that the pore size of the membrane chosen is adequate since the results show there are no particles smaller than 0.22 µm.

In the case of PbS the particles in powder form are distributed between 0.46 and 3080 μm. 7.6 % of the particles have a size of 272.4 μm. This distribution confirms that 100% of the particles are larger than the pore size (0.22 μm) of the filtration membrane used during the experiments. The distribution of the particle size after the equilibrium experiment is similar. No particles smaller than 0.22 μm were found, instead it is observed that PbS powder tends to form larger agglomerates, since the smallest particle size observed is 0.67 μm (1.4 times larger than the smallest particle size in powder form). 5.48 % of the particles in dispersed form have a size of 3.55 μm. These results confirm that no fine particles could pass through the filtration membrane.

During the assessment of the membrane pore size, large concentrations of Fe and Pb were measured in the filtrate. A reduction of the concentration of Fe and Pb up to 93% was in some cases obtained by using filters with the correct pore size.

4.6.3 Equilibration time determination

The equilibration time determination is a key factor in solubility studies. The equilibration time represents the time required to obtain a saturated solution and it is affected by temperature. Equilibration time is referred as the time at which no significant changes in Fe and S concentration are observed. At this time, it is assumed that the dissolution process has ended and therefore the solution has reached equilibrium conditions. The solid and the aqueous phase are allowed to stay in contact for sufficient time (up to 14 days) to ensure that the solubilization process takes place independently of particle size.

The results for FeS are presented in Figure 4.4 and for PbS in Figure 4.5; as molality b ($mol \cdot kg_{water}^{-1}$) versus time at temperatures between 25 °C and 80 °C. The data for FeS are reported in Table 4.1.

It is observed in Figure 4.4 that the concentration of Fe and total sulfur remains almost constant in a range of time between 1 and 13 days at 25 °C and 40 °C. At higher temperatures (60 °C and 80 °C) the concentration of Fe and total S increases with time. An increase of 8.6 times is observed in the concentration of Fe from 1 day to 13 days at 40 °C. A more significant increase is observed in Figure 4.4d at 80 °C: the concentration of Fe is 42.3 times higher after 13 days compared to the concentration after 1 day. A plateau is not clearly identified at 60 °C neither at 80 °C. This suggests that the concentration of Fe and total sulfur may continue increasing over time. Figure 4.4a and Figure 4.4b show that the equilibrium conditions are achieved at around 6 days. This agrees with the studies on

equilibration time for pyrrhotite done by Tewari et al. [10]. Tewari et al. [10] found that 7 days were required to achieve equilibrium conditions in the case of pyrrhotite.

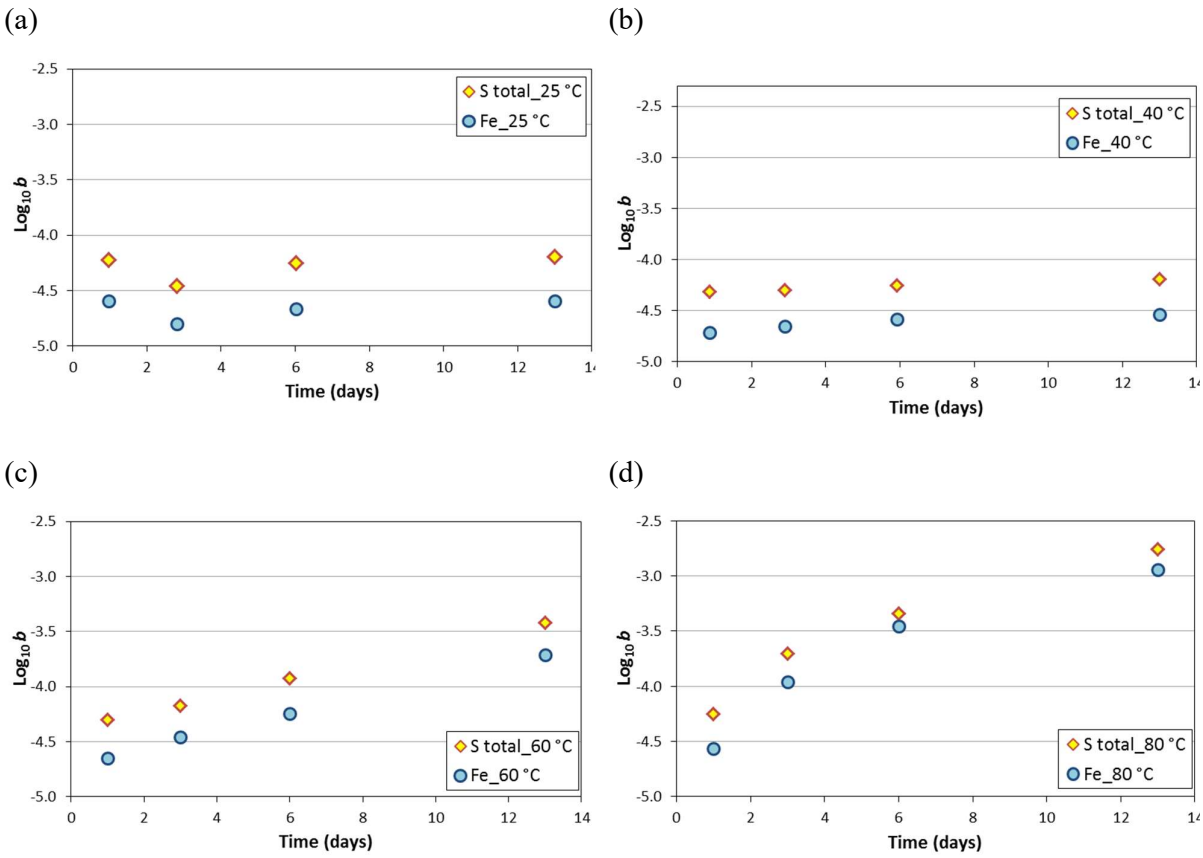

Figure 4.4. Determination of equilibration time for FeS

The variation of the equilibration time with temperature suggests that equilibrium conditions are achieved faster at low temperatures (25 – 40 °C) than at higher temperatures (60 – 80 °C).

The variation of the concentration of total sulfur with respect to time exhibits the same behaviour as observed for Fe. There is a noticeable difference between the concentration of Fe and total sulfur. This difference is observed to remain almost constant, meaning that the concentration of total sulfur is between 2.6 and 1.3 times higher than the concentration of Fe. It is interesting to note that there are larger differences between the concentration of total sulfur and Fe at low temperatures (25 – 40 °C) than at higher temperatures (60 – 80 °C). No evidence of sulfur in significant amounts present in blank samples was found. Therefore, the hypothesis of the presence of contaminants is discarded. Other hypothesis could be a difference in the composition of the starting material FeS. As mentioned in Section 4.4.2, the XRD analysis indicated that the starting FeS material contained less Fe than S.

This could explain some of the difference in concentration observed for Fe and total S in Figure 4.4. The lower concentration of Fe with respect to total S can also be due to precipitation of another Fe compound such as an oxide or hydroxide.

Table 4.1 Solubility data for FeS at temperatures between 25 and 80 ˚C at atmospheric pressure. Equilibration times between 1 and 13 days. The concentrations correspond to the average of the data points reported.

Eq. time (days)	Temp. (˚C)	Fe concentration [mol·kg^{-1} H_2O]x10^7	Data points	S_{Total} concentration [mol·kg^{-1} H_2O]x10^7	Data points
1	25	256.16 ± 1.7	3	602.72 ± 17.4	3
	40	195.05 ± 5.1	3	489.27 ± 7.7	3
	60	225.99 ± 45.7	6	502.05 ± 14.9	6
	80	271.44 ± 35.3	6	560.89 ± 44.6	6
3	25	159.99 ± 1.7	3	347.67 ± 10.5	3
	40	221.48 ± 7.8	6	503.40 ± 93.1	6
	60	350.99 ± 24.7	6	673.12 ± 11.4	6
	80	1093.36 ± 21.9	6	1981.20 ± 97.5	6
6	25	216.68 ± 12.1	6	560.42 ± 50.3	6
	40	262.23 ± 3.6	6	560.40 ± 98.9	6
	60	575.01 ± 10.1	5	1191.65 ± 13.6	5
	80	3492.99 ± 149.6	6	4547.83 ± 343.4	6
13	25	253.82 ± 16.5	6	638.57 ± 215.2	6
	40	291.10 ± 14.1	6	649.78 ± 103.5	5
	60	1937.36 ± 27.7	3	3816.65 ± 38.6	3
	80	11481.25 ± 68.4	3	17399.34 ± 70.1	3

The results for PbS are presented in Figure 4.5. The data are reported in Table 4.2. The concentration of Pb and S remain constant over the range of time studied at 25 ˚C as observed in Figure 4.5a. The constant concentration conditions suggest that equilibrium conditions are achieved in a matter of hours (less than one day) at 25 ˚C.

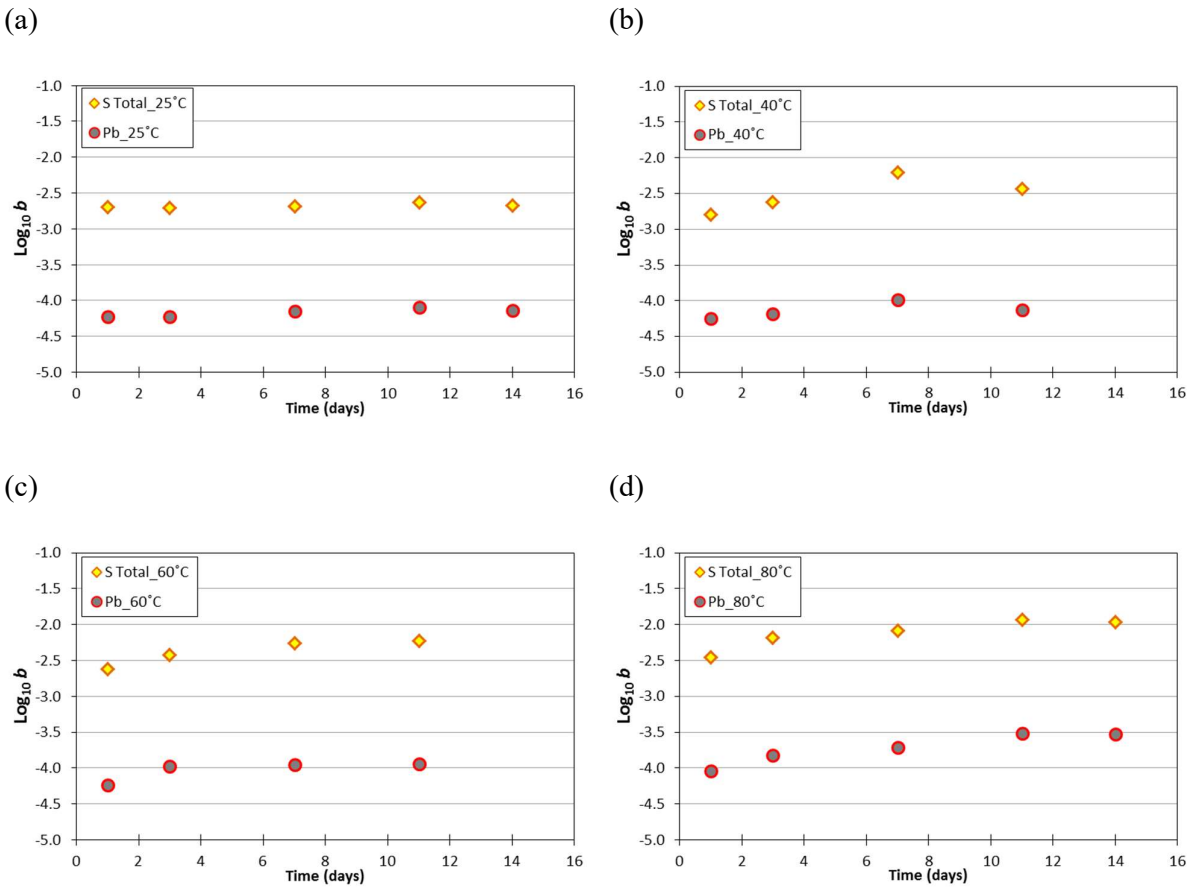

Figure 4.5 Determination of equilibration time for PbS

The scenarios at temperatures between 40 and 80 ˚C look slightly different. An increase in concentration for Pb and S is observed between 1 and 7 days. Beyond 7 days, the figures exhibit a plateau meaning that equilibrium conditions have been achieved. At certain temperatures (25 and 40 °C) a slight decrease in the concentration is observed (8% and 27% respectively). The decrease is larger than the experimental error. Also, a decrease of 2% is observed at 80 °C but the decrease is between the experimental error for Pb. The decline in concentration (at 25 and 40 °C) is perhaps an indication that the steady conditions are not achieved even after 11 days.

Table 4.2 Solubility data for PbS at temperatures between 25 and 80 ˚C at atmospheric pressure. Equilibration times between 1 and 13 days. The concentrations correspond to the average of the data points reported.

Eq. time (days)	Temp. (˚C)	Pb concentration [mol·kg^{-1} H_2O]x10^6	Data points	S_{Total} concentration [mol·kg^{-1} H_2O]x10^6	Data points
1	25	6.0 ± 0.4	8	2.0 ± 0.1	8
	40	5.7 ± 0.4	7	1.6 ± 0.1	6
	60	5.8 ± 0.5	9	2.4 ± 0.2	9
	80	9.0 ± 1.0	5	3.5 ± 0.3	6
3	25	5.9 ± 0.4	17	2.0 ± 0.1	16
	40	6.6 ± 1.0	11	2.4 ± 0.4	12
	60	10.5 ± 0.5	7	3.7 ± 0.1	9
	80	14.9 ± 0.3	7	6.5 ± 0.7	6
7	25	7.1 ± 0.5	6	2.1 ± 0.2	8
	40	10.3 ± 2.7	6	6.2 ± 3.0	6
	60	11.1 ± 0.3	8	5.5 ± 0.6	7
	80	19.2 ± 0.9	9	8.3 ± 0.3	7
11	25	8.0 ± 0.3	8	2.4 ± 0.1	4
	40	7.5 ± 0.3	7	3.7 ± 0.3	7
	60	11.6 ± 0.8	7	5.9 ± 0.8	6
	80	30.6 ± 2.0	5	11.8 ± 1.2	6
14	25	7.3 ± 0.2	7	2.1 ± 0.3	7
	80	29.9 ± 1.4	7	10.9 ± 0.1	7

Table 4.3 pH values for PbS solubility measurements

Temperature (°C)	Eq. time (days)	pH
25	7	5.25 ± 0.1
25	14	4.86 ± 0.6
40	1	4.38 ± 0.0
80	1	5.32 ± 0.3
80	14	5.39 ± 0.1

A significant difference between the concentration of Pb and S is observed in this case. The concentration of total sulfur is 39 times higher than the concentration of Pb. This observation cannot

be attributed to the composition of the initial solid. As mentioned in Section 4.4.2 the composition of the initial solid was determined to correspond to stoichiometric PbS. A possible explanation of this difference in concentration is the precipitation of PbO or $Pb(OH)_2$. This would also explain a slight drop in pH during the equilibrium experiment (see Table 4.3). The difference between the concentrations of metal ion and of total sulfur was observed as well in an earlier study on ZnS Figueroa et al. [20]. No evidence of contamination nor use of non-stoichiometric ZnS could explain the differences in concentration observed between Zn and total S Figueroa et al. [20]

4.6.4 Effect of temperature on FeS and PbS solubility

The effect of temperature on the solubility of FeS is presented in Figure 4.6. The results are plotted as molality b_{FeS} ($mol \cdot kg_{water}^{-1}$) versus temperature and are compared with published data for FeS solubility. FeS solubility was taken to be equal to the Fe molality. Differences in the starting material in earlier data are indicated in Figure 4.6 since direct comparison cannot be done due to differences in crystal structure and composition.

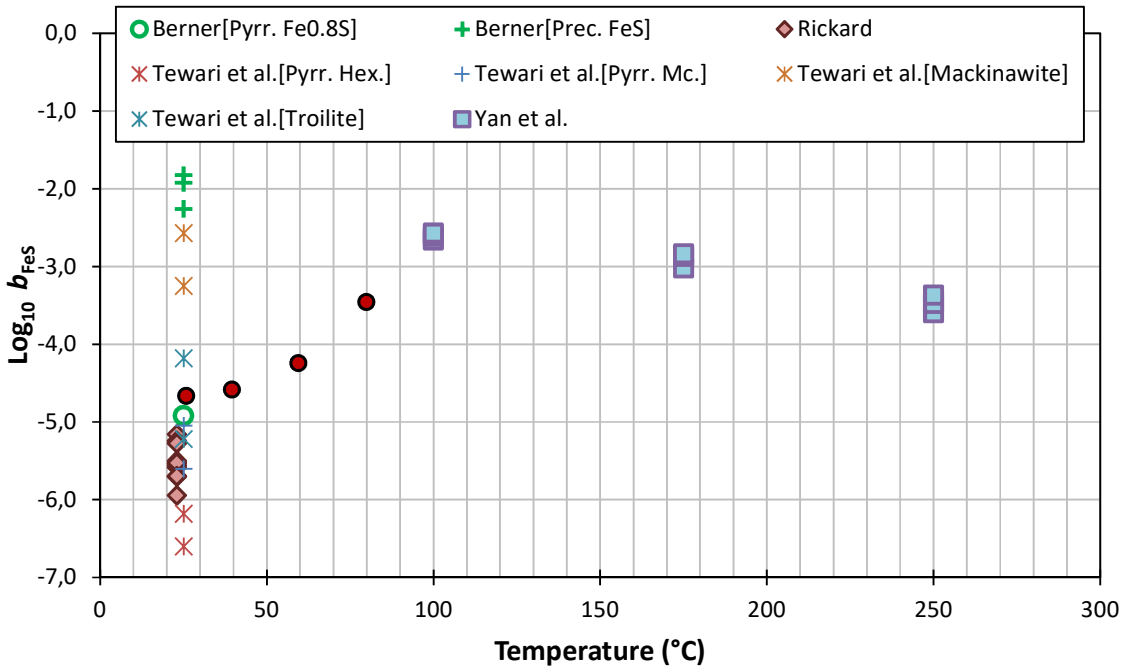

Figure 4.6 Effect of temperature on FeS in aqueous solution. Data taken from Tewari et al. [10] for pyrrohotite hexagonal, mackinawite, pyrrhotite monoclinic and troilite; Rickard [11] at pH between 6.5 and 8.0; Berner [12] for pyrrhotite and precipitated FeS and Yan et al. [13] in 1M NaCl solution.

The results obtained in this study for FeS solubility indicate that the solubility of FeS increases linearly as temperature increases (except for the data point obtained at 25 °C). The solubility of FeS increases approximately 54 times at 80 °C compared to solubility data obtained at 25 °C.

Most of the data for FeS solubility found in literature are measured at 25 °C. The high scattering observed in the data at 25 °C is mainly due to the different composition and crystal structure of the initial solid material. The data presented in Figure 4.6 differ in pH, salinity and crystal structure. Thus, this comparison is intended only for a descriptive purpose of FeS in aqueous solution. This is thecase of the studies on solubility made by Tewari et al. [10] who measured the solubility of 4 different types of iron sulfide. As it can be seen in Figure 4.6 the most soluble form of FeS used by Tewari et al. [10] was Mackinawite and the least was Pyrrhotite with hexagonal crystal structure. The value presented by Berner [12] and the data points published by Tewari et al. [10] at 25 ˚C of hexagonal pyrrhotite are comparable to our value since the starting material has a similar composition and crystal structure. The value presented by Berner [12] is expected to exhibit a high value of solubility since it was measured in aqueous solutions previously saturated with H_2S. Our value at 25 ˚C is slightly larger than the value presented by Berner [12] but the trend observed for our data matches with the data point reported by Berner [12]. Compared to the data published by Tewari et al. [10] the value obtained here is approximately 23 times larger. The values obtained by Tewari et al. [10] were measured in the presence of H_2S and it was expected that the value reported here is lower. Apart from the two studies by Berner [12] and Tewari et al. [10] discussed earlier, comparison with other studies is challenging. The solubility data reported by Yan et al. [12] were obtained using troilite in an aqueous solution of 1 M NaCl. Troilite exhibits higher solubility values than pyrrhotite as observed in the data published by Tewari et al. [10].

The solubility for PbS as a function of temperature is presented in Figure 4.7. The tendency of the solubility of PbS is to increase as temperature increases. The increase is not as remarkable as observed in the case of FeS. The solubility of PbS increases 3 times by increasing temperature from 25 °C to 80 °C. To better understand the results obtained in this study, our results are compared with previously published data. The data available in literature are scarce and differ slightly between authors in terms of pH and salinity (among variations during the experimental procedures). Therefore, direct comparison may not be appropriate, but it brings insights regarding the behavior of PbS in aqueous solutions.

Most of the data published for PbS solubility were obtained at 25 °C. This is the case of Biltz [22] Nims and Bonner [17], and Weigel [16]. Biltz [22] and Weigel [16] measured the solubility of freshly precipitated PbS while Nims and Bonner [17] measured the solubility of the mineral form. The value reported by Nims and Bonner [17] is expected to be lower (as reported in Figure 4.7) as the mineral form was used. The mineral form of aged PbS has a more stable structure that tends to be less soluble in water. Our value obtained at 25 ˚C is 20 times higher than the values obtained by Biltz [22] and Weigel [16]. The initial material in three of the cases is precipitated PbS like we used in our work, and there is not a clear reason why our solubility value is higher. It could be expected that the value reported by e.g. Weigel [16] was higher than the one reported here since measurements of the solubility were done by means of conductivity. Conductivity measurements could overestimate the contribution of Pb ions as impurities could add to the conductivity value.

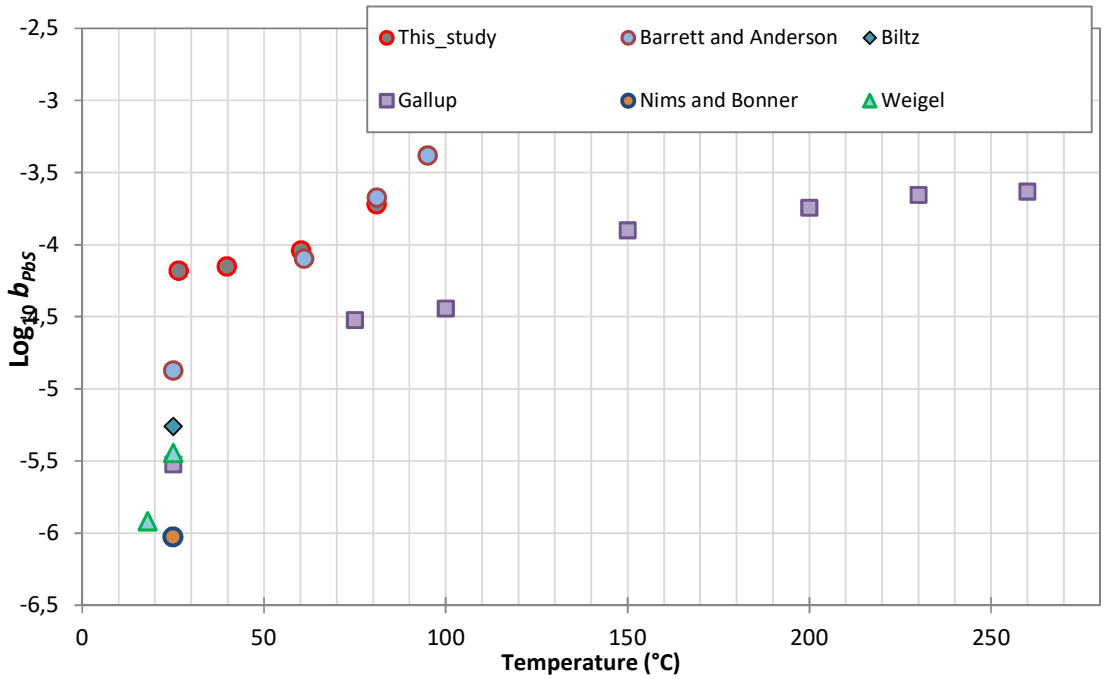

Figure 4.7. Effect of temperature on PbS solubility in aqueous solution. Data obtained from, Barrett and Anderson [19] at pH between 0.46 and 2.34 in 3 m NaCl solution; Biltz [22]; Gallup [13] at pH 5.5 and 4.3 m NaCl; Nims and Bonner [17] and Weigel [16].

PbS exhibits higher solubility at low temperatures (25 - 40 ˚C) than FeS. At higher temperatures (40 - 100 ˚C) FeS is more soluble than PbS. Besides, the effect of temperature on solubility is more remarkable for FeS than in PbS.

The values reported here are comparable to those obtained by Barrett and Anderson [19], in 3 M NaCl solutions and. This indicates that the solubility values obtained in this study are somehow elevated. Our data were carefully measured using the appropriate pore size for the filtration membrane and the presence of impurities was tested without finding contaminating Pb sources. Therefore, the presence of fine particles or Pb contaminants are two hypotheses discarded as causes for elevated solubility values. The elevated values are possibly occasioned by a wrong determination of the equilibration time. The particle size analysis shown in Figure 4.3 shows that PbS coarse particles tend to break apart or reduce their size in dispersed form faster than FeS. In solid form, PbS particles between 0.1 and 10 μm constitutes 18% of the sample. While, in dispersed form the same range of particle sizes constitutes 69% of the sample. This is an increase of almost 4 times the availability of fine particles in dispersed form. Fine particles will solubilize faster than coarse ones and this might tend to show initial high concentrations of Pb as observed in Figure 4.5. However, a decrease in Pb concentration is observed at different temperatures and extended times (beyond 11 days). This might point that the PbS aqueous system is still not at equilibrium conditions and that the concentration of Pb will continue decreasing over time until steady conditions are achieved.

4.7 Reliability of the analytical technique

The concentration of iron and total sulfur contaminant from the ultra-pure water were measured as 6.24×10^{-8} mol·kg^{-1} and 5.2×10^{-7} mol·kg^{-1} respectively. The concentration of the contaminants does not constitute a significant contribution to the concentration measured for solubility experiments.

The error estimation of the measurements was determined using standard solutions of the elements studied here. The relative error estimated for the reported Fe concentrations oscillates between 0.4 % and 2.9% and Pb between 1.4% and 2.8%. For total sulfur, the error estimate oscillates between 1.1% and 2.9%.

The concentration of Pb measured in the ultra-pure water was 1.8×10^{-8}. This value present high uncertainty since the concentration was above the detection limit of the ICP-OES but below its quantification limit. Nevertheless, the value is significantly low that it will not influence the solubility measurements.

4.8 Conclusions

The solubility of FeS and PbS was measured in aqueous solutions at temperatures between 25 ˚C and 80 ˚C and atmospheric conditions. The purity of the initial solid was analyzed by X-Ray diffraction. The results showed a high purity product with a near stoichiometric composition ($Fe_{0.98}S$ or $Fe_{0.879}S$) corresponding to pyrrhotite. The spectrum for PbS showed that the initial solid was galena with stoichiometric composition. Initial characterization of the initial matter is a vital step to explain the behavior of the sulfides during the solubility measurements. Anoxic conditions were guaranteed during the solubility experiments since Fe is easily susceptible of oxidation. Low dissolved oxygen levels in the ultra-pure water to stabilize the solid required attention to detail. The ultra-pure water was firstly distilled and then degassed with high purity nitrogen.

Equilibrium conditions were guaranteed by allowing the solid and the aqueous phase to stay in contact for sufficient time (up to 14 days). In this manner, it is assured that the solubilization process takes place and steady conditions are reached. It was found that FeS in aqueous solution reached equilibrium in around 6 days. Variations in time were observed at different temperatures. It was concluded that equilibrium conditions are achieved faster at low temperatures (25 – 40 °C) than at higher temperatures (60 – 80 °C). Meanwhile for the PbS system equilibrium conditions at 25 °C were apparently achieved in a matter of less than 24 hours. At higher temperatures (up to 80 °C) it was found that the time required for equilibrium did not varied much. A decrease in Pb concentration after 11 days is observed suggesting that steady conditions might be achieved at extended times.

The solubility as a function of temperature was explored in the range between 25 and 80 °C. The solubility of FeS and PbS in aqueous solution both increase with increasing temperature. The effect is highest for FeS. The solubility of FeS at 80 °C was observed to be 54 times higher than at 25°C. Meanwhile, the solubility of PbS just increased 3 times by increasing the temperature from 25 to 80 °C. PbS solubility values reported are quite elevated if compared to data published by other authors. This observation supports the hypothesis that steady conditions perhaps were not achieved during the experiments carried out in this study.

References

[1] M.A. Kasnick, R.J. Engen, Iron Sulfide Scaling and Associated Corrosion in Saudi Arabian Khuff Gas Wells, Middle East Oil Show. SPE 17933 (1989). doi:10.2118/17933-MS.

[2] H. Nasr-El-Din, A. Al-Humaidan, Iron Sulfide Scale: Formation Removal and Prevention, Int. Symp. Oilf. Scale. SPE 68315 (2001) 13. doi:10.2523/68315-MS.

[3] A.J. Savin, B. Adamson, J.J. Wylde, J.R. Kerr, C.W. Kayser, T. Trallenkamp, D. Fischer, C. Okocha, Sulfide Scale Control: A High Efficacy Breakthrough Using an Innovative Class of Polymeric Inhibitors, SPE Int. Oilf. Scale Conf. Exhib. (2014). doi:10.2118/169777-MS.

[4] J.I. Al-Tammar, M. Bonis, H.J. Choi, Y. Al-Salim, Saudi Aramco Downhole Corrosion/Scaling Operational Experience and Challenges in HP/HT Gas Condensate Producers, (2014). doi:10.2118/169618-MS.

[5] H.A. Nasr-El-Din, A.Y. Al-Humaidan, S.K. Mohamed, A.M. Al-Salman, Iron sulfide formation in water supply wells with gas lift, in: SPE Int. Symp. Oilf. Chem., Society of Petroleum Engineers, 2001.

[6] W. Davison, The solubility of iron sulphides in synthetic and natural waters at ambient temperature, Aquat. Sci. 53 (1991) 309–329.

[7] D. Rickard, G.W. Luther, Chemistry of iron sulfides, Chem. Rev. 107 (2007) 514–562.

[8] S. Baraka-Lokmane, C. Hurtevent, H. Zhou, P. Saha, N. Tots, F. Rieu, TOTAL ' s Experience on the Development and Implementation of a Scale Management Strategy in Central Graben Fields, Soc. Pet. Eng. (2014) 1–17. doi:10.2118/169757-MS.

[9] G.M. Graham, C.S.A. MacPherson, C. Simpson, K. Orski, S.M. Heath, Development of Appropriate Test Methodologies for the Selection and Application of Lead and Zinc Sulphide Inhibitors for the Elgin/Franklin Fields, Soc. Pet. Eng. (2006).

[10] P.H. Tewari, G. Wallace, A.B. Campbell, The solubility of iron sulfides and their role in mass transport in Girdler-sulfide heavy water plants, Atomic Energy of Canada Ltd., 1978. AECL-5960.

[11] D. Rickard, The solubility of FeS, Geochim. Cosmochim. Acta. 70 (2006) 5779–5789.

[12] R.A. Berner, Thermodynamic stability of sedimentary iron sulfides, Am. J. Sci. 265 (1967) 773–785.

[13] C. Yan, P. Guraieb, R.C. Tomson, Solubility Study of Iron Sulfide FeS Under Extremely High Temperature Pressure in Strictly Anoxic, Various Ionic Strength Solutions, in: SPE Int. Oilf. Scale Conf. Exhib., Society of Petroleum Engineers, 2016.

[14] D.L. Gallup, G.R. Andersen, D. Holligan, Heavy metal sulfide scaling in a production well at the Salton Sea geothermal field, Trans. Geoth. Res. Counc. 14 (1990) 1583–1590.

[15] H.L. Clever, F.J. Johnston, The solubility of some sparingly soluble lead salts: an evaluation of the solubility in water and aqueous electrolyte solution, J. Phys. Chem. Ref. Data. 9 (1980) 751–784.

[16] O. Weigel, The solubility of the sulphides of the heavy metals in water, Z. Phys. Chem. 58 (1907) 293–300.

[17] L.F. Nims, W.D. Bonner, The Solubility of Galena and a Study of Some Lead Concentration Cells, J. Phys. Chem. 33 (1929) 586–590.

[18] R.J. Hamann, G.M. Anderson, Solubility of galena in sulfur-rich NaCl solutions, Econ. Geol. 73 (1978) 96–100.

[19] T.J. Barrett, G.M. Anderson, The solubility of sphalerite and galena in 1–5 m NaCl solutions to 300 C, Geochim. Cosmochim. Acta. 52 (1988) 813–820.

[20] D.C. Figueroa, P.L. Fosbøl, K. Thomsen, Determination of Zinc Sulfide Solubility to High Temperatures, J. Solution Chem. 46:1805 (2017). doi:10.1007/s10953-017-0648-1.

[21] R. Jones, Particle size analysis by laser diffraction: ISO 13320, Am. Lab. 35 (2003).

[22] W. Biltz, Experiments on ultramicroscopic determination of solubility, Z. Phys. Chem. 58 (1907) 288–292.

CHAPTER 5

Solubility Measurements at High Pressure and High Temperature

5.1 Introduction

Solubility of salts is highly influenced by changes in temperature and pressure [1,2]. Metal sulfides (ZnS, FeS, PbS) are particularly more influenced by temperature changes than pressure changes as already shown in few studies [3–6]. The abrupt changes in temperature and pressure during the extraction of oil from High Pressure/High Temperature reservoirs can trigger the formation of the unwanted deposits of minerals along the way up to the production site in an oil field. These deposits of minerals, i.e. scaling due to changes in the solubility of sulfides is of main concern in oil production, as it leads to large increase in the cost of production and potentially shutdown of a well.

5.1.1 Review of previous studies of solubility of sulfides at high temperatures

Solubility measurements at high temperatures are a challenging task in terms of experimental procedure. As discussed earlier in the Introduction of this document one of the key aspects for reliable solubility measurement is maintaining constant conditions. Different equipment has been designed and tested to measure the solubility of scale minerals during decades. However, concentration (solubility) measurement at constant pressure and temperature conditions is still a cumbersome task that needs further improvements. Relly [4] proposed a method to measure the concentration of zinc without sampling. The bomb (material: Haynes' Alloy 25) was designed to withstand pressures up to 345 bar and temperatures up to 200 °C. A porous capsule containing radioactive zinc was inserted in the bomb assuming that the solute dissolves in the water by means of diffusion. The bomb was only heated from one side since the other side was protected with a lead shield. The concentration of the radioactive Zn was measured using a scintillation probe connected directly to the bomb. This design lead to having different temperature zones in the liquid and therefore a non-homogeneous Zn concentration. Additionally, the gamma energy irradiating from the Zn was not strong enough. Other problems with this design were found related to interferences either from the solute capsule itself or

from zinc ions adsorbed onto the walls of the bomb. These interferences directly altered the readings in the scintillation probe. Relly [4] also considers the presence of suspended solid particles in the liquid phase. As demonstrated in Chapter 3 the presence of suspended solid particles will show higher solubility values. Thus, these experimental data might be significantly biased by these solid particles. This study shows that direct sampling is needed to achieve accurate and reproducible/reliable results. The same conclusion has been reached by Hemley et al. [7]. They measured the solubility of Fe, Pb, Zn and Cu sulfides in chloride solutions These solubility measurements were carried out at temperatures from 300 °C to 700 °C and pressures from 0.5 to 2 kbars. They compared two methods for sampling: a fast quenching technique and a method withdrawing the sample at experimental T and P. The first method of quenching the vessel is a fast a practical way to measure solubilities but it is highlighted by the authors that the method is feasible unless the amount of solid that precipitates during quenching is determined. In fact, they observed precipitation of sulfides, though the precipitate was not directly observed, decrease in pH values indicated the presence of sulfide precipitate and formation of HCl. The direct sampling method at temperature and pressure of the experiments was tested extracting an aliquot through an internal filter. This sampling method prevents reversible reactions that occur when quenching the aqueous solution. The only drawback pointed out by the authors of this method was clogging of the tubbing, as several samples were withdrawn over a period of time with no change of filter [7].

A direct sampling experimental setup has been designed by Barnes [8]. This experimental setup consists of a stainless-steel reaction vessel of volume 1.1 L, suitable for measuring the solubility of minerals at temperatures ranging from 25 °C to 400 °C. This rocking vessel is heated by means of a coiled furnace and it is pressurized by loading H_2S into the vessel (1-304 bar). Deionized and de-aerated water is pumped into the reaction vessel using a displacement piston that uses water instead of oil as lubricant to avoid contamination during experiments [8].

The sampling process in Barnes' experiments was carefully designed and consisted of two steps: first a sample (either liquid or gas phase) is withdrawn at experimental conditions by a double valve system. Temperature changes during the sampling are considered negligible since the sampling tube is preheated to the experimental conditions. Pressure drop is estimated at 0.5%. Then the sample is transferred to a glass container near standard conditions by draining the sampling line. The solubility of minerals is determined using the measured initial quantities of gas, liquid and solid and a constant sample size of 5.24 ± 0.02 mL. This is relatively small volume compared to the volume of reaction vessel, thus it allows taking several samples using the same aqueous solution in the reaction vessel.

This is advantageous as reproducibility of the method can be determined. On the other hand, the draining of the sample at standard conditions could lead to precipitation of solid and consequently erroneous determination of the solubility values [8].

Tagirov et al. [5] measured the solubility of ZnS at 100 °C and 150 bars using a flow-through reactor. The ZnS initial solid was recrystallized in a furnace at 850 °C. The particle size obtained after the recrystallization process was 0.1 mm. Additionally, the initial solid was washed with deionized water until obtaining a clear solution. This washing was performed to remove either contaminant and fine particles adhered to the coarse grains. However, this procedure does not guarantee the absence of fine particles in the solution [5].

Two solutions were employed in Tagirov et al. [5] experiments: the first solution is water saturated with H_2S and the second solution contains either NaOH or $HClO_4$ depending on the pH conditions of the experiments. The sampling was carried out using a titanium back pressure regulator. A titanium frit (2 μm) was installed at the end of the reactor for sampling purposes. The sample was collected in a flask cooled with water. Similar to study by Barnes [8], the fast cooling may trigger the precipitation of ZnS.

Overall, this study lacks an analysis of particle size distribution or detection of fine particles in the liquid sample. This analysis is essential since fine particles might have passed through the frits, leading to erroneous determination of Zn concentration using atomic absorption spectroscopy (AAS).

Similar to the study above, Yan et al. [3] carried out solubility measurements of FeS at pressure up to 1720 bar and 250 °C using a flow-through apparatus. The main purpose of their experiments was to reproduce the downhole conditions of an oil field to investigate the scaling phenomenon. This apparatus was made of Hastelloy C-276. The feed solution (NaCl brine) was injected to the packed column (FeS in troilite phase) using a high-pressure pump. The same packing material was tested at different salinities (1M and 3M NaCl), temperatures and pressures. The packing material was analyzed after the experiments by SEM. It was observed a change of phase for FeS, from troilite (initial solid) to pyrrhotite. Since their experiments were carried out with no change of the packing material, the solubility values obtained correspond to different compositions of triolite and pyrrhotite [3].

The experiments are claimed to be carried out at anoxic conditions (<1 ppb) using a proprietary method of the authors. The samples were withdrawn using a back-pressure regulator at experimental conditions. A qualitative particle size analysis was done using scanning electron microscope (SEM)

finding a wide range of particles sizes. The scanning shows particles smaller than 1 μm though there is not an inline filter installed in the sampling line. To avoid the precipitation of the solid, EDTA was injected to the sample before temperature and pressure drop [3].

Furthermore, the authors do not present information regarding the equilibration time for this specific experiment. Though, in a previous publication [9], they provided the retention time for this flow-through apparatus, i.e. the time to reach equilibrium conditions was 6.5 minutes (0.5 mL/min). This retention time was determined at room temperature and they assumed that equilibration time is reached faster at higher temperatures and pressures.

From the experimental set-ups described above the following is concluded:

- Temperature and pressure conditions should be constant even during sampling to avoid precipitation.
- Fast quenching of the sample leads to precipitation; therefore, this method is not suitable for determination of solubility at high temperatures.
- The use of packing column is a viable solution, but the packing material should be replaced often (the solid phase changes over time).
- Use of an inline filter is essential to retain the small particles that are present in the solution.

The following section presents an experimental apparatus for solubility determination considering the contemplations mentioned above.

5.2 Experimental set up

To address issues mentioned above for solubility measurements of mineral salts at high pressure and high temperature, we have designed and build an experimental set-up at the DTU Chemical and Biochemical Department. This equipment was developed to carry on solubility measurements of low solubility salts, and it is specially aimed for the aqueous systems of ZnS, PbS and FeS. These are of specially interest as they are not well understood nor studied scaling materials. The equipment is illustrated in Figure 5.1.

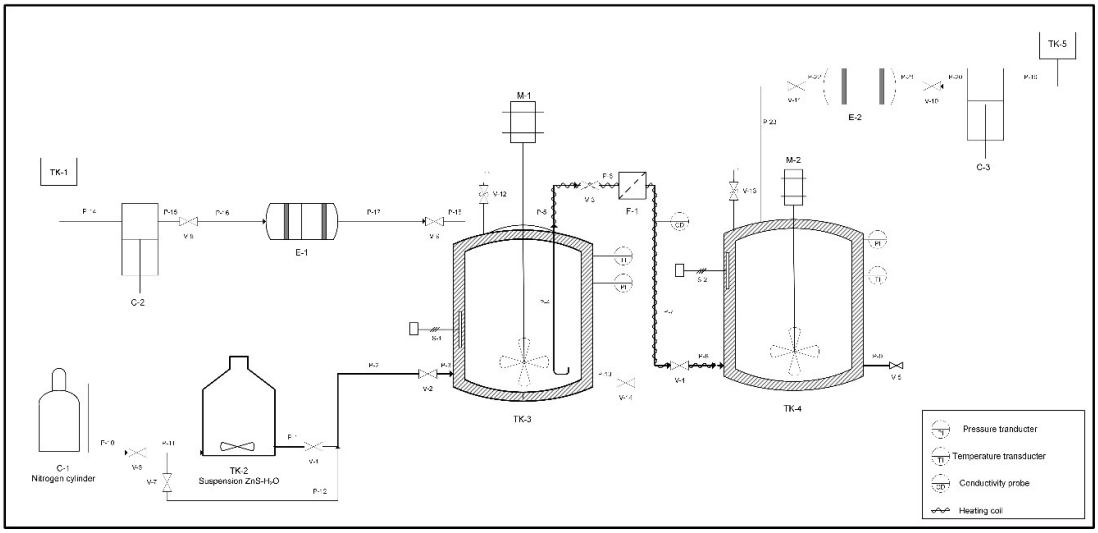

Figure 5.1 HT Titanium Cell Flowsheet

The equipment consists of 2 cells Equilibration Cell (TK-3) and Dilution Cell (TK-4), made entirely of Titanium. Each cell is equipped with a safety valve in case of overpressure (V-12 and V-13) (max. 60 bars), pressure transducers, 3 heating cartridges inserted in the wall of the cell, a magnetic stirring motor (M-1 and M-2) and a thermocouple. The cells can withstand temperatures up until 200°C and 60 bar.

The equilibration cell has a volume of 300 mL. This cell is the main unit of the equipment in which the solution is kept at constant temperature and pressure. The temperature and pressure probes provide continuous monitoring to guarantee constant conditions during equilibration time.

The internal diameter of the cell (TK-3) is 75 mm and the external diameter is 128 mm. The height of the cell is 150 mm. The bottom part of the cell is equipped with two valves for loading the cell (V-2) and sampling (V-14). The lid of the cell is made of titanium with an O-Ring and 6 bolts to seal the cell. The lid consists of 5 ports that were fitted with: (1) a stirrer, (2) a thermocouple, (3) a sampling assembly (transfer line), (4) a pressure transducer and safety valve, and (5) an inlet for injection of silicone oil. The silicon oil is used to control the pressure. Detailed drawings of the cells are presented in Appendix A.

The dilution cell (TK-4) has a volume of 400 mL. This cell is used for diluting a known volume of sample transferred from the equilibrium cell. This cell is kept at the same conditions as the equilibrium cell, to avoid potential deposition of minerals. This is essential especially when measuring solubility of very low solubility minerals, i.e. FeS, ZnS, PbS. Small changes in the

experimental conditions might lead to significant change in the mineral concentration and therefore low reproducibility of measurements.

This cell has similar dimensions to the equilibration cell. The internal diameter of the cell is 75 mm and the external diameter is 128 mm. The height of the cell is 193 mm. The bottom part of the cell is equipped with a valve for sampling (V-5). The lid of the cell has the same number of ports as the equilibration cell, except for the port for the transfer line.

The two cells are connected through a transfer line. The main purpose of this line is sampling from the equilibration cell at constant temperature and pressure. The transfer line is heated by means of two external heating coils placed on the surface of the tubing. The transfer line has an inline filter (F-1) which body and cartridge (pore size 0.5 μm) are made of stainless steel. This filter ensures removal of very fine particles. No cartridge with smaller pore size was available. The pore size guarantees that at least 70% of the particles are retained (based on the particle size analysis reported in Chapter 3). To mitigate the presence of fine particles the sampling assembly is located 5 centimeters above the bottom of the tank and stirring is stopped at least 1 hour before sampling.

Thus, this equipment addresses several issues presented in previous works. It avoids interferences from other metallic ions since is made of Titanium. The heating cartridges installed in the wall of the cells allow uniform heating of the solution avoiding zones at different temperatures. The sampling method at constant pressure and temperature and immediate dilution prevents the solids from precipitating.

5.3 Materials description

The experiments were performed using ZnS powder of 99.99% purity (from Sigma-Aldrich) and with a particle size of 10 μm. The characterization of the ZnS was presented in Chapter 3. NaCl 99.999% trace metal basis grade from Sigma Aldrich was used as tracer during the experiments to determine the dilution rate.

5.4 Methodology

This section describes the methodology developed to measure the solubility of sulfides at elevated temperatures. The developed methodology addresses the main shortcomings of previous designs,

highlighted in described in Section 5.1.1. The method described here was established based on the method developed for solubility measurements below 100 °C described in Chapter 3.

The performed experiments cover relevant temperature and pressure conditions for ZnS. The experiments were carried out at temperatures between 95°C up to 175 °C and pressures up to 50 bars. The success of the experiments depends upon previous preparation of the equipment. It is important to assure that the experiments are carried out at anoxic conditions. The equipment is flushed with nitrogen to evacuate the oxygen present inside the tubing and cell previous any experiment. Hence, the N_2 cylinder (C-1) is connected to the equilibration cell letting the gas flow through the transfer line (V-3 and V-4 are open) and reaching the dilution cell (TK-4). The Equilibration Cell TK-3 and Dilution Cell TK-4 are flushed with N_2 99.999% for 2 hours to evacuate the oxygen present in the equipment.

5.4.1 Sample preparation and Loading of the equilibration cell.

A great importance was given to the preparation of the sample as it is one of the main sources of uncertainty when measuring low concentrations. The preparation of the sample was carried out in closed and strictly-controlled anoxic atmosphere in a glove box flushed with N_2 (99.999% purity). The concentration of oxygen is constantly monitored both in the solution (using a Dissolved Oxygen Probe) and in the box (Oxygen detector). The aqueous sample was prepared in a 0.1 M NaCl solution previously degassed in a 0.5L borosilicate glass flask (Figure 5.1 TK-2Then the flask was sealed and taken out from the glove box. Afterwards, the flask (TK-2) is connected to the Equilibration cell (TK-3) using a flexible hose. The solution is transferred to the equilibration cell by flushing N_2 through it. It is important to keep the nitrogen flowing to avoid the presence of oxygen in the cell. This approach assures low oxygen concentration but also avoiding potential contaminations of the sample. After the solution has been transferred to the equilibration cell, silicon oil is injected from the top of the equilibration cell through one of the ports located at the lid of the cell. Then the stirrer (M-1) is turned on and the speed of the rotor is set to 300 rpm in the Control Box (Figure 5.2d).

5.4.2 Pressure and Temperature settings

The pressure control unit consists of a syringe pump (ISCO) and an auxiliary two chambers piston-cylinder. The ISCO pump uses distilled water as working fluid. The auxiliary cylinder uses water and silicon oil as working fluids. The chamber of the auxiliary cylinder filled with water is connected to the ISCO pump and the chamber filled with silicon oil is connected to the equilibration cell. The control of the pressure is automatic and the set point for the pressure in the equilibration respectively

dilution cell is set through the pressure control unit (see Figure 5.2). The time development of the pressure and temperature values in several points of the experimental units, e.g. equilibration cell, dilution cell, transfer line; are shown in a dedicated software (see Figure 5.3).

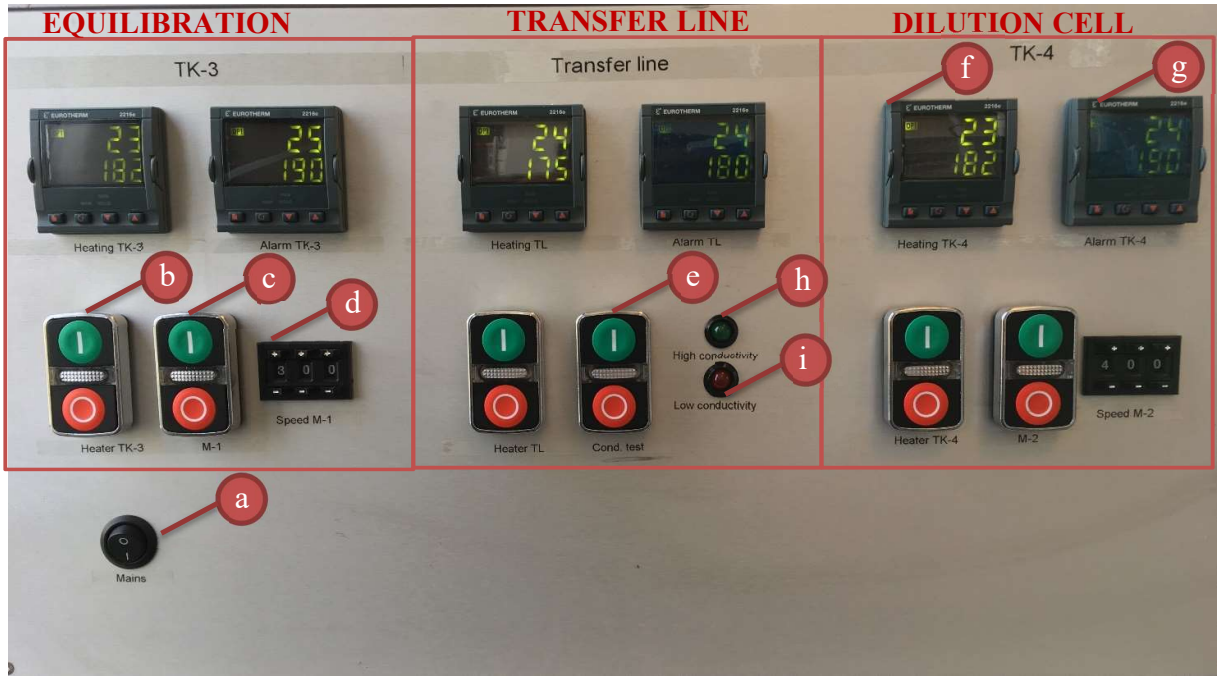

Figure 5.2 Control Box for the HT Titanium Cell. (a) Main switch (b) Heating system swith (c) Stirrer switch (d) Manual setting for stirrer speed (rpm) (e) Conductivity test swith (f) Temperature settings (g) Safety control for temperature (h) High conductivity indicator (i) Low conductivity indicator

Similar to the pressure control system, the temperature through the whole system is maintained at the set point using automatic control. Note that the heating of the setup should be started only when the pressure reached the predefined value. The heating system is started from the Control Box for the equilibration cell (Figure 5.3b) respectively dilution cell (Figure 5.3g). Note that the cells and the transfer line are insulated to avoid heat loss and any accidents.

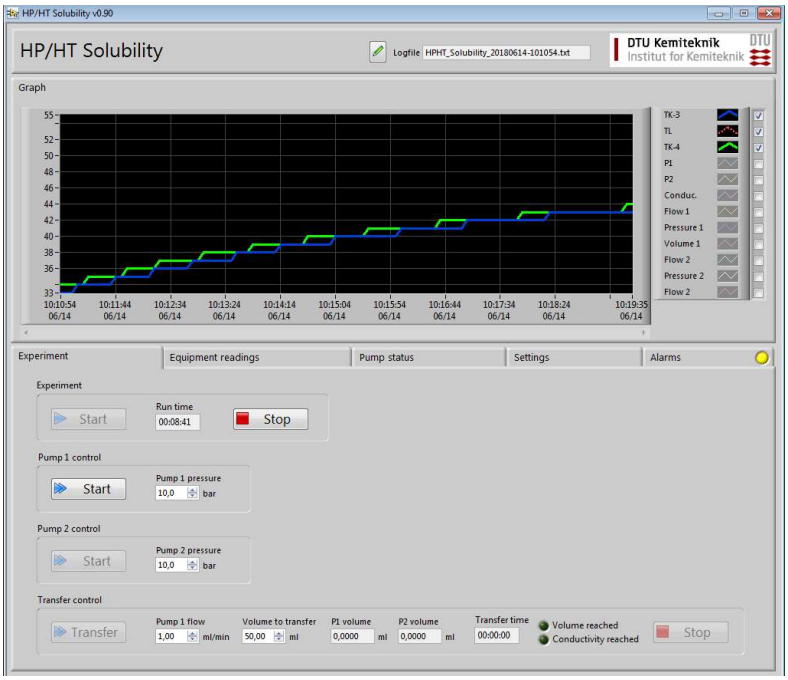

Figure 5.3 Interface for controlling the experimental unit: HT Titanium Cell Software

5.4.3 Time Required to Attain Equilibrium

One of the key aspects for measuring solubility is to ensure that the solid and the aqueous phase are in equilibrium. During the time required to reach the equilibrium conditions it is important to keep the experimental conditions steady. Thus, the Equilibration cell is monitored continuously to ensure constant conditions e.g. temperature and pressure. It is crucial to check the volume of the ISCO Pump to avoid any overpressure in the pump. If this happens the pump stops automatically. If the Equilibration cell is over pressured the relief valve will open when a pressure of 65 bars is reached. If any of those events happen the experiment is no longer carried out at constant conditions. The software will notify any problem on the ISCO Pump at the "Pump Status" tab.

In order to determine if the equilibrium conditions have been achieved a sample has to be withdrawn from the equilibration time at certain intervals of time. The sampling is done at constant temperature and pressure to avoid precipitation of the solid. The procedure is described as follows.

5.4.4 Sampling

The steps described in Section 5.4.1 and 5.4.2 in this Chapter are repeated with the Dilution Cell (TK-4 in Figure 5.1). The dilution cell is only loaded with previously degassed ultrapure water. To avoid

the presence of solid particles in the dilution cell the stirrer in the Equilibration Cell (TK3 in Figure 5.1) must be switched off during sampling. First the heating system for the transfer line is turned on and the process temperature is set. The transfer line must be insulated to guarantee a constant temperature and to prevent any accident. To initialize the sampling the "Transfer control" option in software is employed. The ISCO PUMP (C-2 in Figure 5.1) is set to constant flow rate mode from the control panel. A value of 1 mL/min is set to avoid any abrupt changes in pressure. An aliquot of e.g. 50 mL is set as the volume to transfer in the control panel. To start up the transfer the "Transfer" button Figure 5.3 is pressed.

The valve (V-3 in Figure 5.1) in the transfer line is open manually. The second valve (V-4 in Figure 5.1) at the transfer line is open when the pressure in the Equilibration Cell is constant. When the volume to transfer is reached the software will set the ISCO Pump (C-2 Figure 5.1) back to constant pressure mode. Then it is important to close immediately valves V-3 and V-4 in the transfer line.

The transfer line is equipped with a conductivity probe. During the transfer the green light (Figure 5.2h) must be on, indicating that the aqueous solution is in the line. Otherwise if silicon oil is present in the line, the probe will show a low conductivity value and the red light (Figure 5.2i) will indicate it. If silicone oil is present in the line the sample must be discarded.

Then the heating system and the pressure control of the dilution cell are switched off. A sample is taken from the cell opening the valve (V-5 Figure 5.1). A set of minimum 3 samples is taken since significant variation in the concentration of Zn and Na were observed in some cases between samples.

The procedure described above is repeated until no significant variations in Zn concentration are observed.

5.5 Results and discussion

The experimental solubility data for ZnS at temperatures between 95 °C and 175 °C and pressures up to 50 bars are presented in this section. In addition, the reliability of the analytical technique and sampling method is discussed. The results shown in this chapter are based on the knowledge gathered from the measurements at lower temperatures presented in Chapter 3.

5.5.1 Equilibration time

It is assumed that the equilibration time for the ZnS at temperatures between 95 °C and 175 °C is 3 days. This assumption is based on the results obtained at temperatures up to 80 °C. In Chapter 3 is shown how the equilibration time decreases with the increase of temperature, i.e. the equilibration time at 40 °C was 10 days while at 80 °C was 3 days. Increase of pressure also leads to shorter equilibration time, though the effect of pressure is less significant on the solubility. Thus, it is expected that at the investigated experimental conditions, equilibrium is reached in less than 3 days.

5.5.2 Effect of temperature on ZnS solubility

The effect of temperature on solubility of aqueous ZnS is presented in this section. The results are reported as zinc concentration and total sulphur, i.e. the concentration of sulphur in all existing species such as $H_2S_{(aq)}$, HS^- and S^{2-}.

The experimental Zn respectively total sulphur equilibrium concentrations as function of temperature are summarized in in Figure 5.4 as molality *b* (mol·kg·water^{-1}). The values presented in this figure are the average of 3 measurements. These data were obtained at saturation pressure of water and 3 days of equilibration, i.e. the experiment run 3 days without any disturbance before the samples were taken.

As reported initially for solubility measurements at temperatures up to 80 °C the concentration of Zn and total sulfur increases as temperatures raises. This expected behaviour is shown in Figure 5.4 and was also noticed for other systems, such as PbS and FeS (see Chapter 4). Figure 5.4 substantiates that the effect of temperature on the Zn equilibrium concentration is greater at temperature below 95 °C. While an increase of 12 times was observed from 40 °C to 95 °C just an increase of 1.5 times is observed from 95 °C to 175 °C. Figure 5.4 also shows that the total sulfur concetration increases roughly linear as function of temperature. The values at 95 °C and 135 °C seem to deviate from the linear behavior. Most probably these are outliers, however additional measurements are necessay to confirm.

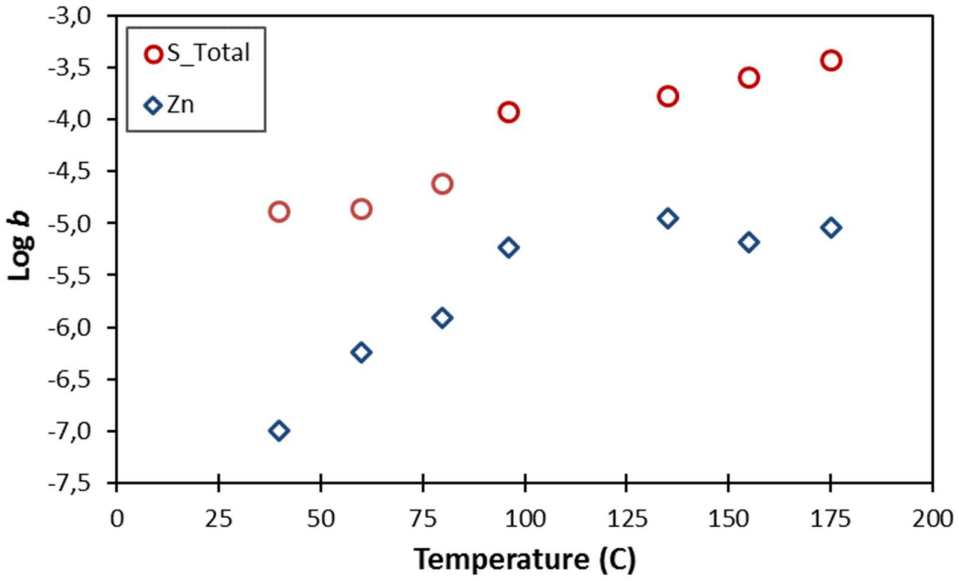

Figure 5.4 Solubility of ZnS vs temperature at the saturation pressure of water

The values presented in Figure 5.4 are the average of 3 measuements. The absolute average deviation is 11% for the Zn concentration respectively 5% for total sulfur concentration. The measurements at 135 °C show the largest deviation (16%) and this may explain the deviation of the concentration observed at 135 °C.

Furthermore, Figure 5.4 outlies that there is a ratio of approximately 1:10 between the concetration of Zn and total sulfur. A molar ratio of 1:1 is expected assuming that the dominant aqueous species are Zn and S. However, the experiments suggests that other species may bepresent in the aqueous solution such as complexes i.e. Zinc Bisulfide Complex $Zn(HS)_3^-$ [10].

In some of the experiments at 175 °C and 50 bar, the solid and the aqueous phase turned red color. The first hypothesis was due to corrosion of the cell or valves made of stainless steel. But after a visual inspection of the apparatus no evidence of corrosion was found. Another hypothesis was the presence of Fe in the structure of the ZnS. Although no evidence of Fe in the structure of ZnS was found when the solid was analyzed by SEM (see Chapter 3). It has been reported by Scott [11] that ZnS might change color (especially at high temperatures e.g. 200 °C) when the metal to sulfur ratio is less than one and obtained under highly sulfidizing conditions. The process for obtention of the ZnS provided by Sigma-Aldrich is unknown. This may explain the large differences found between Zn and S concentrations for all the experiments conducted in this study. As stated in Chapter 3, the SEM analysis was intended to confirm Zn and S as major components rather than reporting the exact

composition of ZnS. Other spectroscopic technique such as X-ray photoelectron spectroscopy (XPS) are required for the analysis of the starting material to determine its exact composition and therefore to confirm the hypothesis that the starting material is metal-deficient.

5.5.3 Effect of pressure on ZnS solubility

The effect of pressure of ZnS solubility was investigated as well. Pressure is the other important parameter that changes during production of oil. Thus, understanding the effect of pressure on solubility is important for avoiding scaling. Though the effect of pressure on solubility is not as remarkable as the effect of temperature [12]

For this reason, experiments were conducted at different pressures: atmospheric pressure for experiments between 40 °C up to 80 °C, above saturation pressure for experiments between 95 °C up to 175 °C and 15 bars to 50 bars. The pressure values for the experiments carried out above the saturation pressure are presented in Table 5.1. Three samples are withdrawn for analysis at each experimental condition (P and T). The results are plotted in Figure 5.5. The data points within a standard deviation from the mean are averaged and presented in Table 5.1. Data points beyond those limits are discarded.

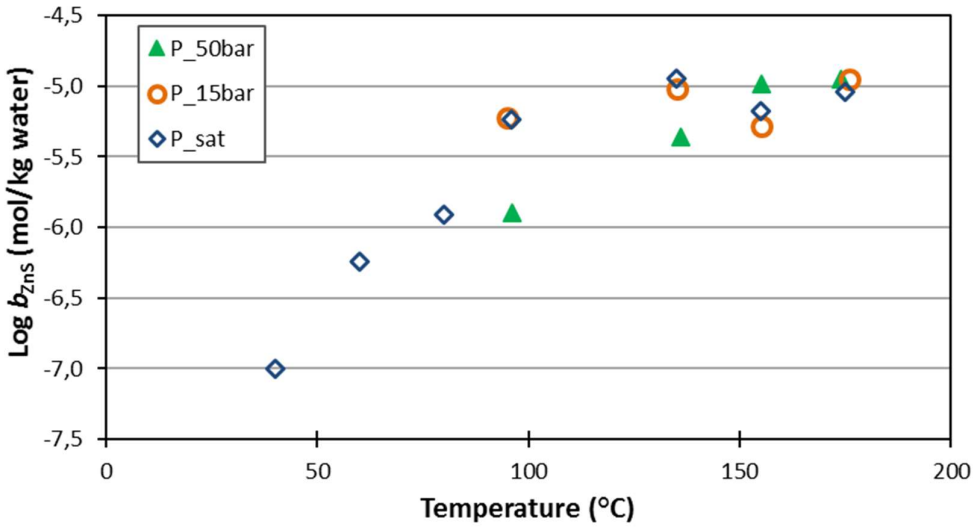

Figure 5.5 Solubility of ZnS as function of temperature at different pressures

Table 5.1 Solubility data at temperatures between 95 °C and 175 °C

P (bar)	Temp. (˚C)	Zn concentration [mol/kg H_2O] x 10^8	Data points	S total concentration [mol/kg H_2O] x 10^6	Data points
2,4	95	588,40 ± 81,8	3	117,80 ± 8,0	3
4,7	135	1149,00 ± 179,5	3	170,05 ± 1,6	3
6,5	155	664,49 ± 14,5	3	252,12 ± 3,0	3
10,3	175	913,60 ± 132,3	3	346,37 ± 0,8	2
15,1 ± 0,3	96	552,68 ± 59,1	3	5,53 ± 0,6	2
	135	950,01 ± 56,0	3	9,50 ± 0,6	3
	155	467,55 ± 74,6	3	4,68 ± 0,7	3
	175	1110,22 ± 32,1	3	11,10 ± 0,3	3
50,3 ± 0,2	96	126,12 ± 6,1	2	133,31 ± 0,1	3
	136	435,73 ± 6,7	2	121,22 ± 0,1	3
	155	1035,70 ± 4,0	2	204,26 ± 0,0	2
	175	1122,46 ± 18,4	3	242,78 ± 0,2	3

No influence of pressure was observed in the range of pressures explored in this study (up to 50 bars) on ZnS solubility (see Figure 5.5). The difference between the Zn equilibrium concentration at different pressures for a fixed temperature is negligible. The small differences between the data for a given temperature is in the range of the experimental error, most probably due to sampling procedure. The dilution determination might propagate errors as the volume transferred from the Equilibrium Cell to the Dilution Cell depends on the accuracy of the determination of the NaCl concentration. The error estimated for the Na concentration ranged between -3% and 4%.

The results obtained in this study are compared to published solubility data. Figure 5.6 shows the obtained experimental data: (1) at water saturation pressure (points marked with red circles), (2) at 15 bar and 0.1 molal NaCl brine solution (purple hollow circles), (3) at 50 and 0.1 molal NaCl brine solution bar respectively (green hollow circles). These data are comparable to values obtained by other researchers.

For example, Barnes [6] measured the solubility of ZnS at 6.8 and 34 bar but at different temperatures (25 °C respectively 100 °C). For this reason, the influence of pressure on the solubility values cannot be analysed. Figure 5.6 shows that generally these values are greater than the values obtained by other studies repsectively data produced at Technical University of Denmark (this study).

The results of this study are also compared to the data by Relly [4]. Relly [4] measured the solubility of ZnS at a very high pressure (275 to 345 bar) using radioactive ZnS. These solubility data are

comparable with the data by Barnes [6] but they are generally much greater than the values from previous studies. As noted by Relly [4], the measurements are doubtful as the radiation of the sample was not strong enough.

Unfortunately the pressure conditions of the experiments conducted by Ellis [13] are not specified but it is observed that there is no significant variation between data. Note that these data were obtained at temperatures between 194 °C and 300 °C. One can see in Figure 6 that Ellis' data follows the trend of the datapoints of this study, i.e. above 95 °C nor the temperature, nor the pressure influences significantly the solubility of ZnS. In summary, the data of Ellis sugest that temperature or pressure does not influence the solubility of ZnS at temperatures above 95 °C.

The solubility measurements conducted by Vukotic [14] were carried out at water vapor pressure. Similar to Ellis' data, the data published by Vukotic are in agreement with this study. Although the data obtained in this study at temperatures above 80 °C differ from the data reported by Vukotic, those discrepancies can be explained by the presence of NaCl (0.1 m NaCl) in the data published in this study. This effect of NaCl on the solubility was studied by Barret and Anderson [15]. It was concluded that under the experimental conditions explored (3-5 m NaCl) ZnS was more soluble as NaCl concentration increased.

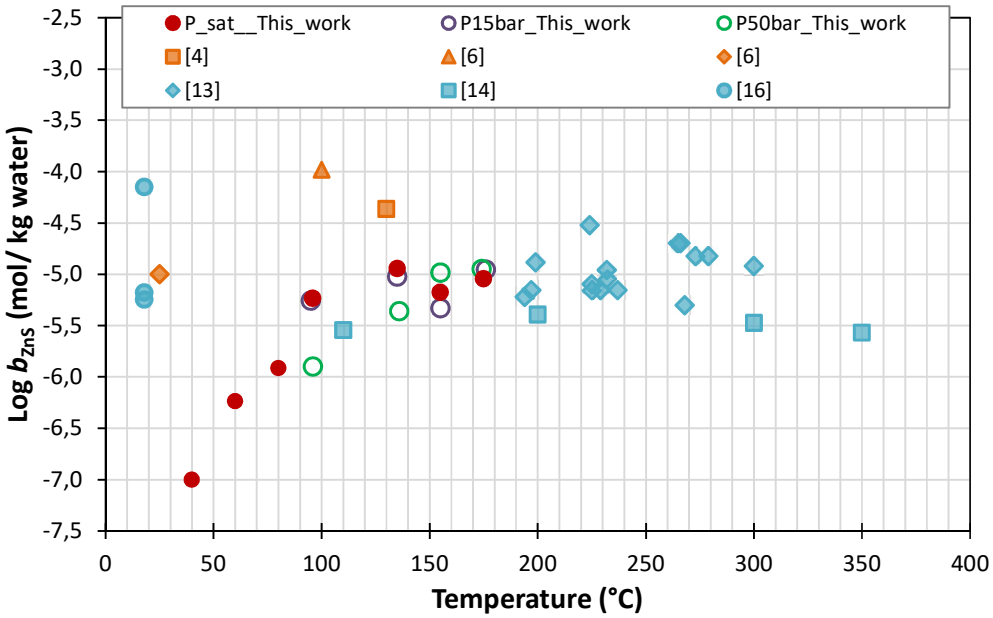

Figure 5.6 Solubility of ZnS vs temperature. Relly [4] at 275-345 bar (pressure range is presented since it is not certain the value at which the experiments were run); Barnes [6] at 6.8 bar (diamond marker) and at 34 bar (triangle marker); Ellis [13]; Vukotic [14] and Weigel [16]

In conclusion, Figure 5.6 outlines that data of this study are in between the data published for ZnS solubility at high pressures (up to 50 bars) and high temperatures (up to 175 °C). This is confirmed by other authors at temperatures up to 350 °C. Thus, from the solubility data presented in Figure 5.6 it can be concluded that pressure does not influence significantly the ZnS solubility at temperatures ranging from 25 °C to 350 °C.

5.5.4 Reliability of the analytical technique and sampling method

The reliability of the analytical technique and sampling method is presented in this section. Evaluation of interferences from external factors such as the construction material of the cell is needed to assess the reliability and accuracy of the data, especially when measuring solubility of trace elements, i.e. Zn and S in aqueous solution. In addition, quantifying the accuracy of the sampling method is also necessary as it is one of the main sources of error in previous studies.

5.5.4.1 Analytical Technique

Interferences of elements such as Titanium (Ti) from the construction material of the cell on the determination of Zn concentration using the ICP-OES were tested. Other elements found in the material of the cell, such as Aluminium (Al), Vanadium (V), Nickel (Ni) and Iron (Fe) were also

included in the study. The purpose of this measurements is to test the interference of these elements in the matrix of the sample in the Zn measurements.

To quantify these interferences, initially the concentration of the elements mentioned above was determined in a set of blank samples. Afterwards, the concentration of the elements was measured in the ultra-pure and in water stored in the cell. Finally, the calibration of the ICP-OES was conducted using the ultra-pure water and the water stored in the cell.

The ICP-EOS measurements revealed that interferences of Titanium, Vanadium, Nickel respectively Iron are insignificant. Only the concertation of Aluminium was between the detection limits of the ICP-OES.

Table 5.2 Concentration of potential interfering elements

	Al **[mol/kg water]x10^7**
Ultra-pure Water	2.7
HT Cell	7.3

The relative error between the aluminium standard solution and the aluminium measured by the ICP-OES was 14%. This difference between the concentration from the two sources of aluminium is significant. However, the aluminium concentration is negligible compared to the concentration of Zinc and therefore it can be assumed that the interaction between the elements is low (insignificant) during the solubility experiments.

The results using two different matrices for the ICP-OES calibration are presented in Table 5.3. Table 5.3 shows the average error when measuring the concentration of Zn of a standard solution using ultra-pure and water stored in the HT Cell as matrices for ICP-OES calibration. The error values show that there is more deviation from the real concentration when the water from the cell is used as matrix. Therefore, the calibration of the ICP-OES for the results shown in the previous section was done using ultra-pure water.

Table 5.3 Calibration test for the ICP-OES

	Error %	
	Ultra-pure water Calibration	**HT Cell water Calibration.**
Low concentration range	4.7%	18.8%
High concentration range	4.7%	19.3%

5.5.4.2 Sampling method

The sampling method for withdrawing an aliquot from the Equilibration Cell to the Dilution Cell presented some challenges. First, the volume measured by the ISCO pumps is not a reliable value. The value for the volume transferred differs in between runs, though the set value was always 50 mL. The variations may be due to changes in temperature or pressure, or differences in the dead volume of the set-up. For that reason, the transferred volume showed by the ISCO Pump was not consider for calculations. Instead, NaCl was used as a tracer. The aqueous solution in the Equilibrium Cell has a concentration of 0.1 M. An aliquot (approximately 50 mL) of the aqueous solution is transferred to the Dilution Cell. Then a sample is extracted from the Dilution Cell and the concentration of Na is checked by ICP-OES analysis. The volume transferred then is calculated using the two known values of Na concentration. The calculation of the volume transferred may carry errors propagated during the experimental work. For example, uncertainties related to weighting of the NaCl and water. Furthermore, the relative error of the concentration of Na determined by ICP-OES was 1.88%.

5.6 Conclusions

An experimental set-up has been designed and manufactured intended for measuring the solubility of sparingly soluble salts. The HT Titanium Cell has been constructed entirely of Titanium to avoid corrosion of the equipment and therefore contamination of the samples. The cell is equipped with temperature, pressure and conductivity probes which facilitate the traceability of the experiments. The versatile design allowed to carry out measurements at high temperatures (up to 175 °C) and elevated pressures (60 bar) with little monitoring of the experiments as the cell is equipped with pressure safety valves and temperature controllers.

One of the challenges identified for determination of solubility at elevated temperatures and pressures is the extraction of a sample at experimental pressure and temperature. This challenge was addressed by installing a transferring line between the two tanks of the equipment. Then the sampling process

takes place at the same experimental conditions. Additionally, the instant dilution of the sample prevents back-reactions.

The results obtained for ZnS solubility are comparable to the results obtained at temperatures between 40 °C– 80 °C. The solubility data obtained at temperatures between 95 °C and 175 °C increase with temperature, the solubility value is double when the temperature is raised 40 °C. However, the increase is lower than at temperatures between 40 °C and 80 °C. The solubility values obtained are comparable with data obtained by other authors. It is important to mention that previously published data differ in terms either in experimental conditions or solid starting material. Though in some cases the comparison is made just for descriptive purposes.

Unfortunately, the experiments carried out at different pressures did not show any effect of the pressure on the solubility values. This may indicate that there is no influence of pressure in the range studied. The solubility data published by different authors that were included in this study do not show a clear effect of the pressure on the solubility of ZnS either. Inaccuracies in the experimental method may hinder the effect of pressure as well. The procedure for sampling using NaCl as tracer needs to be validated. The propagation of the error on the calculation of the dilution rate can affect and results in erroneous determination of the solubility of ZnS. Another reason may be the presence of fine particles as the cartridge employed for filtration only retains 70% of the fine particles.

References

[1] W. Voigt, Chemistry of salts in aqueous solutions: Applications, experiments, and theory, Pure Appl. Chem. 83 (2011) 1015–1030.

[2] R. Cohen-Adad, J.W. Lorimer, M. Salomon, INTRODUCTION TO THE SOLUBILITY OF SOLIDS IN LIQUIDS, in: Alkali Met. Ammonium Chlorides Water Heavy Water (Binary Syst., Elsevier, 1991: pp. xxii–xxx.

[3] C. Yan, P. Guraieb, R.C. Tomson, Solubility Study of Iron Sulfide FeS Under Extremely High Temperature Pressure in Strictly Anoxic, Various Ionic Strength Solutions, in: SPE Int. Oilf. Scale Conf. Exhib., Society of Petroleum Engineers, 2016.

[4] B.H. Relly, A method for determining solubility at high temperatures and pressures, Econ. Geol. 54 (1959) 1496–1505.

[5] B.R. Tagirov, O.M. Suleimenov, T.M. Seward, Zinc complexation in aqueous sulfide solutions: Determination of the stoichiometry and stability of complexes via ZnS(cr) solubility measurements at 100 °C and 150 bars, Geochim. Cosmochim. Acta. 71 (2007) 4942–4953. doi:10.1016/j.gca.2007.08.012.

[6] H.. Barnes, Ore Solutions, 57th ed., Carnegie Institute of Washington, 1958.

[7] J.J. Hemley, G.L. Cygan, J.B. Fein, G.R. Robinson, W.M. d'Angelo, Hydrothermal ore-forming processes in the light of studies in rock-buffered systems; I, Iron-copper-zinc-lead sulfide solubility relations, Econ. Geol. 87 (1992) 1–22.

[8] H.L. Barnes, Ore solution chemistry;[Part] 1, Experimental determination of mineral solubilities, Econ. Geol. 58 (1963) 1054–1060.

[9] P. Guraieb, J. Huang, C. Yan, E. Contreras, M. Tomson, R. Tomson, Validation of the Activity Coefficients for Carbonates at Various High Pressure High Temperature (HPHT) and Total Dissolved Solids (TDS), (2014).

[10] H.L. Barnes, Sphalerite solubility in ore solutions of the Illinois-Wisconsin district: ECON, GEOL. MON. 8 (1967) 826–882.

[11] S.D.B.H.. Scott, Sphalerite-wurtzite equilibria and stoichiometry, Geochim. Cosmochim. Acta. 86 (1972) 1275–1295.

[12] R.P.. Hefter, G.T; Tomkins, ed., The Experimental Determination of Solubilities, John Wiley

& Sons, 2003.

[13] A.J. Ellis, The solubility of zinc sulfide in water at high temperatures, Econ. Geol. 54 (1959) 1035–1039.

[14] S. Vukotic, Contribution to the study of the solubility of galena, of sphalerite, and of chalcopyrite in water in the presence of hydrogen sulfide between 50 and 200 C, Bull. Bur. Rech. Geol. Min. (1961) 11–27.

[15] T.J. Barrett, G.M. Anderson, The solubility of sphalerite and galena in NaCl brines, Econ. Geol. 77 (1982) 1923–1933.

[16] O. Weigel, The solubility of the sulphides of the heavy metals in water, Z. Phys. Chem. 58 (1907) 293–300.

CHAPTER 6

Solubility of $FeCO_3$

6.1 Introduction

Corrosion is a major problem for the oil industry as it is the main cause of significant production losses; equipment failures and costly shut downs. Minimizing the corrosion problem of the pipeline infrastructure will reduce costs on equipment failures and it will minimize production loss. One of the methods to reduce the corrosion in pipelines is by controlling pH. Inducing a basic pH in the pipelines will promote the precipitation of corrosion products and as result, those products will create a barrier that prevents further corrosion of pipelines. Iron carbonate ($FeCO_3$) and iron sulfide (FeS) are corrosion products that when precipitated in the right amount at the right conditions, protect the pipeline infrastructure. In order to successfully control the pH in pipelines, the solubility of the corrosion products needs to be correctly determined as it is highly linked to corrosion rate. Therefore, understanding of the corrosion mechanism and determination of the precipitation rate of these products is of outmost importance. To understand the kinetics of corrosion formation, first the thermodynamics, i.e. solubility and speciation must be accurately described. This is needed as the precipitation rate depends directly on the solubility of the corrosion product [1]. The aim of this project is the study of the solubility of the corrosion products to determine the conditions at which the corrosion products create a protective layer that will prevent the corrosion of the pipelines.

Previous studies have shown the importance of solubility on the corrosion phenomena. The investigation carried out by Han and Carey [2] on localized corrosion on steel surfaces showed a significant reduction of the CO_2 corrosion rate on steel surfaces by $FeCO_3$ scale formation. This study consisted: (1) on the formation of a film of supersaturated $FeCO_3$ to protect steel from further CO_2 corrosion and (2) then a stainless-steel blade removed an area of the $FeCO_3$ film to initialize the localized corrosion. In both cases, the potentials were measured by a three-electrode electrochemical glass cell. In case of the surface coated with $FeCO_3$, the corrosion rate was estimated to 0.2 mm/year while the corrosion rate for the uncoated surface was 1.2 mm/year [2]. This means a reduction of 83% of the corrosion rate caused by CO_2 on steel surfaces. The reduction is directly attributed to the

formation of the $FeCO_3$ protective layer. Therefore, the solubility of $FeCO_3$ plays an important role. Furthermore, it is observed that at temperatures below 60 °C $FeCO_3$ does not form a protective layer as $FeCO_3$ is soluble in the aqueous phase. On the other hand, $FeCO_3$ precipitates at temperatures around 80 °C, consequently a protective film is formed [3]. This suggests that the solubility of $FeCO_3$ decreases as temperature rises. Therefore, high temperatures will favor the formation of a protective layer against corrosion.

The review presented by Fosbøl et al. [4] summarizes the studies on $FeCO_3$ solubility until 2002. Fosbøl et al. pointed out the uncertainties of the existing solubility data sets. Some of the major issues are related to the experimental procedure but also to the accuracy of the analytical method and the purity of the initial solid. For example, the lack of temperature control was observed in few studies which resulted in a low accuracy of the data. In other cases, it is not clear if the equilibrium conditions were achieved which may led to low reproducibility. Furthermore, Fosbøl et al. [4] highlighted that a large number of studies did not report vital information such as CO_2 pressure which makes those data unusable for thermodynamic modeling. The most relevant findings are summarized in the following section.

6.1.1 Previous studies on $FeCO_3$ solubility

Braun [5] determined the solubility product of $FeCO_3$ experimentally at temperatures between 30 and 80 °C. $FeCO_3$ was equilibrated with a buffer solution and degassed using high-purity nitrogen. The solution was placed in a thermostatic bath. Equilibration time was found to vary depending on pH. Iron (II) was analyzed in complexed form by adding 1,10-phenanthroline solution to $FeCO_3$ saturated solution. Then the iron concentration was determined spectrophotometrically at 508 nm. The solubility product was determined using only the data obtained at pH 7, due to complications observed at other pH values. It is pointed out by Braun [5] that iron II may be present in complex form with the buffer solution increasing the solubility of $FeCO_3$. The solubility product was found to decrease as function of temperature in the range studied (between 30 and 80 °C).

Greenberg and Tomson [6] measured the solubility of $FeCO_3$ at temperatures between 24 and 94 °C. A glass stirred reactor was used for their experiments. The concentration of total dissolved iron was determined by UV/vis spectrophotometer at 515 nm. The experiments were run at CO_2 partial pressure between 2.5 and 3 atm. Greenberg and Tomson informed about sampling periodically to monitor steady state conditions, but no information regarding the time required to reach a steady state

is provided. Similar to Braun [5], Greenberg and Tomson showed that the concentration of Fe concentration of iron decreases as temperature increases.

Silva [7] used a precipitated $FeCO_3$ obtained by reaction between ferrous sulfate heptahydrate and sodium bicarbonate. The solubility experiments were carried out in a Plexiglas vessel with temperature control and pH measurements using a combination electrode. The solubility measurements were carried out in NaCl solutions (0.1 and 5.5 molal) and at 25 °C. The solutions were prepared using deoxygenated water in a glove box. The concentration of iron was determined using the Ferrozine method. An important conclusion of this study is that $FeCO_3$ is more soluble at acidic pH values and the solubility is independent of ionic strength.

In more recent studies, Yan et al. [8] explored the solubility of $FeCO_3$ at higher temperatures (at 150 °C and 250 °C) and pressures (5534 – 23390 psig). Yan et al.[8] determined the solubility in 1 M NaCl solutions. At the end of each experiment, the precipitated $FeCO_3$ was analyzed and it was observed the presence of hematite (Fe_2O_3). The authors observed a decrease (0.5 logarithmic units) in solubility values as temperature raises. The presence of hematite shows that the experimental work was not carried out at anoxic conditions and therefore Fe was oxidized. Bénézeth et al. [9] determined the solubility of the mineral form of $FeCO_3$ (siderite) at temperatures between 25 °C and 250 °C. The solid phase was analyzed by XRD observing changes in the color of $FeCO_3$ from light grey to red suggesting oxidation. The XRD analysis showed the presence of goethite (FeO(OH)) and magnetite (Fe_3O_4). The changes of the solid form observed by Yan et a*l.* [8] and Bénézeth et al*.* [9] might lead to inaccurate solubility data determination.

Bruno et al. [10] measured the solubility of $FeCO_3$ (synthesized hydrothermally) at 25 °C in 1M $NaClO_4$ solutions at CO_2 partial pressures between 0.05 and 0.01 bar. Samples were taken after equilibrium was attained. The sample was filtered using a 0.05 mm pore size membrane and the concentration of iron was determined spectrophotometrically by using the ferrozine method. It was observed that the concentration of iron decreased as pH increased. This demonstrates that the solubility of $FeCO_3$ decreases when basicity increases.

The determination of equilibration time plays an important role in obtaining reliable solubility data. It is mentioned by different authors that the time required to reach equilibrium conditions varies with temperature and pH of the solution. It is observed from solubility data published that the equilibration time varies from few hours up to 7 months. Braun [5] showed that at pH 4 the concentration of Fe increased as a function of time. The study was carried out up to 7 months were equilibrium was

apparently achieved. For solutions at neutral pH it is determined that equilibrium is achieved within "several days". Note that equilibration time is shorter at high pH due to low equilibrium concentrations.

Silva et. al [7] and Bruno et. al [10] determined the equilibrium conditions by potentiometric measurements. It was decided that equilibrium was achieved when the value of the potential showed a variation less than 0.1 mV in 24 hours. The equilibration times ranged between 1 and 3 days. Furthermore, Ptacek and Reardon [11] investigated the solubility of siderite in NaCl and Na_2SO_4 solutions. They found out that equilibrium conditions were achieved after 4 weeks at 25 °C. In addition, Bénézeth et. al. [9] explored the effect of temperature on solubility and equilibration time. He determined that 3 to 5 days are required to reach equilibration conditions in the temperature range between 50 °C and 75 °C. The equilibration time is reduced to less than 24 hours at temperatures higher than 100 °C. It was determined that 18 days are necessary to reach equilibration conditions at 25 °C.

Yan et al. [8] used a flow-through apparatus to determine the solubility of siderite. The retention time in the pack column was between 35 and 181 minutes. The authors expressed that this retention time guarantees to reach equilibrium. There are not results shown regarding the variation of Fe^{2+} concentration with respect to retention time. These findings demonstrate that equilibration time must be determined before accurate solubility experiments can be performed as it depends on various factors, such as pH, temperature, raw material, etc.

6.1.2 Synthesis of Iron Carbonate ($FeCO_3$)

The synthesis of $FeCO_3$ is a key aspect for the analysis of the solubility of $FeCO_3$. $FeCO_3$ is not commercially available and therefore, it needs to be produced in-situ. The synthesis of $FeCO_3$ presents several challenges. The main challenge is the susceptibility of $FeCO_3$ to react with oxygen: $FeCO_3$ oxidizes to magnetite and hematite even in low oxygen environment. In most of the methods listed for $FeCO_3$ synthesis, presented by Fosbøl et al. [4] the procedure is carried out in a reduced oxygen atmosphere. $FeCO_3$ is obtained by precipitation using a source of iron (e.g. $FeSO_4$, $FeCl_2$ or FeC_2O_4) and a source of CO_2 ($NaHCO_3$, $NaCO_3$ or $CaCO_3$). This synthesis must be carried out at high temperatures as the reaction is favored at temperatures above 100 °C. The quality of the product varies depending on the process conditions such as anoxic conditions, the ratio between the iron and CO_2 source and the temperature. In several cases, $FeCO_3$ undergoes oxidation characterized by a red to brown color. The color of the precipitate indicates the purity of the obtained sample. For example,

several authors reported a variety of colors ranging from green, blue or black indicating low purity of the $FeCO_3$ obtained. The desired color of $FeCO_3$ is white but beige is also acceptable [4].

The US Patent #4657752 presented by Lyon [12] describes a process to produce high purity $FeCO_3$. According to this patent, the synthesis should be carried out in a closed vessel at temperatures between 100 °C to 300°. The reactants to produce $FeCO_3$ are a ferrous compound and alkali metal bicarbonate. The author suggests as ferrous compound: ferrous chloride ($FeCl_2$) and as alkali reactant: sodium bicarbonate ($NaHCO_3$). The suggested molar ratio of the reactants is between CO_2 source/Fe source of 3:1 to 10:1. In this manner, excess of CO_2 production is guaranteed, and this excess assures that the ferrous source is completely consumed by the reaction with CO_2. The solutions were prepared using distilled degassed water in an anoxic atmosphere. The recommended reaction time varies between 16 hours to 70 hours. The purity of the $FeCO_3$ was not tested but the crystal structure was confirmed by X-ray analysis. It is mentioned that the $FeCO_3$ obtained is stable when exposed to air[12].

The aim of this work is to contribute to the understanding of $FeCO_3$ precipitation as an aid to prevent corrosion. This work consists of two stages: (1) the synthesis of high purity $FeCO_3$ and (2) the solubility determination of $FeCO_3$ at temperatures between 25 °C and 80 °C in aqueous solutions. First, this study describes the experimental conditions and methodology for the synthesis of high purity $FeCO_3$ respectively the analysis of the obtained $FeCO_3$ solid. Then, this solid is used for solubility measurements between temperatures of 25 to 80 °C and in a strictly controlled experimental setup.

6.2 Experimental set-up

6.2.1 Synthesis of $FeCO_3$

The synthesis of FeCO3 was carried out at anoxic conditions in a sealed glove box (see Figure 6.1). Solutions of $FeCl_2 \cdot 4H_2O$ and Na_2CO_3/$NaHCO_3$ were prepared in the glove box using deionized water. The water was previously degassed using high purity N_2 (>99,999%). Each solution was loaded into a piston cylinder. These cylinders containing the solutions were previously purged to eliminate the gas present in the cylinder chamber. Then, the $FeCl_2 \cdot 4H_2O$ solution was pumped into the cylinder containing either Na_2CO_3 or $NaHCO_3$ solution using an ISCO pump.

Figure 6.1. Preparation of $FeCl_2 \cdot 4H_2O$ solution inside a glove box.

Afterwards the cylinder was pressurized and placed in a furnace at constant temperature (130 °C) for 24 hours. Then, the cylinder was cooled down using compressed air. Finally, the filtration of $FeCO_3$ was carried out in the glove box at anoxic conditions.

The $FeCO_3$ obtained was washed several times with deionized water previously degassed with nitrogen. Then, $FeCO_3$ was dried in a vacuum oven at 50 °C for 2 days (runs #1, #2 and #3). For run #4 $FeCO_3$ was dried in vacuum at room temperature for approximately 5 days.

6.2.2 Solubility measurement of $FeCO_3$

The experimental set-up and methodology used for solubility determination was described in detailed in Chapter 3. Here, only the steps specific for the solubility measurement of $FeCO_3$ are outlined FeCO3 was equilibrated with deionized water degassed with high-purity nitrogen. In order to investigate the importance of the purity of water on the reproducibility of the data, in some cases, the deionized water was distilled prior to degassing This additional distillation treatment helped to further reduce the amount of O_2 dissolved in the water. The sample was prepared at strictly anoxic conditions in a glove box. Note that the solubility of $FeCO_3$ was determined at temperatures between 25 °C and 80 °C.

6.3 Results and discussion

6.3.1 Synthesis of $FeCO_3$

This section presents the details of the $FeCO_3$ synthesis and suggest optimal operating conditions for obtaining high purity $FeCO_3$. The synthesis of $FeCO_3$ for this study was based on the studies published by Lyon [12] and Ptacek [13]. A summary of the most relevant investigatedexperimental conditions are summarized in Table 6.1. This table outlines the importance of key optimal reaction conditions such as elevated temperatures and excess of the CO_2 source.

Table 6.1 Experimental conditions for the synthesis of $FeCO_3$

Run	Fe source	CO_2 source	Fe /CO_2 (molar ratio)	Pressure (bar)	Temperature (°C)	$FeCO_3$ (s) (Color)
1	$FeCl_2 \cdot 4H_2O$	Na_2CO_3	1:1	10	25	Green-greyish/ Red-brown after drying
2	$FeCl_2 \cdot 4H_2O$	$NaHCO_3$	1:1	10	130	Tan/red after drying
3	$FeCl_2 \cdot 4H_2O$	$NaHCO_3$	1:4	10	130	Tan/red after drying
4 and 5	$FeCl_2 \cdot 4H_2O$	Na_2CO_3/ $NaHCO_3$	1:4	10	130	Beige

Table 6.1 shows that the color of the precipitate and therefore the purity of the product, strongly depends on the Fe/CO_2 molar ratio respectively the reaction temperature. Note that a white/beige $FeCO_3$ precipitate reflects a pure precipitate while the purity of the product decreases as the color turns to red-brown. For example, stoichiometric quantities of the iron and CO_2 sources were used in runs #1 and #2. It was observed in run#1 that the filtrate obtained changed its color from translucent to yellow over time. This suggests that $FeCl_2 \cdot 4H_2O$ did not react completely and the excess of $FeCl_2 \cdot 4H_2O$, which remained in the solution, oxidized in contact with air. The solid product obtained was initially green-grayish color. This color changed very fast, already before drying. After the drying process the solid turned red-brown color.

(a) (b) (c)

Figure 6.2 $FeCO_3$ precipitate obtained as a result of run #2, to #5 described in Table 6.1 Experimental conditions for the synthesis of $FeCO_3$: (a) – run #2, (b) – run #3 and (c) – run #4 and #5.

Run #2 was carried out using $NaHCO_3$ as CO_2 source. The molar ratio of $FeCl_2 \cdot 4H_2O$ and $NaHCO_3$ was 1:1. In this case the reaction temperature was 130 °C based on the findings from several publications [4,12,13]. Additionally, the reaction pressure was 10 bars to improve the CO_2 contact with the solution. The reaction was carried out for 24 hours. The product obtained had a tanned color. However, the change in color from tan to red was observed during the drying process. The change in color indicates the oxidation of the product obtained and it is doubtful that $FeCO_3$ was precipitated during Run #2.

The molar ratio (Fe source/CO_2) source used for Run #3 was 1:4. Increasing the amount of the CO_2 source guarantees an excess of CO_2 available during the reaction. The color of the product obtained in Run #3 was tan. The filtrate obtained was colorless and no change in color in contact with air was observed. The product changed its color during the drying process, from tan to red-brown color (Figure 6.2a). This suggests oxidation of the product obtained as traces of oxygen could have been present. The oxidation process might have been accelerated by the temperature of approximately 50 ˚C during the drying process. Probably a secondary reaction took place, such as the formation of $Fe(OH)_2$ instead of $FeCO_3$. Note that $Fe(OH)_2$ easily oxidizes in contact with air [12].

A mixture of Na_2CO_3/$NaHCO_3$ (1:1 molar ratio) was used as CO_2 source for run #4. The color of the product obtained after filtration was beige (see Figure 6.2c). Since it was observed in Run #3 that $FeCO_3$ oxidized during the drying process, the product obtained in Run #4 was dried at room temperature and at $6x10^{-1}$ mbars. No change in color was observed in this case. The crystal structure

of the product obtained in run #4 was analyzed by XRD and it was identified as $FeCO_3$. The spectrum from the XRD analysis is shown in Figure 6.3. The blue line (upper line) in Figure 6.3 corresponds to the characteristic spectrum of $FeCO_3$. The black line shows the spectrum obtained for the sample in run #4 and exhibits the characteristic peaks shown in the blue line. This figure demonstrated that the obtained product is very pure (>99.99%) and it is suitable for determination of $FeCO_3$ solubility in aqueous solution.

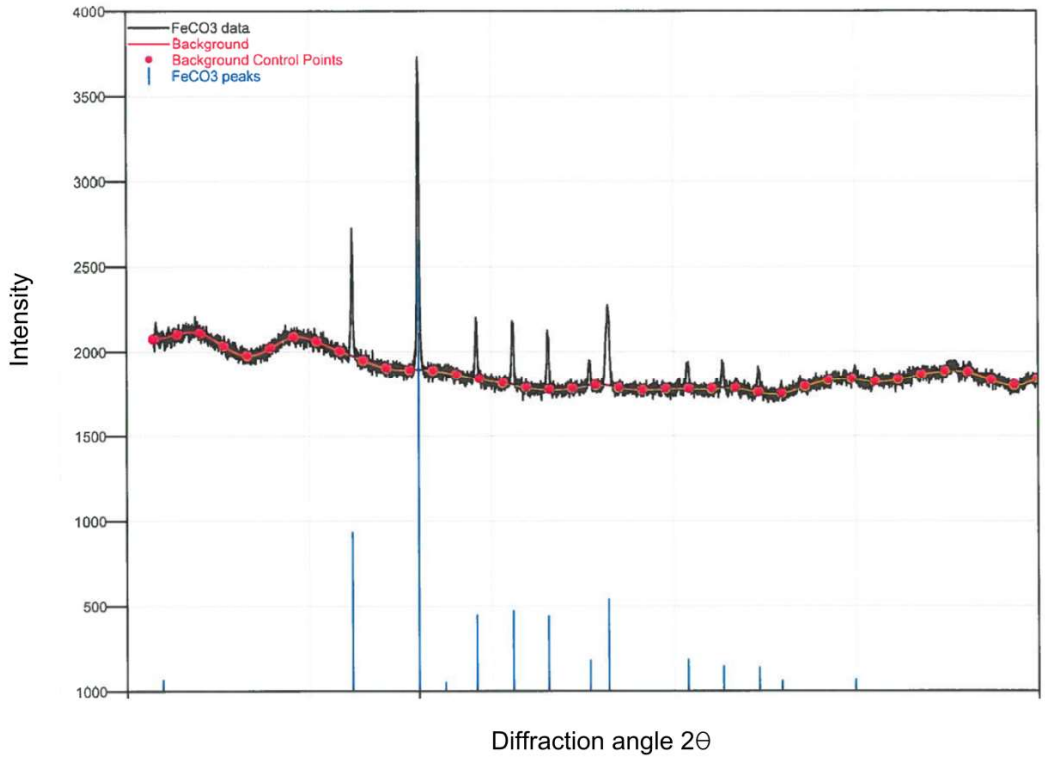

Figure 6.3 XRD spectrum of the product obtained in run #4. The crystal structure is identified as $FeCO_3$

Run #5 was performed at the same experimental conditions as Run #4, but the molar ratio Na_2CO_3/$NaHCO_3$ was 5:7. This run had an increased amount of $NaHCO_3$ compared to Run #4. The product obtained was beige $FeCO_3$ (Figure 6.2c) with no differences observed compared to the product obtained in Run #4.

The different colors described in Table 6.1 are due to different experimental conditions, incomplete reaction (in case of Run#1), formation of byproducts (Run #3) and/or oxidation of the final product due to poor oxygen removal. These results prove that it is important to assure a reduced oxygen conditions along the obtention of the product by using a glove box for (1) preparing of the sample,

(2) preparation of the reaction vessel and (3) also during filtration of the product. Furthermore, high purity $FeCO_3$ is obtained by using a mixture of Na_2CO_3 + $NaHCO_3$ as CO_2 source. This mixture assures excess of CO_2 compared to $FeCl_2$. Furthermore, oxidation of the sample can be minimized by drying at room temperature in an oxygen depleted environment.

6.3.2 Solubility determination of $FeCO_3$

Laboratory experiments were carried out to determine the solubility of $FeCO_3$ at temperatures between 25 °C and 80 °C. As mentioned in previous chapters, the solubility studies require the determination of the equilibration time prior solubility determination. Hence, the experiments to determine equilibrium conditions (no change in concentration) are presented first. Then, the effect of temperature on solubility is discussed.

6.3.2.1 Equilibration time determination

This section presents the experimental investigation of equilibration time of $FeCO_3$ at various temperatures. The determination of the equilibration time is crucial to determine the solubility of $FeCO_3$ accurately. The experimental methodology followed for these tests is described in Chapter 3. Note that we assume that all iron is present as iron ion (Fe^{2+}) as demonstrated by Bénézeth et al. [9] and Bruno et al. [10]. They showed that Fe^{2+} ion was the dominant iron species when studying the solubility of $FeCO_3$ at temperatures between 25 ˚C and 250 ˚C.

To understand how the concentration of the dissolved $FeCO_3$ changes in time and temperature, the iron concentration was measured between 1 and 7 days at temperatures between 25 ˚C and 80 ˚C. Figure 6.4 presents the results as concentration of iron versus time. The equilibration time can be determined from this figure, i.e. equilibration time corresponds to the plateau in the concentration versus time curve (see Figure 6.4). The analytical method employed for determination of iron concentration was Inductively Coupled Plasma Optical Emission Spectrometry (ICP-OES).

It is observed in Figure 6.4 that the concentration of iron continuously increases over time at 25 ˚C. Apparently equilibration conditions are not achieved in this time interval. This is in accordance with the work of Bénézeth et al. [9]. They suggested that more than 18 days may be required to reach steady state (equilibrium) conditions at 25 ˚C. Thus, additional work is needed to determine the equilibration time.

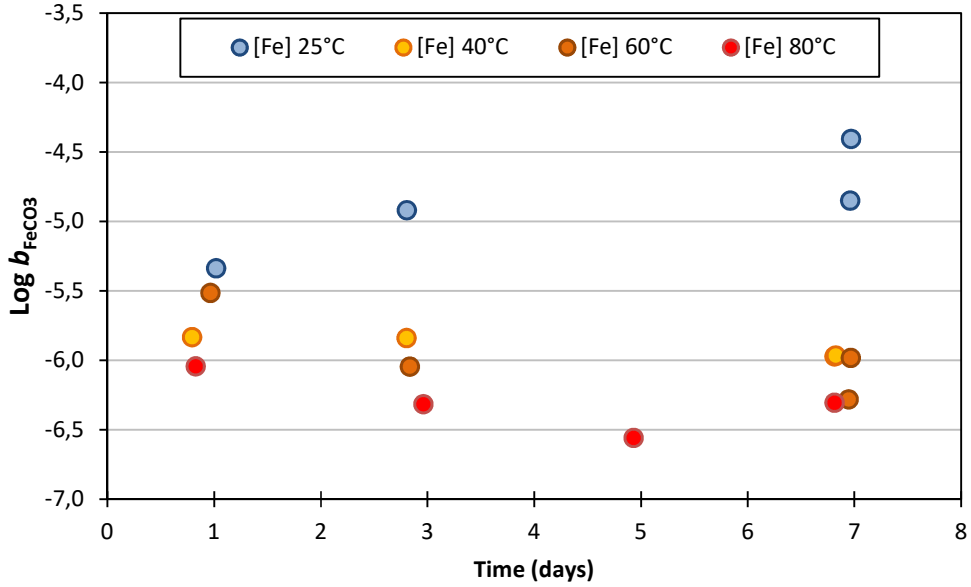

Figure 6.4 Equilibration time determination at temperatures between 25 °C and 80 °C.

The concentration of iron at temperatures between 40 ˚C and 80 ˚C shows an opposite trend compared to the behavior at 25 ˚C. The concentration of iron increases rapidly in a very short time (1 day) followed by a decline in concentration. This initial increase may correspond to the supersaturation before reaching equilibrium conditions [4]. There are no significant differences in the concentration of iron between 3 and 7 days. This suggests that equilibrium conditions are achieved between 3 and 7 days at temperatures from 40 ˚C to 80 ˚C. This agrees with the observations made by Bénézeth et al. [9]. Bénézeth et al. stated that 3 to 5 days are required to attain equilibrium conditions for the temperature interval between 50 °C and 75 °C [9].

These results demonstrate that equilibration time strongly depends on the temperature and it is apparently shorter at temperatures above 25 °C. The influence of temperature on iron concentration is clear at 3 days, i.e. at these conditions the concentration is lower as temperature rises. Moreover, this study confirms that at temperatures above 40 °C, 3 days seems of to be sufficient for reaching equilibrium between solid and liquid phases.

6.3.2.2 Effect of temperature on $FeCO_3$ solubility

The effect of temperature on the $FeCO_3$ solubility was also explored in this study. The temperatures considered were between 25 °C and 80 °C. The iron concentration at steady conditions as function of temperature are presented in Figure 6.5. This figure contains the experimental values obtained after

3 days of equilibration time. The previous section showed that 3 days are sufficient for achieving equilibrium conditions.

Figure 6.5 shows the iron concentration at equilibrium condition with respect to temperature. In this figure the experimental data obtained is compared to available data from the open literature. Figure 6.5 illustrates that the solubility of $FeCO_3$ decreases as temperature increases. The solubility is 24 times higher at 25 °C compared to 80 °C.

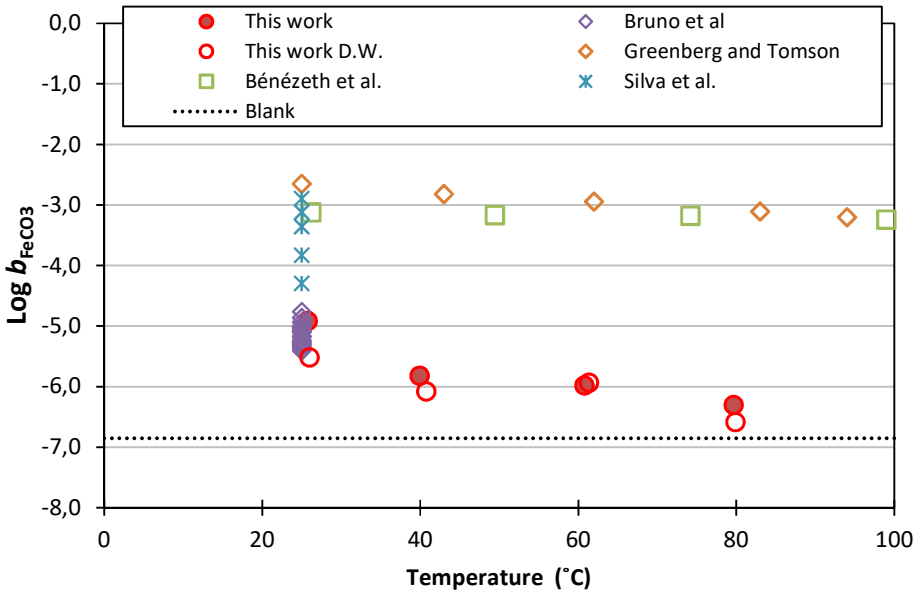

Figure 6.5 Iron concentration at equilibrium conditions vs temperature. Solubility data obtained using distilled Milli-Q water (DW) (hollow red dots), Bénézeth et al. [9] (NaCl 0.1M and pH between 4- 6); Bruno et al. [10] (pCO_2 0.05 - 0.1 atm and pH 7.4 - 8.9) Greenberg and Tomson [14] (pCO_2 2.4 – 3.0 atm) Silva et al. [7] (pCO_2 0.05 atm, NaCl 0.1 pH 5.7 – 6.3).

It has been observed that the color of the sample (obtained $FeCO_3$ solid) changed during the solubility analysis of the sample (see Figure 6.6). To understand this phenomenon, additional solubility experiments were carried out. It is important to mention that this change in color it is partly attributed to poor removal of oxygen during sample preparation. This issue was addressed by distilling Milli-Q water (used as solvent) using a roto-evaporator and further degassing the distilled water with high purity nitrogen. These results correspond to the hollow red dots in Figure 6.5. No significant differences are observed at temperatures between 40 °C and 80 °C. The largest change in concentration was obtained at 25 °C, a reduction of 71% on iron solubility when using distilled Milli-Q water.

Figure 6.6 Change of color of $FeCO_3$ after solubility analysis

The solubility data for $FeCO_3$ obtained in this study are also compared to published data in Figure 6.5. The data published in open literature are characterized by large scattering. The scatter is mainly due to different experimental conditions such as variations of the pH, partial pressure of CO_2 (pCO_2) and presence of NaCl that ultimately impacts on the speciation scheme and therefore on the solubility values. This is outlined by the data presented by Bénézeth et al. [9] and Greenberg and Tomson [6] which are almost 1000 times higher than the experimental data produced. In the case of Bénézeth et al., the experiments were carried out at slightly acidic conditions (pH 4 – 6) at which the solubility of $FeCO_3$ is expectedly higher. Greenberg and Tomson measured the $FeCO_3$ solubility at CO_2 partial pressures between 2.4 and 3.0 atm. Higher pressure favors the solubility of CO_2 aqueous and ultimately impacts on the pH of the solution. This leads to a more acidic solution compared to a zero CO_2 (or very low) partial pressure.

In the range of temperatures studied here, between 25 °C and 80 °C, a decrease in the concentration is observed in the data published by Greenberg and Tomson [6]. This finding agrees with this study. The data published by Bénézeth et al. [9] show that the concentration of Fe at equilibrium conditions is independent of temperature. This might be due to a significant change in the pH, (between 4 and 6) and acidity of the solution as mentioned above. The data published at 25 °C by Silva et al. [7] show high scattering as a consequence of some experiments carried out in presence of NaCl in the solution or at acidic pH.

Bruno et. al [10] measured the solubility of $FeCO_3$ at 25 °C at 1 atm and relatively low partial pressures of CO_2 compared to other studies mentioned here (e.g. Bénézeth et al. [9] and Greenberg and Tomson [14]). The results obtained by Bruno et. al [10] are comparable to the results obtained here at 25 °C. It is worth to mention that the experiments performed in this study are free drift, meaning that there is no control for pH during experiments (no addition of buffer solutions) neither the pH of the solution was set. Although the pH of the solutions was not measured; we expect that the pH of the solution will be around neutral values, having in mind the low concentrations of the species dissolved. In this matter, the data at pH values between 7 and 8 presented by Bruno et al. [10] are in agreement with the data at 25 °C presented in this study.

To determine whether there was contamination of the samples with a source of iron different from $FeCO_3$, measurements of the iron content of a blank sample were taken using the ICP-OES analytical technique. The results are represented in Figure 6.5 by a dotted line. The iron content of the blank sample was determined in the same manner as the experimental procedure described for the solubility analysis of $FeCO_3$. This figure demonstrates that the concentration of iron present in the blank sample is insignificant respect to the Fe concentration from the $FeCO_3$ solubility analysis, i.e. the experimental results are not biased by impurities from the solvent. The experimental error of the measurements was determined using a standard solution of iron. The concentration of iron was measured using the ICP-OES. The experimental error was determined to vary between 6.5% to 7.7%.

6.4 Conclusions

The solubility of $FeCO_3$ in water at temperatures between 25 °C and 80 °C and at atmospheric pressure was studied. The methodology used for preparing the sample and performing the solubility measurements has been adjusted for the $FeCO_3$ system to achieve reliable results and to avoid potential pitfalls, such as presence of impurities in the sample, oxidation of the sample, etc. Furthermore, various factors have been studied for the synthesis of high purity $FeCO_3$, necessary to prepare aqueous samples for solubility analysis.

This study showed the changes in the iron concentration as function of time, i.e. the iron concentration of the sample has been measured after 1 day to 7 days of equilibration to determine the equilibration time (the time needed to reach steady state conditions). Additionally, the influence of the temperature on the solubility was explored. The main conclusions of this study are:

- The iron concentration with respect to time at 25 °C did not reach a plateau in 7 days. This suggests that the equilibrium conditions were not achieved in 7 days. On the other hand, at temperatures between 40 °C and 80 °C the time required to achieve equilibrium conditions occurs between 3 and 7 days.
- A weak influence of the temperature on FeCO3 solubility was observed. The iron concentration at equilibrium conditions at 25 °C is approximately 3.5 times higher than the concentration observed at 80 °C. It is also noteworthy that the solubility of FeCO3 decreases as temperature increases.

The synthesis of the $FeCO_3$ in-situ for solubility experiments was needed as $FeCO_3$ is not available commercially. Five different experimental conditions were explored to obtain $FeCO_3$. It was concluded that high temperatures (around 130 °C) favor the formation of $FeCO_3$. The iron source/carbonate source molar ratio has a high impact on the obtention of $FeCO_3$. It was found that at a molar ratio of 1:4 (Fe source/CO_2 source), the product of the synthesis obtained correspond to the crystal structure of $FeCO_3$.

References

[1] W. Sun, S. Nešić, R.C. Woollam, The effect of temperature and ionic strength on iron carbonate (FeCO 3) solubility limit, Corros. Sci. 51 (2009) 1273–1276.

[2] J. Han, J. William Carey, Localized CO2 corrosion propagation at moderate FeCO3 supersaturation initiated by mechanical removal of corrosion scale, J. Appl. Electrochem. 41 (2011) 1367–1371. doi:10.1007/s10800-011-0337-5.

[3] G. Schmitt, M. Horstemeier, Fundamental aspects of CO2 metal loss corrosion-Part II: Influence of different parameters on CO2 corrosion mechanisms, in: Corros. 2006, NACE International, 2006.

[4] P.L. Fosbøl, K. Thomsen, E.H. Stenby, Review and recommended thermodynamic properties of FeCO3, Corros. Eng. Sci. Technol. 45 (2010) 115–135. doi:10.1179/174327808X286437.

[5] R.D. Braun, Solubility of iron (II) carbonate at temperatures between 30 and 80, Talanta. 38 (1991) 205–211.

[6] J. Greenberg, M. Tomson, Precipitation and dissolution kinetics and equilibria of aqueous ferrous carbonate vs temperature, Appl. Geochemistry. 7 (1992) 185–190.

[7] C. Silva, X. Liu, F.J. Millero, Solubility of siderite (FeCO 3) in NaCl solutions, J. Solution Chem. 31 (2002) 97–108.

[8] C. Yan, P. Guraieb, J. Huang, R.C. Tomson, Study of Siderite Solubility under Extreme High Temperature and Pressure in 1 M NaCl Solution, in: Corros. 2015, NACE International, 2015.

[9] P. Bénézeth, J.L. Dandurand, J.C. Harrichoury, Solubility product of siderite (FeCO 3) as a function of temperature (25–250 C), Chem. Geol. 265 (2009) 3–12.

[10] J. Bruno, P. Wersin, W. Stumm, On the influence of carbonate in mineral dissolution: II. The solubility of FeCO3 (s) at 25 C and 1 atm total pressure, Geochim. Cosmochim. Acta. 56 (1992) 1149–1155.

[11] C.J. Ptacek, E.J. Reardon, Solubility of siderite (FeCO3) in concentrated NaCl and Na2SO4 solutions at 25 C, in: Water-Rock Interact. Proc. Int. Symp., 7th, 1992: pp. 181–183.

[12] W.G. Lyon, Process for preparing ferrous carbonate, US Patent #4657752, 1987.

[13] C.J. Ptacek, Experimental determination of siderite solubility in high ionic-strength aqueous solutions, Waterloo, Ontario, Canada, 1992.

[14] J. Greenberg, M. Tomson, Precipitation and dissolution kinetics and equilibria of aqueous ferrous carbonate vs temperature, Appl. Geochemistry. 7 (1992) 185–190. doi:10.1016/0883-2927(92)90036-3.

CHAPTER 7

Modeling of Sulfide Scaling Materials:

Zinc, Iron and Lead Sulfide

7.1 Introduction

This chapter presents the thermodynamic calculations to represent the solid-liquid equilibrium of ZnS, FeS and PbS in aqueous solutions using the Extended UNIQUAC thermodynamic model. This model has been already used for the prediction of scaling materials such as $CaSO_4$, $BaSO_4$ and $SrSO_4$ at temperatures up to 300 °C and pressures up to 1000 bar showing promising results [1]. The focus of this study is to determine as few adjustable parameters as possible when fitting the model against the experimental data obtained. Note that it is not the intention of this study to reproduce and describe the Extended UNIQUAC model as the model is described in detail in the open literature [2].

There are only a few studies that present modeling results against experimental data for ZnS, FeS and PbS in aqueous solutions. However, thermodynamic models as well as experimental data are essential for studying and better understanding the behavior of these systems at various conditions. These models are also needed for mitigating the risk of scaling of pipelines, especially at high pressure and high temperature conditions. The vast majority of prediction studies are based on well-known models. For example, Saidoun et al. calculated the SLE for ZnS, FeS and PbS at temperatures up to 250 °C and pressures up to 1000 bar using the ScaleSoftPitzer developed by Rice University [3]. In a study, Okocha and Sorbie [4] presented a modelling approach that includes the speciation equilibrium reactions including seven (7) chemical species (i.e. H_2S, H^+, HS^-, S^{2-}, OH^-, Fe^{2+} and FeS). This approach uses the mass balance equations plus the charge balance equations. This system of equations is solved numerically by using the equilibrium constants from literature for each equilibrium reaction. The authors evaluate the performance of the model to their own experimental data. They claim the model represent exactly the experimental values for the FeS and PbS aqueous systems. No results are presented for ZnS [4].

The software MULTISCALE® developed by Petrotech is one of the few options that includes the prediction of FeS. The software is based on the Pitzer model and its working range is between 0 to 300 °C and pressures between 1 to 1000 bar [5].

The prediction of $FeCO_3$ deposition was determined by Amiri et al. [6] and Anderko [7] using the ScaleCHEM Software that implements the speciation-based model developed by Anderko *et al.* [8] and it is commercialized by OLI Systems Inc. Generally, there is a need for developing and validating thermodynamic model for calculating solid-liquid equilibria of sulfide systems such as aqueous ZnS, PbS and FeS. The Extended UNIQUAC model has been successfully applied to various systems for vapor-liquid-solid equilibria calculations and therefore is an obvious choice for describing these systems.

The Extended UNIQUAC is an activity coefficient model and it is combined with the Soave-Redlich-Kwong (SRK) equation of state. [9]. The model accounts for temperature and pressure dependency. The model only requires a set of parameters that are determined using experimental data. The adjustable parameters are the volume and surface are parameters for each component. These parameters account for the deviations from ideality as a consequence of differences in size and shape of the species [10]. Additional to the adjustable parameters, the Extended UNIQUAC model requires as input the Gibbs energy (ΔG_f) of formation, the enthalpy of formation (ΔH_f) and the specific heat capacity (C_p) of the ions in solution and of the solid phases. The Scale-CERE software is based on the Extended UNIQUAC model and it has been already implemented for the prediction of scaling materials such as $CaSO_4$, $CaSO_4 \cdot 2H_2O$, $BaSO_4$, SrSO4 and carbonate-scaling minerals [11,12].

7.2 The Extended UNIQUAC model

This section briefly summarizes the fundamentals of the Extended UNIQUAC thermodynamic model. The Extended UNIQUAC model is an activity coefficient model aimed to calculate liquid-solid equilibrium and vapor-liquid equilibrium. The Extended UNIQUAC model was developed from the classical UNIQUAC model by adding a Debye-Hückel term to correct for the electrostatic interactions between the ions in the liquid. The extended UNIQUAC model is a Gibbs excess energy model which applies the thermodynamic γ-φ convention. Thus, the Extended UNIQUAC model is used for determining the liquid phase activity coefficients while the Soave–Redlich–Kwong (SRK) cubic equation of state gives the gas phase non-idealities. [1]. The model consists of three terms (as shown in Eq. (6.1)) to calculate the excess Gibbs energy:

$$G^{ex} = G^{ex}_{Combinatorial} + G^{ex}_{Residual} + G^{ex}_{Extended\ Debye-Hückel} \quad (6.1)$$

where $G^{ex}$is the Gibbs excess energy; $G^{ex}_{Combinatorial}$, $G^{ex}_{Residual}$,and $G^{ex}_{Extended\ Debye\quad ückel}$ are the Gibbs combinatorial, residual and Debye-Hückel contributions to the Gibbs excess energy. The combinatorial and residual terms are calculated using the original UNIQUAC model proposed by Abrams and Prausnitz. The combinatorial term accounts for size and shape effects of a component. Those effects are quantified by introducing the structural *r* and *q* parameters. The *r* parameter refers to volume while the *q* parameter refers to surface area of a component [13,14].

The combinatorial term is defined as follows:

$$\frac{G^{ex}_{Combinatorial}}{RT} = \sum_i x_i ln \frac{\Phi_i}{x_i} - \frac{z}{2}\sum_i q_i x_i ln \frac{\Phi_i}{\theta_i} \quad (6.2)$$

where $\Phi_i$is the volume fraction, x_i is the mole fraction, *z* is the co-ordination number and $\theta_i$is the surface area fraction of component *i*.

The volume and surface area terms in Eq. (6.2) are dependent on the adjustable parameters *r* and *q* as shown in Eq. (6.3) and Eq. (6.4).

$$\Phi_i = \frac{x_i r_i}{\sum_l^N x_l r_l} \quad (6.3)$$

$$\theta_i = \frac{x_i q_i}{\sum_l^N x_l q_l} \quad (6.4)$$

where r_i is the UNIQUAC volume parameter and q_i is the UNIQUAC surface parameter of component *i* with a total of *N* liquid components. In the original UNIQUAC model, these parameters, r_i and q_i, are calculated from pure component data while these are adjustable parameters for the Extended UNIQUAC model., i.e. in the Extended UNIQUAC model, these parameters are obtained by fitting to experimental data.

The residual term, $G^{ex}_{Residual}$, accounts for short-range interactions referring to intermolecular interactions. The residual term is also calculated as in the classical UNIQUAC model and it is defined by:

$$\frac{G^{ex}_{Residual}}{RT} = -\sum_i x_i q_i \, ln \sum_i \theta_{k\,i} \psi_{k,i} \tag{6.5}$$

The parameter $\psi_{k,i}$ in Eq. (6.5) depends on the interaction energy parameters u_{ki} and u_{ii} as follows:

$$\psi_{k,i} = exp\left(-\frac{u_{ki} - u_{ii}}{T}\right) \tag{6.6}$$

The interaction energy parameters in Eq. (6.6) are functions of temperature, thus the residual term is temperature dependent while the combinatorial term is not. The energy interaction parameters are obtained by fitting to experimental data and are defined as:

$$u_{ki} = u^0_{ki} + u^T_{ki}(T - 298.15). \tag{6.7}$$

$$u_{ii} = u^0_{ii} + u^T_{ii}(T - 298.15) \tag{6.8}$$

The u_{ki} interaction parameter refers to interaction between different species while u_{ii} refers to interactions between same species.

The third term in Eq. (6.1) is the Debye-Hückel term which accounts for deviations from ideality as a result of ions present in the aqueous solution. This term accounts for electrostatic interactions between ions. The Extended UNIQUAC model uses a simplified expression, the Debye-Hückel Extended law, for determining the Debye-Hückel contributions to the Gibbs excess energy. This Debye-Hückel term is defined by:

$$\frac{G^{ex}_{Debye-Hückel}}{RT} = -x_w M_w \frac{4A}{b^3}\left[ln(1 + bI^{0.5}) - bI^{0.5} + \frac{b^2 I}{2}\right] \tag{6.9}$$

where x_w is the mole fraction of water, M_w the molar mass of water, A the Debye-Hückel parameter in $(kg \cdot mol^{-1})^{1/2}$, b is a constant $(1.5\ kg \cdot mol^{-1})^{1/2}$, and I the ionic strength of the solution. In the Extended UNIQUAC model A is assumed temperature dependent by [15]:

$$A = \left(1.131 + 1.335 \cdot 10^{-3}(T - 273.15) + 1.164 \cdot 10^{-5}(T - 273.15)\right) \tag{6.10}$$

This expression is valid in the temperature range: 273.15 K< T< 383.15 K.

Solid-liquid equilibrium (SLE)calculation

The general equilibrium criterion between phases is an equal chemical potential of the species in all the phases:

$$\mu_i^{\alpha}(T,P,n) = \mu_i^{\beta}(T,P,n) = \cdots = \mu_i^{\pi}(T,P,n) \tag{6.11}$$

This thermodynamic condition for equilibria states that the chemical potentials of a substance at a determined pressure, temperature and equilibrium composition must be equal in all the phases present.

The chemical potential for a component *i* is expressed as follows:

$$\mu_i = \mu_i^0 + RT\ ln\ (x_i\gamma_i) \tag{6.12}$$

where μ_i is the chemical potential of component *i*, μ_i^0 is the standard state chemical potential of component *i* and x_i is the mole fraction of component *i*.

In order to obtain the SLE composition the activity coefficients need to be determined. This can be achieved by partial molar differentiation of the excess Gibbs energy, Eq. (6.13):

$$ln\ \gamma_i = \left[\frac{\partial\left(\frac{nG^{ex}}{RT}\right)}{\partial n_i}\right]_{P,T,n} \tag{6.13}$$

where γ_i is the activity coefficient of component *i*, G^E is the excess Gibbs energy, *R* is the gas constant (8.314 J K^{-1} mol^{-1}), *T* is the temperature in Kelvin (K) and *n* is the number of moles.

Then the definition presented in Eq. (6.13) is applied to Eq. (6.1) obtaining the activity coefficients for the three terms.

$$ln\ \gamma = ln\ \gamma^{Combinatorial} + ln\ \gamma^{Residual} + ln\ \gamma^{Debye-Hückel} \tag{6.14}$$

Using the definition of chemical potential from Eq. (6.12) and introducing the solubility product definition:

$$K_{e,j} = exp\left(-\frac{\Delta_r G_j^0}{RT}\right) = \prod\nolimits_i (x_i\gamma_i)^{v_i,j} \tag{6.15}$$

where $K_{e,j}$ is the solubility product, $\Delta_r G_j^0$ is the change in standard-state Gibbs energy and ν_i is the stoichiometric coefficient of species *i* in equilibrium *j*.

Equation (6.15) is solved simultaneously for all the species at different equilibria along with the vapor-liquid equilibrium equations. In this manner the Extended UNIQUAC model calculates the solid-liquid equilibrium of a given system. For a more detailed description of the model we refer to previous works [1,10,14].

7.3 Results

The performance of the Extended UNIQUAC model against the obtained experimental data for ZnS, FeS, PbS and $FeCO_3$ are presented in this section. Since the main focus of this thesis is solubility determination of sulfites, here the modeling results are presented as solubility (in molality) versus temperature.

Table 7.1 Interaction parameters considered in this work

	H_2O		**HS^-**		**Cl^-**		**Na^+**	
			u_{ij}^0 (K)					
Zn^{2+}	792.116	a	-1735	b	1646.75	a	-114.83	a
Fe^{2+}	765.58	a	N.D.		1623.74	a	-86.69	a
Pb^{2+}	-260.82	d	N.D.		1180.535	d	422.31	d
Na^+	733.28	c	66.67	c	1443.23	c	0	c
Cl^-	1523.39	c	412.04	b	2214.81	c	-	
			u_{ij}^T					
Zn^{2+}	2.172	a	45	b	17.102	a	0.217	a
Fe^{2+}	2.350	a	N.D.		14.095	a	0.751	a
Pb^{2+}	-2.16	d	N.D.		14.801	d	1.21	d
Na^+	0.48	c	9.85	c	15.63	c	0	c
Cl^-	14.63	c	10.336	b	14.436	c	-	

[a] Parameters obtained from Iliuta et al. [16]. Valid at temperatures between 0 °C to 110 °C.
[b] Parameters determined in this work. The parameters are indicative as they have not been evaluated with other aqueous systems containing the same ions.
[c] Parameters determined by Thomsen and Rasmussen [2].
[d] Parameters obtained from Rodriguez [27]
N.D. Not determined

As mentioned, the scope of this study is on investigating the potential of the Extended UNIQUAC model for predicting the SLE and therefore, only a few parameters that were not determined previously were adjusted. The *r* and *q* parameters were previously adjusted by Iliuta et al (2002) are

used here as input for the Extended UNIQUAC model. The interaction parameters u^0 and u^T are consider temperature dependent and are determined by fitting to the solubility experimental data for the ion-pairs: Cl^--HS^- and Zn^{2+}-HS^-. For the other pairs they were taken from previous publications [2,16]. A summary of the most relevant interaction parameters is shown at the end of this section in Table 7.1.

The validation of the parameters for the interaction between HS^- and Na^+ has been carried out using sodium sulfide (Na_2S) solubility data [17–26].

In aqueous solution, sulfide exists in the form of H_2S(aq), HS^-, and S^{2-}. H_2S dominates at acidic pH while HS^- is mainly present in alkaline solutions. The sum of the amounts of these three-sulfur species constitutes the total sulfur content. The "classical" approach for describing the speciation of H_2S in aqueous solution is also challenged in this work. The "classical" speciation proposed for H_2S is shown in Eq. (6.16). However, due to uncertainty of the value of pKa_2 for H_2S, we have followed new scientific findings of May et al. [28] and did not include S^{2-} in low temperature aqueous chemistry. Instead of Eq. (6.16), the solubility of metal sulfides is described in terms of HS^- by Eq. (6.17) [29]:

$$H_2S_{(aq)} \leftrightarrow H^+ + HS^- \tag{6.16}$$

$$MS_{(s)} + H^+ \leftrightarrow M^{2+} + HS^- \tag{6.17}$$

where *M* symbolizes the metal ion.

7.3.1 Solubility of Na_2S in water

The solid-liquid equilibria (SLE) of Na_2S in aqueous solution is calculated using the Extended UNIQUAC model. The speciation scheme assumed for the calculations is presented in Eq. (6.18) and Eq. (6.19). Equation (6.18) refers to the classical model speciation including S^{2-} as one of the species present in the aqueous solution. Meanwhile Eq. (6.19) presents the speciation based on the new findings of May et al. [28] that excludes the presence of S^{2-} in the aqueous solution. The energy interaction parameters between Na and water were obtained from Thomsen and Rasmussen [2]. These are presented in Table 7.1.

$$Na_2S \leftrightarrow 2Na^{2+} + S^{2-} \tag{6.18}$$

$$Na_2S(s) + H_2O \leftrightarrow Na^{2+} + HS^- + OH^- \tag{6.19}$$

The behavior of the model against a large number of experimental data (covering the temperature range of -20 °C to 110 °C respectively Na_2S content from 0 to 60%) is presented in Figure 7.1. This figure shows the predicted equilibrium temperature as function of aqueous Na_2S solution concentration.

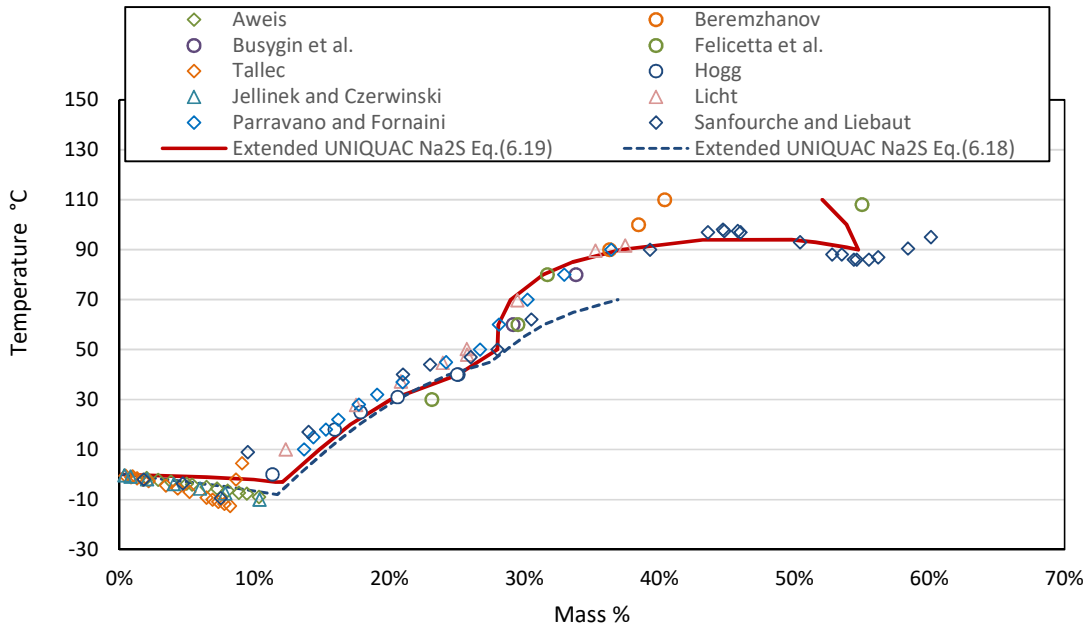

Figure 7.1 Solid-liquid equilibria for Na_2S.

Data from Aweis [17]; Beremzhanov [18]; Busygin et al. [19]; Felicetta et al.[20]; Tallec [21]; Hogg [22]; Jellinek and Czerwinski [23]; Licht [24]; Parravano and Fomaini [25] and Sanfourche and Liebaut [26]

Figure 7.1. presents the results of the SLE calculations for the Na_2S aqueous system. The dark-blue dashed line in Figure 7.1 are the results obtained using the speciation model presented in Eq. (6.18). It is observed that the Extended UNIQUAC can represent the SLE at temperatures up to 50 °C. Beyond this temperature, between 50 °C and 70 °C, the deviation of the model from the experimental data is significant. Above 70 °C the model does not converge.

The continuous red line in Figure 7.1. represents the results obtained using Eq. (6.19). These results demonstrate that the Extended UNIQUAC model represent accurately the SLE of the Na_2S aqueous solution. The deviation between model and experimental data is within two mass percent (2%). These results support the new speciation model [Eq. (6.19)] used for the calculations of the activity coefficients. Consequently, the exclusion of S^{2-} ions from the speciation scheme improved the

modeling of the experimental data. Thus, the following modeling results of the zinc-, iron and lead-sulfides are based on the speciation presented in Eq. (6.19).

7.3.2 Zinc Sulfide

The solid liquid equilibria calculations (e.g. solubility) for ZnS in aqueous solution are presented in this section using the Extended UNIQUAC thermodynamic model. The extended UNIQUAC model has not been used previously for describing this system (aqueous ZnS) due to the lack of experimental data for determining the adjustable parameters. Therefore, determination of some adjustable parameters was expected before performing SLE calculations.

The adjustment of the model parameters relies on the experimental data obtained in this study, presented in Chapter 3 and Chapter 4. To investigate the model accuracy, the performance of the model has been compared to previously published data as well.

In order to show the need for determination of the model parameters, initially the model predictive capacity has been compared to experimental data using the thermodynamic properties published by NIST [30] (ΔG_f and ΔH_f) for ZnS. These initial results do not include any parameter fitting. The purpose was to observe the impact of the parameters on the SLE calculations. These results are presented in Figure 7.2. The SLE for ZnS is represented by the solid red line while the SLE for ZnS in 0.7 m NaCl is represented by the dashed line. The calculated SLE is far from the experimental data at all temperatures. Especially the solution that contains NaCl shows an excessively high solubility compared to the available experimental data.

Figure 7.2 shows that the SLE cannot be calculated using the NIST values for the thermodynamic properties of the species involved. Rather a set of parameters need to be estimated based on the experimental data. Therefore, a sensitivity analysis has been performed to investigate which parameters strongly influence the SLE calculations. This study showed that the Gibbs energy of formation must be modified, to bring the model near the experimental values. Consequently, the Gibbs energy of formation was slightly modified to improve the accuracy of the speciation equilibria calculations, while the enthalpy and the heat capacity used for the calculations is taken from NIST [30]. Furthermore, the interaction parameters $u_{ij}^{(0)}$ and $u_{ij}^{(t)}$ for the species Zn^{2+} and HS^- were fitted.

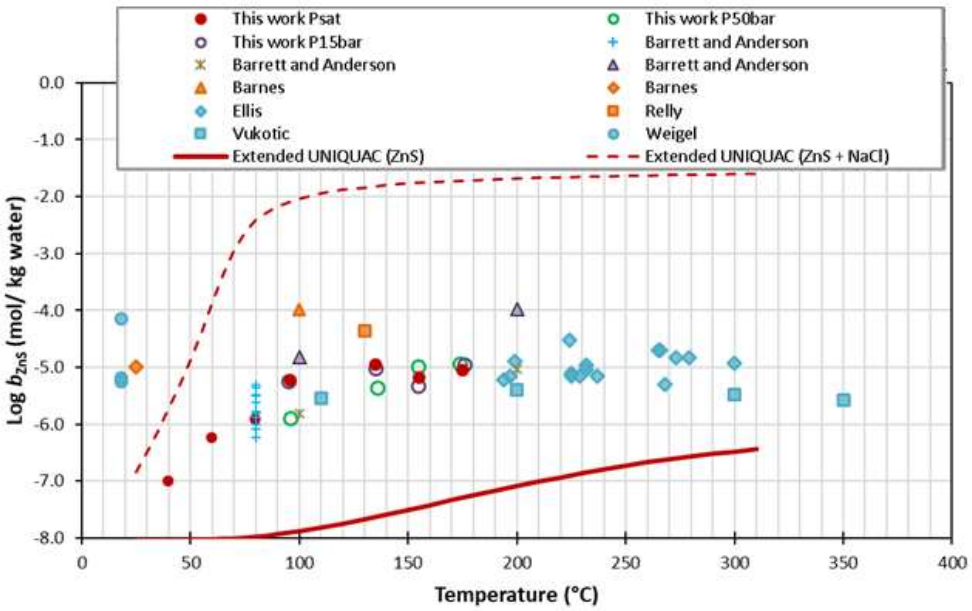

Figure 7.2 Results obtained by using ΔG_{ZnS}=-201.29 kJ·mol^{-1} and ΔH_{ZnS}=-205.98 kJ·mol^{-1}K^{-1} (Values reported by NIST). Barrett [31] data obtained at saturated H_2S, cross and star marker at NaCl 1m and tringle marker at NaCl 3m pH between 5.5 and 7.5. Relly [32] at 275-345 bar (pressure range is presented since it is not certain the value at which the experiments were run); Barnes [33] at 6.8 bar (diamond marker) and at 34 bar (triangle marker); Ellis [34]; Vukotic [35] and Weigel [36]

The $u_{ij}^{(0)}$ parameter shows a strong interaction between Zn and HS- as the parameter is negative and the previously fitted parameters for HS^- with other anions are positive. The results in Figure 7.3 obtained with the improved parameters, i.e. Gibbs energy of formation and the interaction parameters, outline that the model can describe the temperature dependency of the solubility of aqueous ZnS.

For the system containing 0.7 m NaCl it was found that the parameters that have a high impact on the calculation are the interaction parameters between Cl^- and HS^-. The results for this system are also shown in Figure 7.3. The SLE was challenging to represent with the Extended UNIQUAC model at temperatures higher than 95 °C. It is observed in Figure 7.3 that at temperatures above 100 °C the model presents extremely high values for solubility. A sensitivity analysis performed to adjust other parameters relevant to this aqueous system showed that other parameters have no impact whatsoever on the SLE calculations. It appears that a good fit above 100 °C cannot be obtained with the current parameters and/or the speciation equilibria model proposed.

Garcia [10] mentioned that the SLE for NaCl at temperatures above 150 °C was not described accurately by the Extended UNIQUAC model. Thus, it is possible that new parameters are needed at higher temperatures.

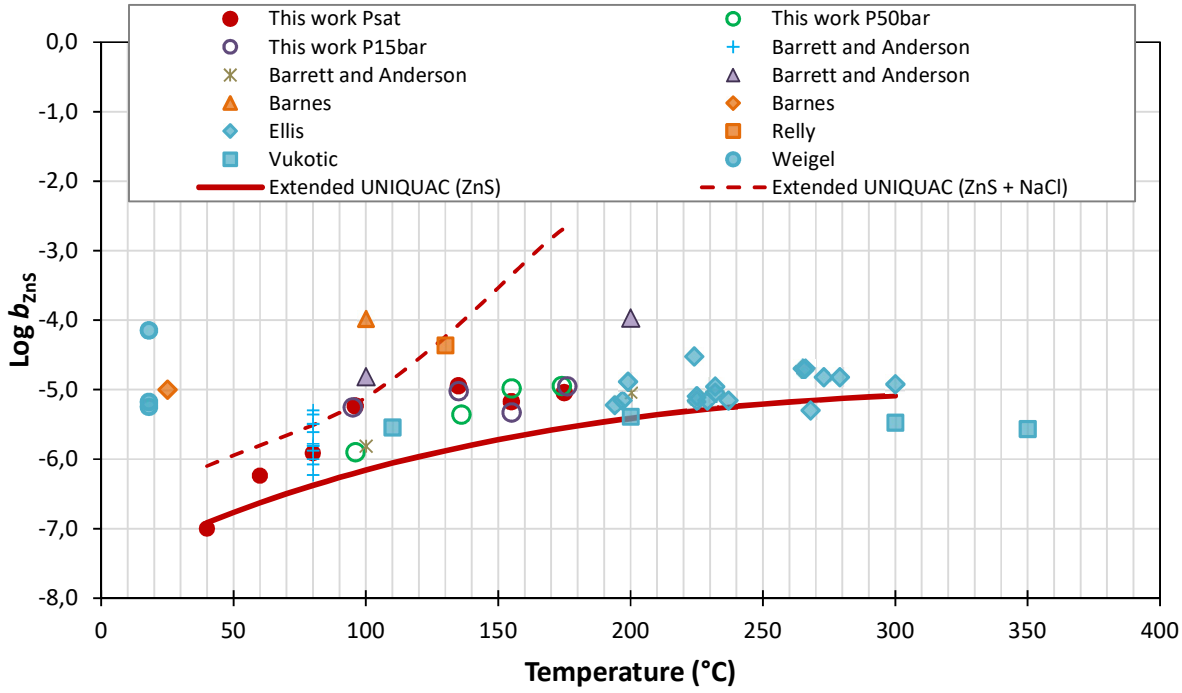

Figure 7.3 Results obtained by adjusting ΔG_{ZnS} and by fitting the interaction parameters for HS^- - Cl^-. Barrett and Anderson [31] data obtained at saturated H_2S, cross and star marker at NaCl 1m and tringle marker at NaCl 3m pH between 5.5 and 7.5. Barnes [33] at 6.8 bar (diamond marker) and at 34 bar (triangle marker); Ellis [34]; Relly [32] at 275-345 bar (pressure range is presented since it is not certain the value at which the experiments were run); Vukotic [35] and Weigel [36]

On the other hand, the results obtained suggest that the Zn speciation equilibria model proposed here is not adequate (see Eq. 6.). Currently, in the Extended UNIQUAC model it is assumed that Zn solely exits in aqueous form as $Zn^{2+}_{(aq)}$ with no other complexes formed. The presence of a metallic ion (i.e. Zn), OH^-, Cl^- and S^{2-} as potential ligands in addition to the decrease of dielectric constant of water at elevated temperatures; makes the ZnS aqueous system suitable for the formation of complexes [37,38]. Note that several studies have considered the inclusion of complexes for the Zn speciation model for solubility studies of ZnS [39–42] .

It has been shown that zinc is also present in complexed form (chloride and hydrosulfide) in hydrothermal fluids [39]. Furthermore, Hayashi *et al.* measured the solubility of ZnS at temperatures

between 25 °C and 240 °C. They concluded that the inclusion of complexes for the Zn speciation in aqueous solution is vital for accurate modelling [40]. Accordingly, they proposed a model in which zinc sulfide complexes were the dominant species to represent the experimental data obtained. According to this study, the predominant zinc sulfide complexes present at temperatures between 100 °C and 200 °C were $Zn(HS)_2^0$ and $Zn(OH)(HS)_2^-$ at pH values between 3 and 10. Tagirov et al. concluded that in the presence of $Cl^-_{(aq)}$ (i.e. in presence of NaCl), Zn is mainly present in the form of $ZnCl^+$, $ZnCl_2$ and $ZnCl_4^{2-}$ complexes [39,41]. It is claimed by Tagirov *et al.* that the Zn speciation model proposed is likely to accurately represent the Zn species that exits in an aqueous solution. Their experimental results and model calculations differ 0.1 log units and it is pointed out that the deviation is within the uncertainty of pH [39]. In a more recent study of ZnS solubility by Tagirov and Seward [42] the Zn speciation model suggests that Zn^{2+} is dominant at very acidic pH values and its concentration decreases as temperature increases. Meanwhile, the concentration of species like $Zn(HS)_2^0$ and $Zn(HS)_3^-$ increases with respect to temperature. Other intermediate complexes are also included in the speciation model but as temperature increases the other complexes disappear. $Zn^{2+}_{(aq)}$, $Zn(HS)_2^0$ and $Zn(HS)_3^-$ are the only species present at 350 °C. $Zn(HS)_2^0$ is the only complex present in the pH range between 3 and 8 at 350 °C [42]. Note that other complexes included in this model, such as $Zn(HS)_2OH^-$ also play a significant role up to 100 °C and above pH values of 5 [41].

The Extended UNIQUAC model currently does not include formation of any complexes in the speciation model for ZnS. This is potentially the main reason for over-prediction of the solubilities, especially for the ZnS+NaCl aqueous system. Information regarding the equilibrium and stability constants for a list of Zn complexes is presented in the IUPAC Technical Report presented by Powell et al. [43]. This information constitutes the basis for including the Zn complex compounds into the Extended UNIQUAC model. Then a series of Zn speciation models need to be proposed and validated against experimental data.

7.3.3 Iron sulfide

In this section the solid-liquid equilibrium calculation using the Extended UNIQUAC model for the aqueous FeS system is presented. The parameters for this system for the Extended UNIQUAC model have not been determined previously. Note that the approach employed in these calculations is the same described in Section 7.3.2. Thus, first the Gibbs energy of formation for FeS, ΔG_{FeS} was adjusted. The value reported by NIST for ΔG_{FeS} is -100.4 kJ/mol [30] while the value determined in this case was ΔG_{FeS}= -66.95 kJ/mol. This is a significant change in the Gibbs energy. However, this

can be explained by the difference in the characteristics of each material for which the energy of formation was reported. The interaction between Fe^{2+} and HS^- is found to be low as the parameters between those ions do not have any visible impact on the SLE calculations. For this reason, these parameters were excluded by setting them to large numbers.

The results for the SLE calculations using the Extended UNIQUAC model for the FeS aqueous system are presented in Figure 7.4. This figure shows that the Extended UNIQUAC model can describe the SLE accurately at temperatures up to 60 °C. At 80 °C a large deviation from the experimental data is obtained. The deviation may be due to an erroneous determination of the equilibration time at 80 °C.

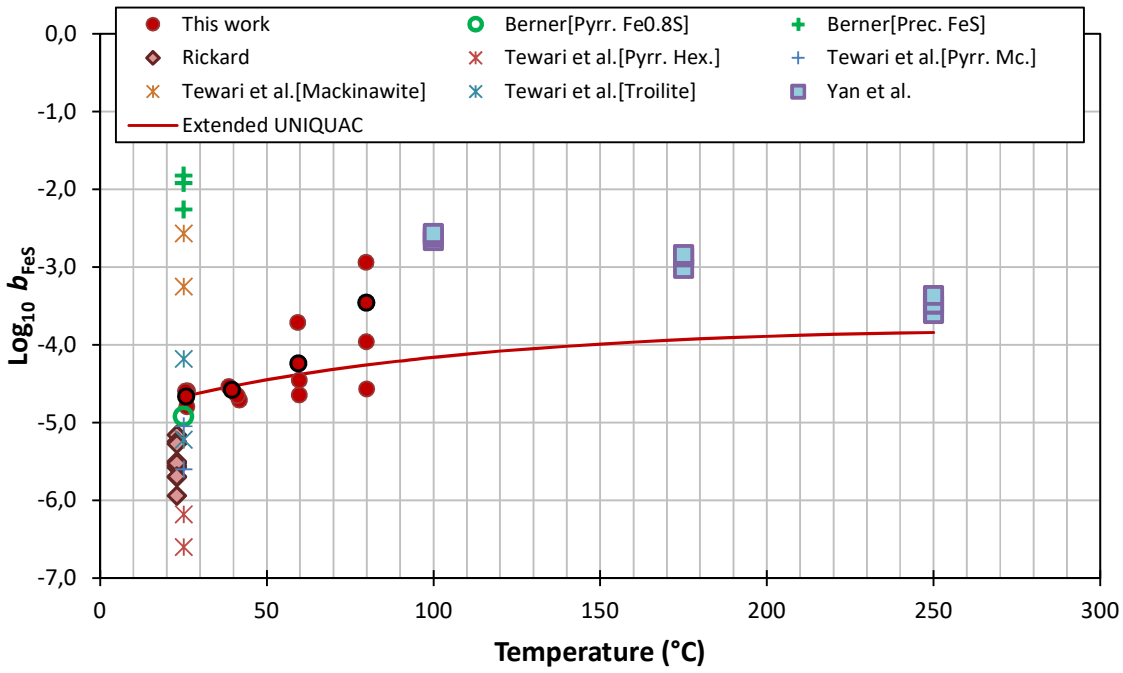

Figure 7.4 SLE calculations for FeS aquous system.

Data taken from Berner [46] for pyrrhotite and precipitated FeS; Rickard [29] at pH between 6.5 and 8.0; Tewari *et al.* [47] for pyrrohotite hexagonal, mackinawite, pyrrhotite monoclinic and troilite and Yan et al. [44] in 1M NaCl solution.

Another hypothesis is that the Fe speciation model proposed is not adequate. As in the case of ZnS, complexes may form as temperature raises. The only data available at high temperatures are reported by Yan et al. [44]. These results obtained by Yan et al. [44] show higher values for FeS solubility at temperatures between 100 °C and 250 °C than the solubility predicted by the model. As pointed by

Davison [45] there is no agreement on the speciation of FeS (and this could be extended to other sulfides).

The presence of soluble complexes could also explain the higher levels of solubility. A soluble complex Fe_2S_2 has been identified by polarographic measurements in lake water [48]. The later suggests that Fe-S complexes are present even at ambient temperatures. Therefore, thermodynamic modeling faces some challenging issues when describing SLE of FeS system.

7.3.4 Lead Sulfide

This section discusses the SLE calculation for the aqueous PbS system using the Extended UNIQUAC model. Consider that the thermodynamic model has not been neither verified nor fitted for this system.

The approach described previously has been followed to determine the best parameters for this system. A sensitivity study revealed that while the adjustment of the Gibbs energy of formation enabled the SLE calculations for the ZnS and FeS aqueous systems; but unfortunately, that is not the case for the PbS aqueous system. The best value found for the ΔG_{PbS} was -22 kJ/mol while the value reported by NIST [30] is ΔG_{PbS} = -100.4 kJ/mol. This is an enormous difference, suggesting that this Gibbs energy of formation is not a representative one. Furthermore, the analysis showed that none of the parameters have visible effect on the calculations. These findings suggest that the modeling assumptions do not hold for this system.

Once again, the hypothesis of the presence of complexes in the aqueous solution arises. The high values obtained for PbS solubility presented in Chapter 4 cannot be modelled using the Extended UNIQUAC with the speciation model assuming that the only species present are: PbS, Pb^{2+} and HS^-. High values of solubility for PbS in hydrothermal systems are attributed to the formation of the $PbS{\cdot}H_2S$ complexes at pH values around 7. It is referred that the concentration of $PbS{\cdot}H_2S$ is larger than the concentration of Pb^{2+} [49]. Other complex present in solution in the pH range between 6 and 10 is $PbOH^+$ [50]. Thus, further improvement of the thermodynamic model is necessary to include complexes in the speciation scheme.

7.3.5 Iron carbonate

In this section the Extended UNIQUAC model is applied for SLE calculation of aqueous $FeCO_3$. In this case, the Gibbs energy and enthalpy of formation for $FeCO_3$ were adjusted to accurately approximate the solid-liquid equilibrium experimental data. The two standard properties obtained

after fitting the model to the experimental data are presented in Table 7.2. This table also shows the recommended values for $FeCO_3$.

Table 7.2 Standard properties for $FeCO_3$

$FeCO_3$	ΔG^0f (kJ mol^{-1})	ΔH^0f (kJ mol^{-1})
Adjusted values	-691.68	-724.78
Data from [51,52]	-676.88	-750.01
Data from [30,51]	-665.16	-738.28

There are variations observed in the standard properties of $FeCO_3$ published in literature as noted in Table 7.2. The adjusted properties differ slightly from those previously published but it can be said that the variation is acceptable (± 3%). The interaction parameters u^0 and u^T where found to have an insignificant effect on the excess Gibbs function. This result was expected since the concentration of the species is very low and therefore the interaction between the species is almost negligible.

The experimental data and the SLE calculated with the Extended UNIQUAC model are presented in Figure 7.5. The results are presented as iron concentration at equilibrium conditions versus temperature.

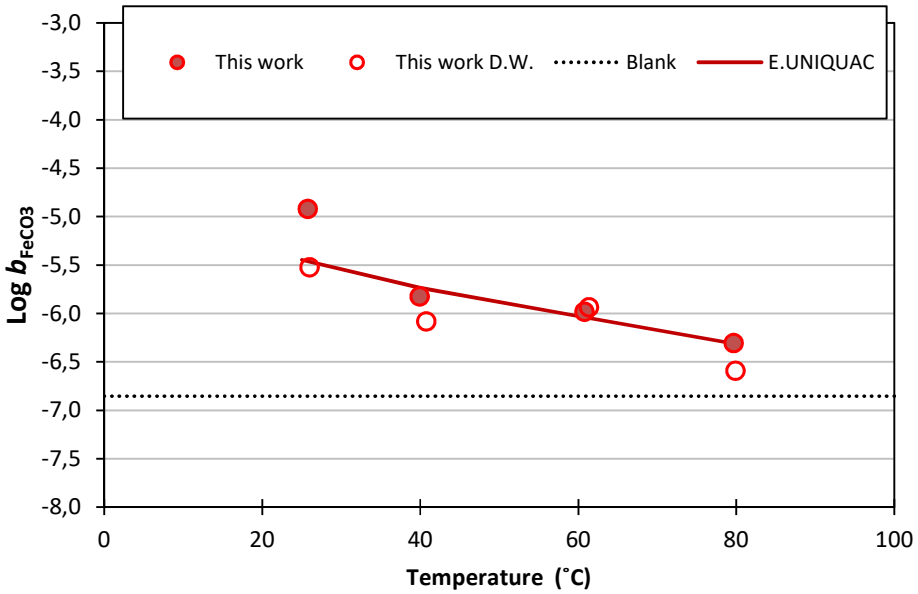

Figure 7.5 Results of the E. UNIQUAC correlation to experimental data for the binary system $FeCO_3$-H_2O. The legend D.W. refers to experimental data obtained using distilled water (refer to Chapter 4 for a detailed explanation)

It is observed in Figure 7.5 that the Extended UNIQUAC model describes accurately the experimental data. The largest deviation from the experimental data is observed at 40˚C with a deviation of 22%.

The deviation at temperatures above 40 ˚C is between experimental error. This deviation can be improved adding more experimental data as input to the E. UNIQUAC model.

7.4 Conclusions

The field of application of the Extended UNIQUAC has been expanded with this work towards prediction of sulfides solubility. The Extended UNIQUAC model has proven to be a flexible thermodynamic model capable of calculating the SLE for metallic sulfides. The results obtained here for ZnS and FeS are satisfactory. Nonetheless inconsistencies of the calculated SLE were found at temperatures above 80 °C and in the presence of NaCl. The Gibbs energy of formation for ZnS was adjusted to the experimental data and binary interaction parameters for Zn^{2+}-HS^- and HS^--Cl^- were determined. The parameters here determined are considered indicative and further comparison to other experimental data is required to evaluate the predictive capacity of the model.

After several attempts to describe the dependency on temperature of PbS; it was concluded that the speciation equilibria proposed may be incorrect. Additional, to the species considered, the hypothesis that complexes are formed in the solution at equilibrium with the metal sulfide arises. Complexes of metal ions with ligands such as S, OH^- and Cl are likely to form, especially at elevated temperatures.

This project has shown the need to include more chemical species into the Scale-CERE software (based on the Extended UNIQUAC model) to make it even more versatile allowing to propose more speciation models that include complex species of metal ions.

References

[1] A. Villafáfila Garcia, K. Thomsen, E.H. Stenby, Prediction of mineral scale formation in geothermal and oilfield operations using the extended UNIQUAC model. Part I. Sulfate scaling minerals, Geothermics. 34 (2005) 61–97.

[2] K. Thomsen, P. Rasmussen, Modeling of vapor-liquid-solid equilibrium in gas-aqueous electrolyte systems, Chem. Eng. Sci. 54 (1999) 1787–1802. http://www.sciencedirect.com/science/article/pii/S0009250999000196.

[3] M. Saidoun, K. Mateen, S. Baraka-Lokmane, C. Hurtevent, Prediction of Sulphide Scales-Improvement of Our Understanding of Heavy Metal Sulphide Solubility, in: SPE Int. Oilf. Scale Conf. Exhib., Society of Petroleum Engineers, 2016.

[4] C. Okocha, K. Sorbie, Scale Prediction for Iron, Zinc and Lead Sulphides and Its Relation to Scale Test Design, Corros. 2014. (2014) Paper No 3766. doi:10.2118/164111-MS.

[5] ExpoPetrotech©, MULTISCALE®, (n.d.). http://multiscale.no/.

[6] M. Amiri, J. Moghadasi, M. Jamialahmadi, Prediction of Iron Carbonate Scale Formation in Iranian Oilfields at Different Mixing Ratio of Injection Water with Formation Water, Energy Sources, Part A Recover. Util. Environ. Eff. 35 (2013) 1256–1265.

[7] A. Anderko, SIMULATION OF FeCO3/FeS SCALE FORMATION USING THERMODYNAMIC AND ELECTROCHEMICAL MODELS, in: Corros. Assoc. Corros. Eng. Annu. Conf., NACE, 2000.

[8] A. Anderko, P. Wang, M. Rafal, Electrolyte solutions: from thermodynamic and transport property models to the simulation of industrial processes, Fluid Phase Equilib. 194 (2002) 123–142.

[9] K. Thomsen, P. Rasmussen, Modeling of vapor–liquid–solid equilibrium in gas–aqueous electrolyte systems, Chem. Eng. Sci. 54 (1999) 1787–1802.

[10] A. Villafafila Garcia, Measurement and Modelling of Scaling Minerals, 2005.

[11] A. Villafáfila Garcia, K. Thomsen, E.H. Stenby, Prediction of mineral scale formation in geothermal and oilfield operations using the Extended UNIQUAC model: part II. Carbonate-scaling minerals, Geothermics. 35 (2006) 239–284.

[12] A. Villafáfila Garcia, K. Thomsen, E.H. Stenby, Prediction of mineral scale formation in

geothermal and oilfield operations using the extended UNIQUAC model: part I. Sulfate scaling minerals, Geothermics. 34 (2005) 61–97.

[13] D.S. Abrams, J.M. Prausnitz, Statistical thermodynamics of liquid mixtures: a new expression for the excess Gibbs energy of partly or completely miscible systems, AIChE J. 21 (1975) 116–128.

[14] K. Thomsen, Electrolyte solutions: thermodynamics, crystallization, separation methods, DTU Chem. Eng. Tech. Univ. Denmark. (2009). http://orbit.dtu.dk/files/131770579/ElectrolyteCompendium.pdf.

[15] B. Sander, P. Rasmussen, A. Fredenslund, Calculation of vapour-liquid equilibria in nitric acid-water-nitrate salt systems using an extended UNIQUAC equation, Chem. Eng. Sci. 41 (1986) 1185–1195.

[16] M.C. Iliuta, K. Thomsen, P. Rasmussen, Modeling of heavy metal salt solubility using the extended UNIQUAC model, AIChE J. 48 (2002) 2664–2689.

[17] M.S. Aweis, Thermodynamic modeling of sour gas cleaning, (2011).

[18] Beremzhanov BA, Solubilities in the system Na2S-Na2SO4-H2O at temperatures 90-140°, Izv. Akad. Nauk Kaz. SSR, Ser. Khim. 10 (1956) 104–105.

[19] V.M. Busygin, L.A. Malysh, L.G. Gaisin, K. V Tkachev, A.G. Prokhorov, M.F. Volkova, BaS-Na2S-H2O system at 60°C, Russ. J. Appl. Chem. 72 (1999) 1075–1076.

[20] V.F. Felicetta, M. Lung, J.L. McCarthy, Spent sulphite liquor -- 9, Tappi. 42 (1959) 496–513.

[21] G. Tallec, Project Report, (2011) ERASMUS student from Université de Pau et des Pays.

[22] A.R. Hogg, CXVIII.—The ternary system sodium sulphidesodium sulphate–water, J. Chem. Soc. 129 (1926) 855–862.

[23] K. Jellinek, J. Czerwinski, Über die Dissoziation von H2S, Na2S und NaHS in wässeriger Lösung, Zeitschrift Für Phys. Chemie. 102 (1922) 438–479.

[24] S. Licht, Aqueous solubilities, solubility products and standard oxidation-reduction potentials of the metal sulfides, J. Electrochem. Soc. 135 (1988) 2971–2975.

[25] F.M. Parravano N., Sopra gli idrati del solfuro di sodio, Gazz.Chim.Ital. 37 (1907) 521–527.

[26] L.A. Sanfourche A, Sur les hydrates du sulfure de sodium, Bull. Soc. Chim. Fr. 31 (1922) 966–

972.

[27] A. Rodriguez Pupo, Thermodynamic modeling of scale formation in brines from HP/HT reservoirs, Termodynamisk modellering af scale dannelse i HP/HT reservoirer, Technical University of Denmark/École Polytechnique Fédérale de Lausanne, 2016.

[28] P. May, D. Batka, G. Hefter, E. Konigsberger, D. Rowland, Goodbye to S^{2-} in Aqueous Solution, Chem. Commun. 54 (2018) 1980–1983. doi:10.1039/C8CC00187A.

[29] D. Rickard, The solubility of FeS, Geochim. Cosmochim. Acta. 70 (2006) 5779–5789.

[30] E. Shen, V.K., Siderius, D.W., Krekelberg, W.P., and Hatch, H.W., NIST Standard Reference Simulation Website, NIST Stand. Ref. Database. (n.d.) Gaithersburg MD, 20899. doi.org/10.18434/T4M88Q.

[31] T.J. Barrett, G.M. Anderson, The solubility of sphalerite and galena in NaCl brines, Econ. Geol. 77 (1982) 1923–1933.

[32] B.H. Relly, A method for determining solubility at high temperatures and pressures, Econ. Geol. 54 (1959) 1496–1505.

[33] H.. Barnes, Ore Solutions, 57th ed., Carnegie Institute of Washington, 1958.

[34] A.J. Ellis, The solubility of zinc sulfide in water at high temperatures, Econ. Geol. 54 (1959) 1035–1039.

[35] S. Vukotic, Contribution to the study of the solubility of galena, of sphalerite, and of chalcopyrite in water in the presence of hydrogen sulfide between 50 and 200 C, Bull. Bur. Rech. Geol. Min. (1961) 11–27.

[36] O. Weigel, The solubility of the sulphides of the heavy metals in water, Z. Phys. Chem. 58 (1907) 293–300.

[37] M.A. McKibben, A.E. Williams, Metal speciation and solubility in saline hydrothermal fluids; an empirical approach based on geothermal brine data, Econ. Geol. 84 (1989) 1996–2007.

[38] T.M. Seward, Metal complex formation in aqueous solutions at elevated temperatures and pressures, Phys. Chem. Earth. 13 (1981) 113–132.

[39] B.R. Tagirov, O.M. Suleimenov, T.M. Seward, Zinc complexation in aqueous sulfide solutions: Determination of the stoichiometry and stability of complexes via ZnS(cr) solubility

measurements at 100 °C and 150 bars, Geochim. Cosmochim. Acta. 71 (2007) 4942–4953. doi:10.1016/j.gca.2007.08.012.

[40] K. Hayashi, A. Sugaki, Solubility of sphalerite in aqueous sulfide solutions at temperatures between 25 and 240 ° C, 54 (1990) 3–5.

[41] N.N. Akinfiev, B.R. Tagirov, Zn in hydrothermal systems: Thermodynamic description of hydroxide, chloride, and hydrosulfide complexes, Geochemistry Int. 52 (2014) 197–214.

[42] B.R. Tagirov, T.M. Seward, Hydrosul fi de / sul fi de complexes of zinc to 250 ° C and the thermodynamic properties of sphalerite, Chem. Geol. 269 (2010) 301–311. doi:10.1016/j.chemgeo.2009.10.005.

[43] K.J. Powell, P.L. Brown, R.H. Byrne, T. Gajda, G. Hefter, A.-K. Leuz, S. Sjöberg, H. Wanner, Chemical speciation of environmentally significant metals with inorganic ligands. Part 5: The Zn2++ OH–, Cl–, CO32–, SO42–, and PO43–systems (IUPAC Technical Report), Pure Appl. Chem. 85 (2013) 2249–2311.

[44] C. Yan, P. Guraieb, R.C. Tomson, Solubility Study of Iron Sulfide FeS Under Extremely High Temperature Pressure in Strictly Anoxic, Various Ionic Strength Solutions, in: SPE Int. Oilf. Scale Conf. Exhib., Society of Petroleum Engineers, 2016.

[45] W. Davison, The solubility of iron sulphides in synthetic and natural waters at ambient temperature, Aquat. Sci. 53 (1991) 309–329.

[46] R.A. Berner, Thermodynamic stability of sedimentary iron sulfides, Am. J. Sci. 265 (1967) 773–785.

[47] P.H. Tewari, G. Wallace, A.B. Campbell, The solubility of iron sulfides and their role in mass transport in Girdler-sulfide heavy water plants, Atomic Energy of Canada Ltd., 1978. AECL-5960.

[48] W. Davison, N. Phillips, B.J. Tabner, Soluble iron sulfide species in natural waters: reappraisal of their stoichiometry and stability constants, Aquat. Sci. 61 (1999) 23–43.

[49] G.M. Anderson, The solubility of PbS in H 2 S-water solutions, Econ. Geol. 57 (1962) 809–828.

[50] K.J. Powell, P.L. Brown, R.H. Byrne, T. Gajda, G. Hefter, A.-K. Leuz, S. Sjöberg, H. Wanner, Chemical speciation of environmentally significant metals with inorganic ligands. Part 3: The

Pb2++ OH–, Cl–, CO32–, SO42–, and PO43–systems (IUPAC Technical Report), Pure Appl. Chem. 81 (2009) 2425–2476.

[51] P.L. Fosbøl, K. Thomsen, E.H. Stenby, Review and recommended thermodynamic properties of FeCO3, Corros. Eng. Sci. Technol. 45 (2010) 115–135. doi:10.1179/174327808X286437.

[52] J.D. Cox, D.D. Wagman, V.A. Medvedev, CODATA Key Values for Thermodynamics 1989, Hemisphere, New York Google Sch. (n.d.).

Recommendations for future work

The study of scaling materials is an extensive field in which several branches of engineering play an important role. Understanding the thermodynamics and kinetics of this phenomenon is especially needed in the field of reservoir engineering to maximize profit while protecting pipelines, wells and machinery. A newly emerging and little understood area is sulfide scaling, i.e. precipitation of FeS, PbS and ZnS.

The foundations to explore the behaviour of scaling materials under certain conditions (i.e. temperature, pressure, etc.) lay on the experimental work. As highlighted throughout this document, the lack of experimental data on solubility of sulfides, well established and reliable experimental methodology as well as the need for special treatment of samples (low oxygen conditions, particle size analysis, determination of chemical composition of the mineral, etc.) made this work somehow challenging. The few experimental data published are in some cases non-comparable to other studies, as the experimental conditions differ between them. More experimental data are needed to support the thermodynamic modeling and ultimately to evaluate the risk of precipitation in oil reservoirs, large equipment (e.g. heat exchangers) and geothermal reservoirs. Additional variables to resemble reservoirs conditions such as higher pressures, higher temperatures, presence of NaCl (higher salinity) and interference of other scaling materials need to be considered. For example, the risk of sulfide scaling can be minimized by controlled precipitation of $FeCO_3$ [1]. The addition of NaCl to the aqueous solution will simulate the conditions when sea water is injected to reservoirs for production purposes. Additional to an increase of the ionic strength of the solution that will impact on the solubility of the sulfide, flocculation of fine particles will be promoted as well [2]. The reduction of fine particles in the aqueous solution impacts directly on the quality of results that are obtained. Fine particles as demonstrated in this study interfere on the analysis of results using analytical techniques such as ICP-OES. This can be extended to techniques that use similar principles for trace concentration determinations as Inductively Coupled Plasma Mass Spectrometry (ICP-MS) and Atomic absorption spectroscopy (AAS).

The High Temperature (HT) Titanium Cell has been built with the main purpose of measuring solubility of aqueous solutions. This cell can be used for a wide range of temperature and pressure range which makes it appropriate for producing data that can be used for validating thermodynamic

models in the whole area of application. However, benchmark of this cell for well-known systems would be helpful to minimize uncertainties and better understand the potential pitfalls, i.e. presence of fine particles, accuracy of the dilution process.

This HT Titanium Cell designed and built in this project is a versatile equipment that can be employed for other type of laboratory experiments as well. For example, the determination of properties of liquids at various pressures and temperatures and at different concentrations (simple phase relations) can be performed. Also, differences in composition can be determined as the cell is equipped with a conductivity probe.

The findings of this work suggested that a new speciation equilibrium model including complexes for sulfides in aqueous solutions need to be proposed and evaluated. The inclusion of complexes will result in a more realistic model and a more accurate SLE calculation, especially in the case of PbS. Previous studies have reported that the complexes species in aqueous systems of ZnS and PbS are present at high temperatures (i.e. above 80 °C).

Appendix A

This appendix contains complementary drawings of the HT Titanium Cell. Figure A-1 and Figure A-2 show the cross-section of the Equilibration Cell and Dilution Cell in which the dimensions of the cells are specified. Additionally, Figure A-1 3resents a detailed drawing of each cylinder head in which the distribution of the five service-ports is shown. The distribution of the six screws to fasten the cylinder head to the cylinder body is presented.

Figure A-4 presents a three-dimensional exploded-drawing type of the HT Titanium Cell. This plot presents the interaction between various parts and their assembly to the cylinder body.

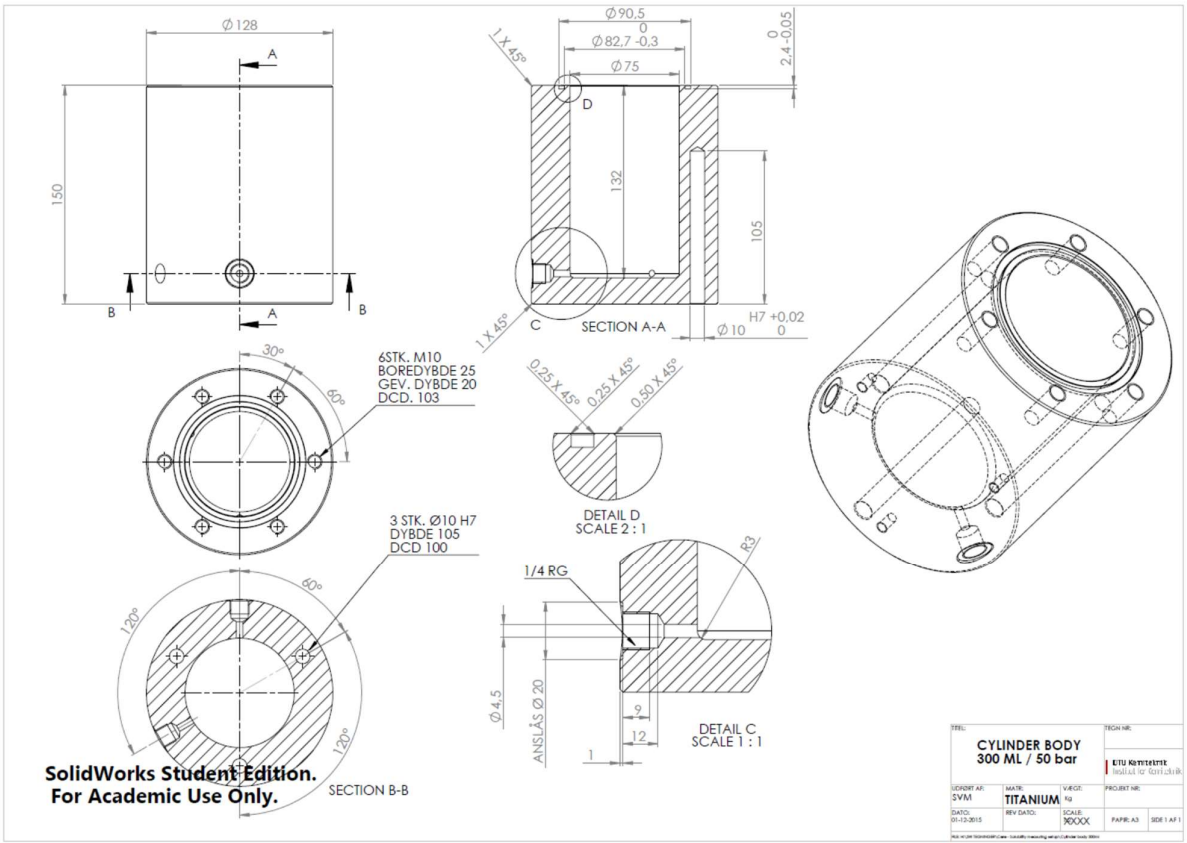

Figure 9-1 Equilibration Cell

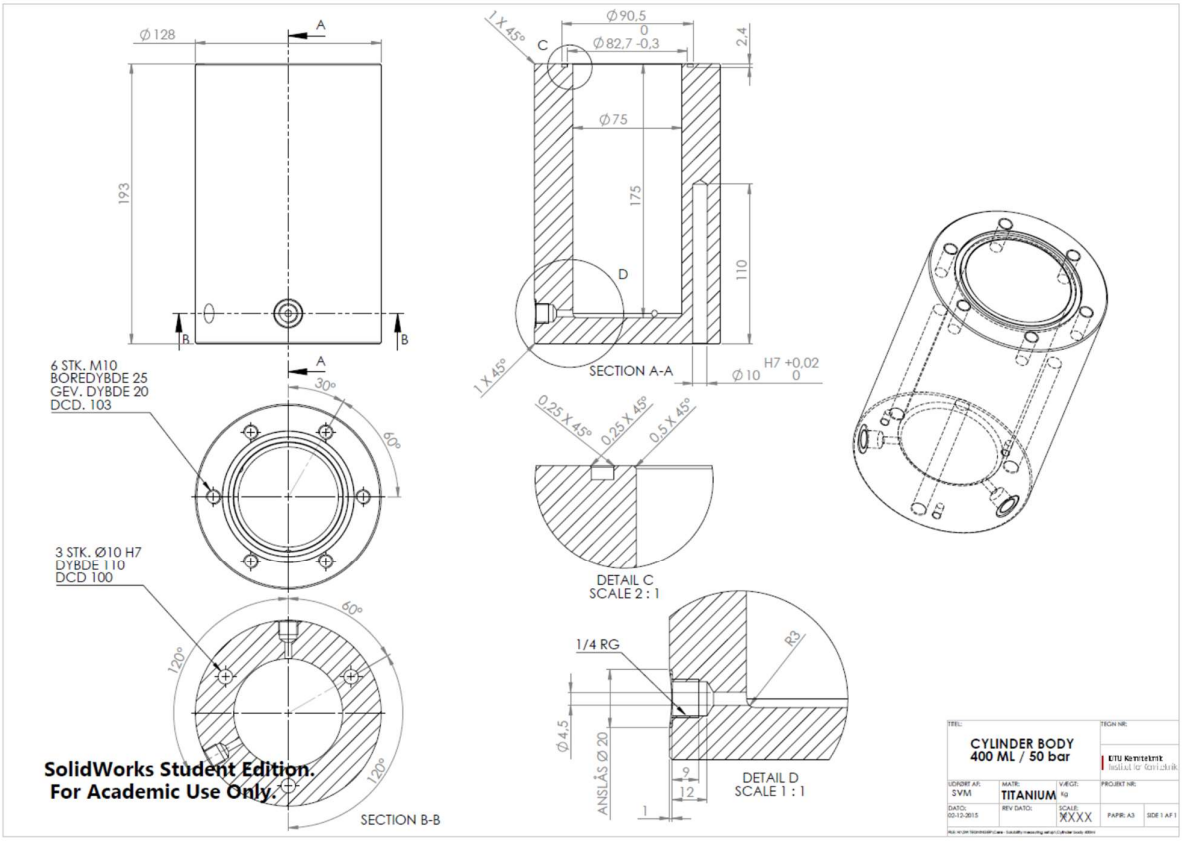

Figure A-2 Dilution Cell

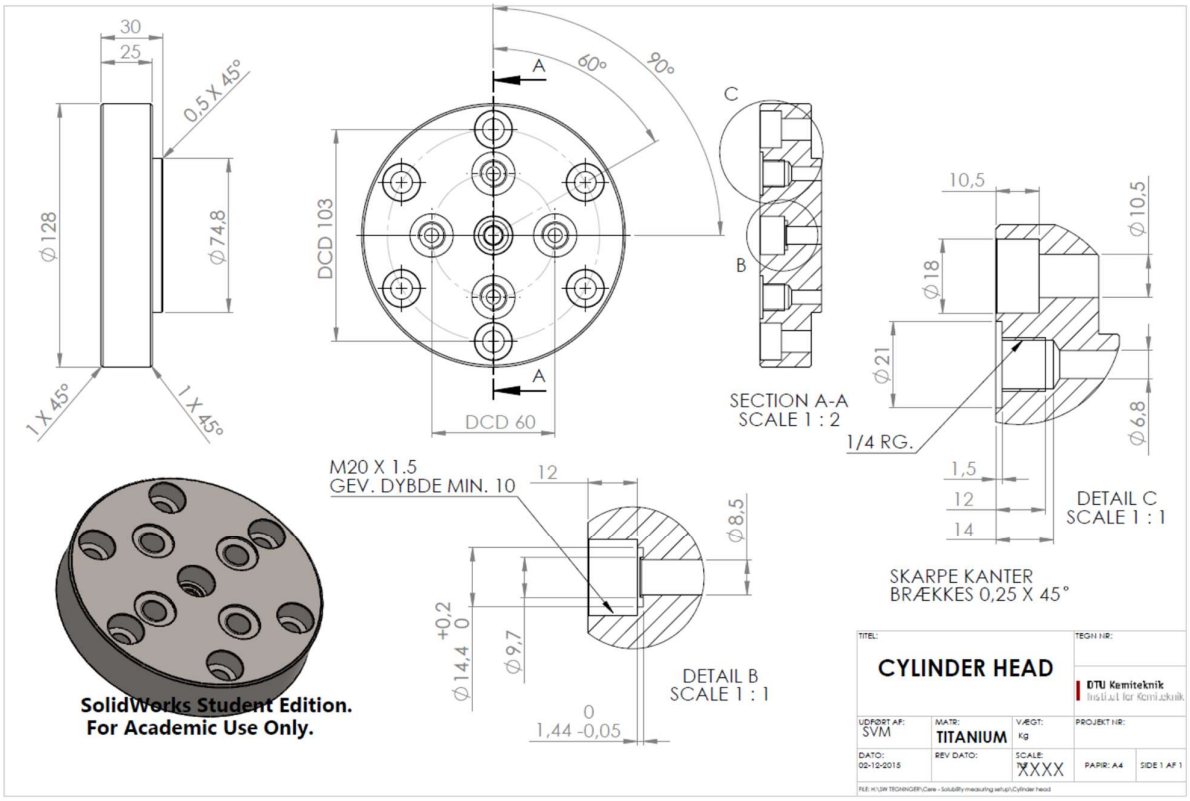

Figure A-3 Cylinder Head

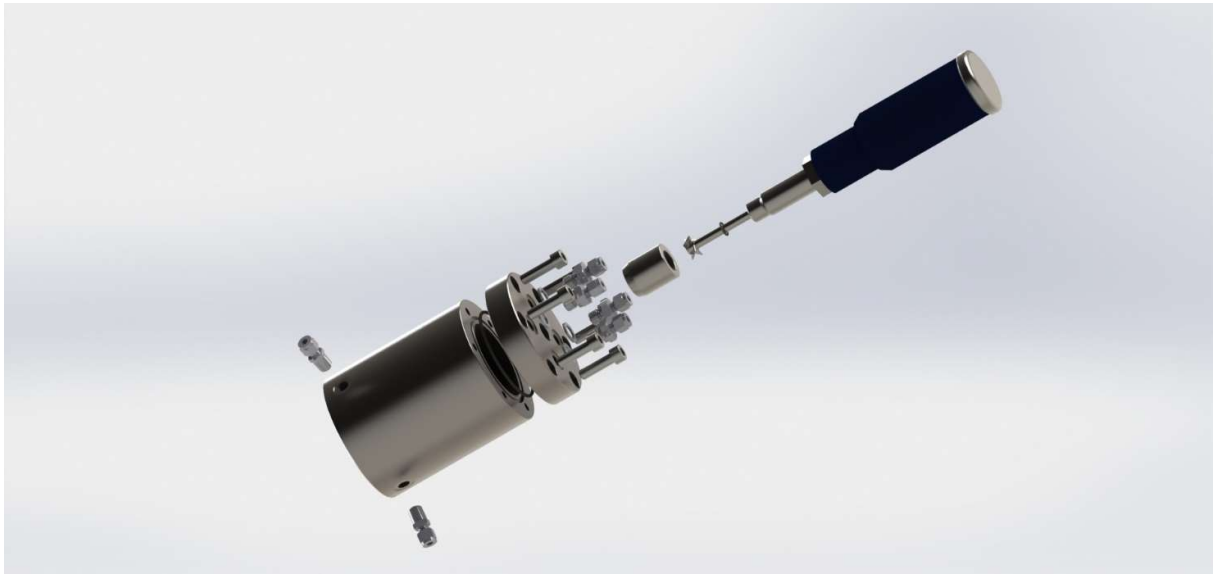

Figure A-4 3D sketch of the Equilibration and Dilution Cells